THESIS

KINETIC CONTROL OF SOLID STATE METATHESIS REACTIONS

Submitted by

Andrew J. Martinolich

Department of Chemistry

In partial fulfillment of the requirements

For the Degree of Doctor of Philosophy

Colorado State University

Fort Collins, Colorado

Fall 2017

Doctoral Committee:

Advisor: James Neilson

Amy Prieto
Amber Krummel
Matthew Shores
Jose de la Venta

ABSTRACT

KINETIC CONTROL OF SOLID STATE METATHESIS REACTIONS

The control of solid state reaction pathways will enable the design and discovery of new functional inorganic materials. A range of synthetic approaches have been used to shift solid state chemistry away from thermodynamic control, in which the most energetically favorable product forms, towards a regime of kinetic control, so that metastable materials can be controllably produced.

This work focuses on the use of solid state metathesis in the preparation of transition metal sulfides and selenides, and understanding the reaction pathways through which these reactions proceed. Through a range of structural probes combined with thermal analysis techniques, the reaction pathways are identified. The challenge of changing the pathway is then tackled, aiming to maximize mixing in the reaction mixtures to overcome the classical diffusion limitations in solids at low temperatures. Changing the reaction pathway promotes the formation of metastable intermediates and products, highlighted by the formation of the superconducting cubic polymorph of $CuSe_2$.

Future work is suggested, surrounding the idea of maximizing diffusion and mixing at low temperatures. Understanding the properties of reactants, intermediates, and products to direct the reaction pathway is paramount in controlling the pathways through which reactions occur. This will progress the field of synthetic solid state chemistry towards the

ability to design materials and reactions that are not limited by thermodynamics, in turn yielding the discovery of a range of new, functional compounds.

ACKNOWLEDGEMENTS

As my tenure as a graduate student comes to a close, I am filled with gratitude. No amount of thanks would be enough to properly acknowledge the mentorship I received from my advisor, Professor Jamie Neilson. Working with Jamie has taught me about the necessity to just go for it, whether it be trying a reaction you're convinced won't work or running up and down hills all day long. The amount of support and guidance Jamie provided to me without stifling my own development as an independent scientist was inspiring, and a trait that I hope to inherit as I continue in my career. More than anything else, Jamie's immense amount of patience for me over the years has been the direct precursor to any successes I've had. Thank you for everything.

I also thank my undergraduate research advisor, Prof. Korin Wheeler. She introduced me to the wonder of scientific research and ignited my passion for working in the lab. The realization that not all education need stem from reading out of a book has allowed me to reach far beyond what I ever imagined for myself. I must also acknowledge my high school chemistry teacher, Zach Matson, for introducing me to the field of chemistry in such a way that made it feel fun and interesting rather than a boring chore that had to be done.

To my committee members, Professors Amy Prieto, Amber Krummel, Jose de la Venta, and Matt Shores, thank you for dedicating your time and effort as educators towards my development as a scientist. It has also been my pleasure in collaborating with Amy Prieto and Matt Shores along with their groups.

I would also like to acknowledge my excellent coworkers in the Neilson group. Often times talking with you about your chemistry, results, and ideas got me more excited and

motivated than thinking about my own. Thank you for entertaining my incessant questions and tolerating my variable congeniality.

I'd specifically like to thank Dr. Joshua Kurzman. Thank you for imbuing upon me the necessity of urgency in ones work, and your amazing willingness to explain things two, or three, or more times... each as precisely and patiently as the first. Beyond the work bubble, Josh's steadfast friendship and conversation always served as a highlight of late nights and weekends over Fort Collins' all-too-minimal food selection. Thanks buddy.

Dealing with the trials of grad school, trivial to serious and everything in between, would not have been possible without my friends. Robert, the many hours of chatting science, and many more hours of chatting not science, were instrumental to my education and the maintenance of my morale. I look forward to many more. Michael and David, thanks for always giving me the opportunity to get out of the bubble entirely and suddenly be back in the old days. Ethan, Becca, Paul, Max, Amy, thanks for letting us grow a little family and showing me there is somehow more to life than work.

I'm infinitely thankful to my wonderful family for their love and support throughout graduate school and beyond. I would not be the person or scientist I am today without you.

TABLE OF CONTENTS

ABSTRACT ii
ACKNOWLEDGEMENTS iv
LIST OF FIGURES vii
1 Introduction 1
2 Pyrite Formation via Kinetic Intermediates Through Low-Temperature Solid-State Metathesis 12
2.1 Introduction 12
2.2 Materials and Methods 14
2.3 Results 16
2.4 Discussion 21
2.5 Conclusion 26
3 Circumventing Diffusion in Kinetically-Controlled Solid-State Metathesis Reactions 28
3.1 Introduction 28
3.2 Materials and Methods 30
3.3 Results 32
3.4 Discussion 38
3.5 Conclusions 42
4 Polymorph Selectivity of Superconducting $CuSe_2$ Through Kinetic Control of Solid-State Metathesis 44
4.1 Introduction 44
4.2 Materials and Methods 46
4.3 Results 50
4.4 Discussion 56
4.5 Conclusion 60
5 Lewis Base Mediated Polymorph Selectivity of Pyrite $CuSe_2$ Through Atom Transfer In Solid State Metathesis 62
5.1 Introduction 62
5.2 Materials and Methods 65
5.3 Results and Discussion 67
5.4 Conclusion 78
6 Outlook and Proposed Future Directions 80
6.1 Introduction 80
6.2 Materials and Methods 80
6.3 Using Molecules to Control Solid State Material Formation 83
6.4 Expanded Considerations for Precursor Selection 89
6.5 Advancing *in situ* Methods to Develop Kinetic Control 96
6.6 Applying Kinetic Control Design Rules to Real Systems 97

LIST OF FIGURES

1.1 Schematic reaction coordinate diagrams illustrating (a) thermodynamic control (b) kinetic trapping and (c) kinetic control. 2
1.2 Hypothesized pathways of solid state metathesis reactions 8

2.1 Cartoon depiction of a solid state metathesis reaction 13
2.2 DSC and PXRD of the products of the reaction $FeCl_2 + Na_2S_2$ executed at various temperatures 17
2.3 High Resolution Synchrotron PXRD patterns of the products of the reaction $FeCl_2 + Na_2S_2$ 18
2.4 PXRD of the products of the reaction $CoCl_2 + Na_2S_2$ executed at various temperatures 20
2.5 PXRD of the products of the reactions $MCl_2 + Na_2S_2$, M = Mn, Fe, Co, Ni, Cu, Zn 21

3.1 DSC and *in situ* PXRD of the reactions $MCl_2 + Na_2S_2$, M = Fe, Co, Ni, prepared in anhydrous conditions 33
3.2 DSC and relative mole fraction of the major reactants and products of the reactions $MCl_2 + Na_2S_2$, M = Fe, Co, Ni 35
3.3 DSC and *in situ* PXRD of the reactions $MCl_2 + Na_2S_2$, M = Fe, Co, Ni, prepared in ambient conditions 36
3.4 PDF of the air-exposed reactions $MCl_2 + Na_2S_2$ before annealing, M = Fe, Co, Ni 37
3.5 *In situ* PDF analysis of the reaction $FeCl_2 + Na_2S_2$, prepared in air 37
3.6 Cartoon illustrating diffusion- vs. nucleation-limited reaction pathways 42

4.1 Comparison of pyrite- and marcasite-structured $CuSe_2$ 45
4.2 Preparation of both polymorphs of $CuSe_2$ facilitated by air exposure 50
4.3 Physical properties of pyrite $CuSe_2$ 52
4.4 DSC, *in situ* PXRD, and phase fractions of the air-exposed reaction $CuCl_2 + Na_2Se_2$ 53
4.5 *In situ* PDF analysis of the air-exposed reaction $CuCl_2 + Na_2Se_2$ 55
4.6 Reaction scheme enabling polymorph selectivity and comparison of copper and selenium sublattices indicating the structural similarities between intermediates and products 56

5.1 PXRD patterns of the reaction $CuCl_2 + Na_2Se_2 + 0.1\,Ph_3P$ at 130 °C as a function of time 68
5.2 Mass spectrometry, magnetometry, and infrared spectroscopy analysis of the reaction products 69
5.3 XPS of the pyrite $CuSe_2$ product phases 70
5.4 Phase fractions of major products of the reaction $CuCl_2 + Na_2Se_2 + x\ Ph_3P$ as a function of x 71
5.5 ^{1}H NMR and ^{31}P NMR spectra of benzene-d_6 wash of products of the reaction $CuCl_2 + Na_2Se_2 + 0.97\,Ph_3P$ 73
5.6 PXRD patterns of the products of the reaction $CuCl_2 + Na_2Se_2$ with various molecules added 74

5.7 Cartoon scheme and hypothesized reaction pathway enabling polymorph selectivity via Ph_3P addition 78

6.1 PXRD of Fe + Se with and without triphenylphosphine flux 84
6.2 PXRD of Fe + S after reaction in a triphenylphosphine flux 86
6.3 Partial phase diagrams of Fe–S and Fe–Se 87
6.4 *In situ* PXRD patterns of the reaction $A_2S_2 + NiCl_2$, A = Na, K 90
6.5 Temperature dependent impedance spectroscopy of Na_2S_2 and K_2S_2 91
6.6 DSC of the reaction $A_2S_2 + Na_2S_2$, A = Na, K 92
6.7 Proposed reaction pathways of the reactions $A_2S_2 + Na_2S_2$, A = Na, K. 93
6.8 PXRD of NiSSe solid solutions formed from various precursor mixtures 94

1. Introduction[†]

The products formed in a chemical reaction are dependent on the pathway through which the reaction proceeds. The two canonical regimes of reactivity throughout synthetic chemical disciplines are either thermodynamically- or kinetically-limited reactions. Reactions that occur under thermodynamic control often have higher activation barriers, and in turn yield the products that are the most stable at thermodynamic equilibrium. Alternatively, if the activation energy can be lowered the reaction may proceed under kinetic control, in which the products that form the fastest may be stabilized, despite possibly not being the lowest energy configuration in the system.

While it is possible to access both kinetic and thermodynamic products in most synthetic molecular chemistry, solid state reactions yield a distinct challenge in dictating the reaction coordinate.[2,3] Approaches that overcome solid state diffusion become paramount: when atomic-scale mixing is not facilitated by a solvent or an intrinsic property of the reactants, other means must be used to promote reactivity.[4,5] The application of heat will provide the requisite energy to overcome the activation energy of diffusion to aid in mixing solid reactants; such heating often yields the product or products that are most stable since the system has sufficient thermal energy to relax into such a configuration.

In practice, this does not realistically limit the number of feasible synthetic targets available to the solid state chemist.[6] Though, while a large number of materials will invariably form at thermodynamic equilibrium, the formation of these materials occurs spontaneously

[†]Substantial portions of this introduction have been reproduced with permission from A. J. Martinolich and J. R. Neilson, *Chem. Mater.* **2017**, *29*, 479–489, reference 1, © 2017 the American Chemical Society

without control (Figure 1.1a). If one wants to rationally direct a reaction to prepare a new material with a specific structural motif or directed functional properties, metallurgical reactions are inadequate. Some stoichiometries of materials are metastable with respect to partial decomposition (e.g., $MS_2 \longrightarrow MS + S$, M = Mn, Cu, Zn)[7–9] while others are not (e.g., M = Fe, Co, Ni).[10–12] Additionally, polymorphs of the same stoichiometry may have vastly different properties that originate from the minor structural differences. A key example of this is the various polymorphs of TiO_2: slight changes in the connectivity of [TiO_6] octahedra have dramatic effects on the electronic band structure and thus the properties, and ranges of viable applications for the different polymorphs.[13]

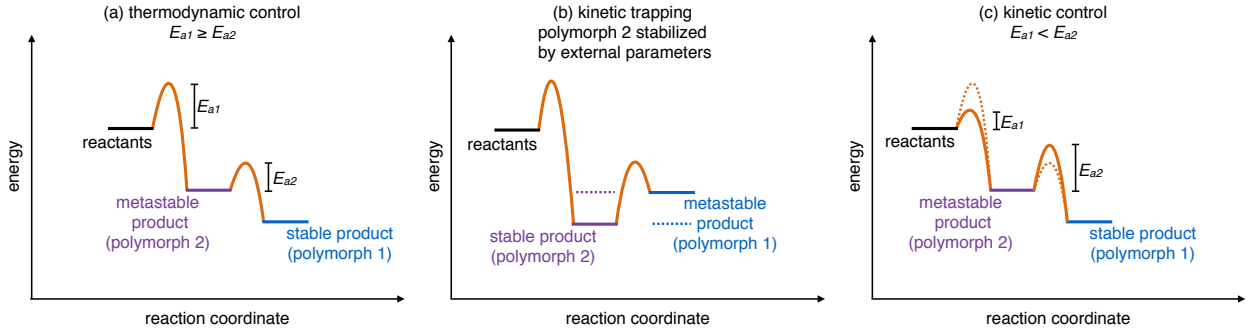

Figure 1.1: Schematic reaction coordinate diagrams illustrating (a) thermodynamic control (b) kinetic trapping and (c) kinetic control.

Thus, the synthetic pathway to form new materials must be altered in order to stabilize phases that are metastable under ambient conditions. In the case of MS_2 (M = Mn, Cu, Zn), combination of the elements requires the application of high pressure ($p > 10$ kbar) at approximately 1000 °C to stabilize the disulfide rather than the monosulfide phase.[14,15] Application of pressure and high temperature, followed by quenching, can be considered kinetic trapping (Figure 1.1b): at increased pressure, the ground state energy of a given material can change with respect to other configurations of the same material in another form (e.g., ZnS_2 vs. $ZnS + S$). This can also be achieved with temperature: at high tem-

perature, the hexagonal wurtzite polymorph of ZnS becomes thermodynamically favored over the cubic sphalerite phase.[9] Alternatively, extrinsic material factors such as particle size can be used. The thermodynamic stability of the three naturally-occuring TiO_2 polymorphs depends on the particle size because of their variable surface energies: while rutile forms in the bulk, the polymorphs anatase and brookite become thermodynamically stable with increasing specific surface area.[16]

Therefore, forming metastable materials in the bulk and without extreme applied conditions is a significant challenge. Achieving kinetic control, where the activation energies of solid-state reaction processes are altered in such a way that metastable materials can be accessed (Figure 1.1c) requires alternative chemistries to traditional high temperature solid state reactions; the key component of these alternative reactions is the facilitation of or lack of dependence upon diffusion between reactants. *Chimie douce* (i.e., "soft chemistry") often uses redox activity to either reductively or oxidatively intercalate or deintercalate ions into or out of a solid state structure, in turn maintaining the bulk framework but altering the electronic properties. A canonical example of this is the oxidative deintercalation of Li from $LiVS_2$ with I_2 in acetonitrile, which affords the layered, metastable VS_2 phase.[17] Direct combination of the elements, $V + 2\,S$, does not result in this phase, as suggested by the phase diagram.[18] In these oxidative deintercalation reactions, the rate limiting step is often diffusion of the alkali ion.[19] Additionally, complete or near-complete deintercalation can lead to a structural instability, which causes rearrangement of a layered crystal structure (e.g., $K_{1-x}Ni_2Se_2$) into a 3D-interconnected crystal structure (e.g., $K_{1-x}Ni_{2-y}Se_2$).[19] When the stability of the host lattice is maintained, multiple ion-exchange or (de)intercalation steps can be exploited to design new materials with predictable struc-

ture. This has been very fruitful in the preparation of perovskite-structured oxide ceramics, where the rigid oxide lattice allows multiple exchanges of the intercalated A-site cations, as shown by Wiley and coworkers[20] as well as Schaak and Mallouk.[21]

More recent work towards the preparation of tetrahedral transition metal chalcogenides such as FeS, CoS, and CoSe via (de)intercalation by Rodriguez and coworkers demonstrates the versatility of the technique in gaining kinetic control of solid phase transformation. For example, the metastable superconductor FeS can be intercalated by alkali metal hydroxides under various conditions to produce new superconducting phases. The superconducting properties are strongly dependent on the synthetic method, where the temperature of the intercalation must be kept below 160 °C and the conditions must be reducing.[22] In the cases of CoS and CoSe, the deintercalation of potassium from KCo_2S_2 and KCo_2Se_2 is achieved at room temperature; higher temperatures yield decomposition of the tetragonal cobalt chalcogenides to the thermodynamically stable Co_9Q_8 and hexagonal $Co_[(_1-x)]Q$ phases, indicating the metastable nature of the deintercalated phases.[23]

Another important, though somewhat under-explored, feature of *chimie douce* reactions is the ability to oxidize the anions in the lattice as well as the cation.[24] This is achieved through oxidative deintercalation from covalent systems, in which the charge is more delocalized and upon oxidation the electron is not necessarily removed from the cation. This leads to anion-anion bond formation and new metastable materials. Though pioneering work in this field occurred in the early 1990s, there remain many open questions in the development of these techniques to fully understand how much control over the reactivity of the anions can be achieved. This has become especially relevant with the discovery of

redox-active anions in intercalation cathodes in batteries, yielding higher overall capacities at high voltages.[25]

Anion deintercalation and exchange in extended inorganic solids also yields an electronically altered material with a crystal structure that is related to the precursor. Reaction of alkali hydrides with various metal oxides can yield 2D layered structures with unusually low oxidation state metals (e.g., Co(I) and Ni(I))[26,27] as well as magnetic oxyhydride materials.[28] Kageyama and coworkers have shown that hydride reduction of $BaTiO_3$ yields an electronically conducting mixed valence Ti^{3+}/Ti^{4+} material, and that the hydride anion in $BaTiO_{(3-x)}H_x$ is surprisingly labile.[29] This lability was then exploited as a facile route to oxynitride materials by then reacting the hydride under NH_3 (g),[30] and surprisingly even under N_2 gas at 400 °C.[31] Additional investigation of the nitridation of $EuTiO_3$ indicated that use of the hydride precursor allows nitrogen exchange at much lower temperatures, and a more complete exchange of nitrogen into the lattice via enhanced anion diffusion pathways, yielding a kinetically stable oxynitride perovskite.[32] These examples of topotactic modification to derive kinetically-mediated metastable phases have tremendous utility, but are limited in the sense that a relationship to the original crystalline lattice of the precursor material is typically required. The lability of the hydride anion has also been exploited in the direct preparation of $Ba_{1-x}K_xFe_2As_2$ superconductors from alkali and alkaline earth hydrides reacted with iron arsenide, which significantly increases the reaction kinetics and yields comparable materials to slow elemental reactions.[33]

Another solid state synthetic approach that has the potential to provide kinetic control is the use of reactive, alkali (poly)chalcogenide fluxes. Work in the late 1980s and early 1990s by Ibers and coworkers[34–36] as well as Kanatzidis and coworkers[37,38] was successful

in producing kinetically-stable materials using varieties of A_2Q_x (A = Na, K; Q = S, Se, x = 1–5) with low melting temperatures to facilitate mixing. The fluxes are corrosive and oxidizing and often yield the inclusion of polychalcogenide anions into the crystal structures of the products. These polyanions are only kinetically stable and disproportionate to the thermodynamically favored chalcogenide and the elemental chalcogen if metallurgical approaches are used. More recently, *in situ* spectroscopic[39] and diffraction[40] studies of flux mixtures and reactions provide a deeper understanding of the structure and reactivity of these fluxes. Depending on the polysulfide composition in mixtures of $K_2S_3 + K_2S_5$, the local structure of the liquid flux is strongly altered. Additionally, input stoichiometry, heating rate, and flux composition can yield a range of new materials that are transiently stable at various temperatures heating and cooling in the flux. For example, the new phases $K_5Sn_2S_8$ and $K_4Sn_2S_6$ are formed when reacting tin metal in K_2S_5, discovered using *in situ* PXRD. If instead K_2S_3 is used, another new phase, $K_6Sn_2S_7$, is observed.[40] These fundamental studies are integral in determining kinetic pathways to new functional materials.

Another notable example of kinetic control in preparing new solid state materials is the use of the modulated elemental reactant method. In this method, precisely controlled thicknesses of various elemental reactants are deposited as ultra-thin films onto a substrate sequentially.[41–43] The layered elemental reactants are then annealed to yield a homogeneous amorphous intermediate; further annealing directly crystallizes the product, which is often metastable. The sequential deposition of very thin layers of the various elements is key in reducing the diffusion lengths in the films, which promotes mixing before crystalline phase nucleation. This, along with the low temperatures required to permit nucleation only rather than complete structural rearrangement,[44] has allowed the prepa-

ration of many ternary and quaternary[45,46] solid state materials without first nucleating binary phases,[47,48] as well as the formation of many metastable phases.[41,44,49]

Gaining kinetic control in materials synthesis has provided various materials chemistry breakthroughs. The intercalation of lithium, lithium amide, and ammonia in between the layers of superconducting FeSe increases the transition temperature from 8 K to 43 K.[50] Observing kinetic processes in applied systems is very important in understanding their function, such as cycling rate-dependent formation of Li_xFePO_4 solid solution phases in battery cathodes,[51] as well as comprehensive studies of the reaction mechanisms in intercalation[52] and conversion[53,54] type cathodes. Further investigation of kinetic systems, both fundamental and applied reactions, will allow breakthroughs in the discovery and design of new functional materials.

We have recently shown the role of kinetic control in solid-state metathesis (double-ion exchange) reactions. These reactions are driven by the formation of stoichiometric equivalents of a thermodynamically stable byproduct (e.g., NaCl), along with the targeted material. Initial investigations into this field by Kaner and Parkin in the early 1990s yielded spectacular results. Combination of various transition metal halide salts with various alkali-chalcogenide and alkali-pnictide salts would rapidly self-propagate upon mixing, igniting even under inert atmospheres to yield refractory compounds such as transition metal borides and nitrides.[55–58] The larger ΔH_f° of these reactions than the analogous metallurgical reactions is due to the formation of multiple equivalents of a binary salt (e.g., NaCl). These self-propagating reactions often heat the mixture to above the melting point of the salt byproduct to form a flux which allows the counterions to mix and form highly crystalline transition metal compounds. Thus, this approach is amenable for forming hard,

refractory materials from constituent elements that are otherwise kinetically inert when combined metallurgically.[59,60]

While the rapid self-heating to extreme temperatures that occurs in these reactions does not readily permit the imposition kinetic control, a range of efforts were put forth to determine the driving forces and tunability of these reactions. Reaction conditions such as overall heat capacity and particle size could be altered to promote or inhibit self-propagation. Calculation of the adiabatic temperature (that is, the temperature that the reaction mixture would reach if no heat was lost to the environment) was used as an approximate gauge to tell if the reactions would ignite.[61] If enough heat was released to heat the salt product to a melt, it was observed that the reactions would self-propagate. These initial forays into dictating the pathway and outcome of solid state metathesis reactions provide a promising narrative for the bulk of this perspective.

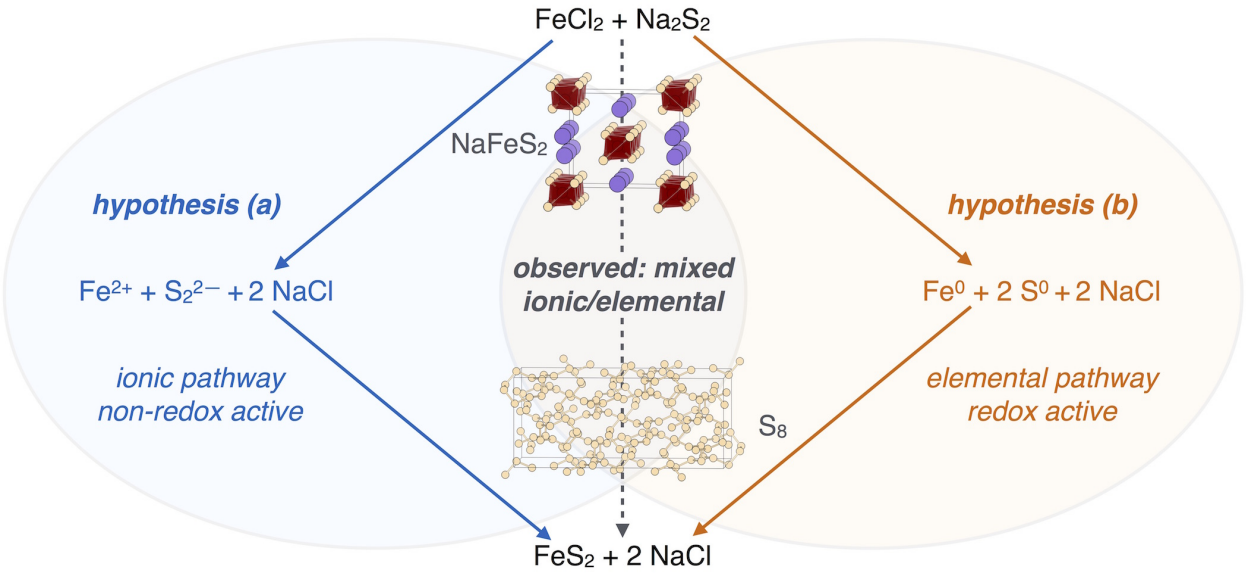

Figure 1.2: The two pathways hypothesized for solid state metathesis reactions. The reactants could either progress through (a) ionic intermediates, where the products would form from facile ion exchange, or from (b) elemental intermediates where the constituents are redox-active and likely driven by the rapid heating of the reaction mixture by the formation of NaCl. The observed intermediates indicate a combination of both pathways at play in solid state metathesis reactions.

Initial hypotheses surrounding the reaction pathways of these solid state metathesis reactions suggested that they progress through either ionic or elemental intermediates (Figure 1.2).[57,62] The ionic pathway would proceed through facile ion exchange and indicate that the reactions are not redox-active; however, a hypothetical transition state might be electrostatically disfavored. Alternatively, the elemental pathway would progress through elemental intermediates that are formally reduced or oxidized *in situ* before being reoxidized or rereduced to form the expected products. There, the multiple electron-transfer steps may be disfavored. These limiting extremes inspired our subsequent experiments to understand the reaction pathways of these ion-exchange reactions.

The following body of work aims to achieve kinetic control over solid state metathesis reactions. It can broadly be broken into two distinct sections over the next four chapters. Chapters two and three are focused on simply understanding the pathway through which solid state metathesis reactions occur. In chapter two, the reactions targeting transition metal disulfides ($M\mathrm{S}_2$, $M =$ Mn, Fe, Co, Ni, Cu, Zn) are studied to provide insight into the mixed ionic and elemental pathways that occur, which is informed through the use of high resolution synchrotron powder X-ray diffraction. The limitations of solid state metathesis reactions are also outlined, in that only the thermodynamically stable products are observed despite the low temperatures that are used to drive the reactions to completion.

Chapter three reports the ability to change reaction pathway through air exposure of the reactants. This drives the reactants to mix fully upon slight hydrolysis of the precursors by atmospheric water, and forms a well mixed, homogeneous, amorphous metal sulfide intermediate. Annealing the amorphous intermediates yields direct nucleation of

the targeted phase with the desired stoichiometry. The use of *in situ* synchrotron powder X-ray diffraction allows the reactions to be studied as they happen and a number of salient features of the reactions, proceeding though both diffusion- and nucleation-limited pathways, to be determined.

The insights into controlling the reaction pathway are then exercised to produce the metastable superconducting phase cubic $CuSe_2$. In chapter four, the ability to produce well-mixed intermediates and decouple the formation of salt from the formation of the products is exploited to form the metastable phase. The formation of structurally related intermediates that can then rearrange upon gentle heating is the key to forming the metastable $CuSe_2$. Previously, the preparation of the cubic $CuSe_2$ phase from the elements was only achievable at extreme temperatures and pressures.

Chapter five aims to exert more control over the formation pathway towards cubic $CuSe_2$ via inclusion of a reactive small molecule in the solid state metathesis reaction to replicate the effects of air exposure. It is found that the if the the Lewis base triphenylphosphine is present, it acts as a molecular shuttle that can promote the reaction at low temperatures, and again produce the desired metastable product. Comparing to a range of other small molecules, it is determined that the additive must be Lewis-basic and also a liquid at the reaction temperature.

The final chapter outlines possible future work stemming from these studies. Continuing with solid state metathesis, considerations regarding the specific properties of the reactants and products to control the reaction pathway should be investigated, with a brief case study on ion size and mobility provided. Beyond metathesis, development of new reaction schemes in which diffusion can be promoted at low temperatures is suggested. An

example of this, the use of triphenylphosphine to produce tetragonal FeSe (a superconductor with limited phase stability) is provided. More generally, the development of ways to understand solid state chemical reactions as they happen and in more varied and applied systems is addressed.

Note on author contributions: Portions of this chapter were published in *Chemistry of Materials*, **2017**, vol. 29, page 479, by Andrew J. Martinolich and James R. Neilson. The initial draft was written by AJM and both authors contributed to the editing and finalization of the manuscript. JRN supervised the research.

2. Pyrite Formation via Kinetic Intermediates Through Low-Temperature Solid-State Metathesis[†]

2.1. Introduction

The formation of solids illustrates the competition of thermodynamics and kinetics: while there is often a thermodynamic driving force to form a compound, the kinetic barriers from solid-state diffusion make materials by design extremely challenging.[64] Therefore, the solid-state chemist often relies on high-temperature reactions in order to produce a desired phase, assuming that the desired phase is thermodynamically stable. Alternatively, self-heating solid-state metathesis reactions have been used extensively in the formation of refractory and super-hard compounds, such as sulfides, nitrides, borides, carbides, and silicides.[55,57,58,60,62] With some precursors, the solid-state metathesis reaction does not proceed immediately with rapid self-heating and is instead only proceeds with the application of heat over a period of time.[65] Along these lines, metathesis has been integrated into aerosol-assisted formation pathways of nanomaterials.[66] These formation pathways have also been used to form transition metal chalcogenide materials, and further integration of metathesis may allow control over the formation of size and shape of resulting nanoparticles, which may in turn alter their properties as the crystallite size decreases.[67] The use of solid-state metathesis at low temperatures, under conditions without extensive self-

[†]Substantial portions of this chapter have been reproduced with permission from A. J. Martinolich and J. R. Neilson, *J. Am. Chem. Soc.* **2014**, *136*, 15654–15659, reference 63, © 2014 the American Chemical Society

heating, presents many opportunities for the solid-state chemist to maintain increased control over reactions to control the formation of designer materials.

A compound of great interest for energy applications and geosciences is iron pyrite, FeS_2. As a compound that melts incongruently ($T_{\text{decomp}} = 743$ °C) that is comprised of high-melting iron and volatile sulfur, its preparation from the elements at ambient pressure can require long reaction times at high temperature and is not guaranteed to achieve stoichiometric completion due to the formation of many other sulfur deficient compounds;[10,68] excess sulfur is often used to generate the high fugacity needed to drive stoichiometric completion of the reaction.[69] Many transition metal disulfides form pyrite polymorphs, ranging across the period from MnS_2 to ZnS_2; however, MnS_2, CuS_2, and ZnS_2 are all high-pressure phases.[14,15,70] The properties of the pyrite change dramatically with metal substitution, ranging from antiferromagnetic insulators to superconductors.[15,71–74] With the appropriate synthetic tools in hand, it may become possible to prepare novel related phases that would be otherwise unattainable through metallurgical preparatory routes.

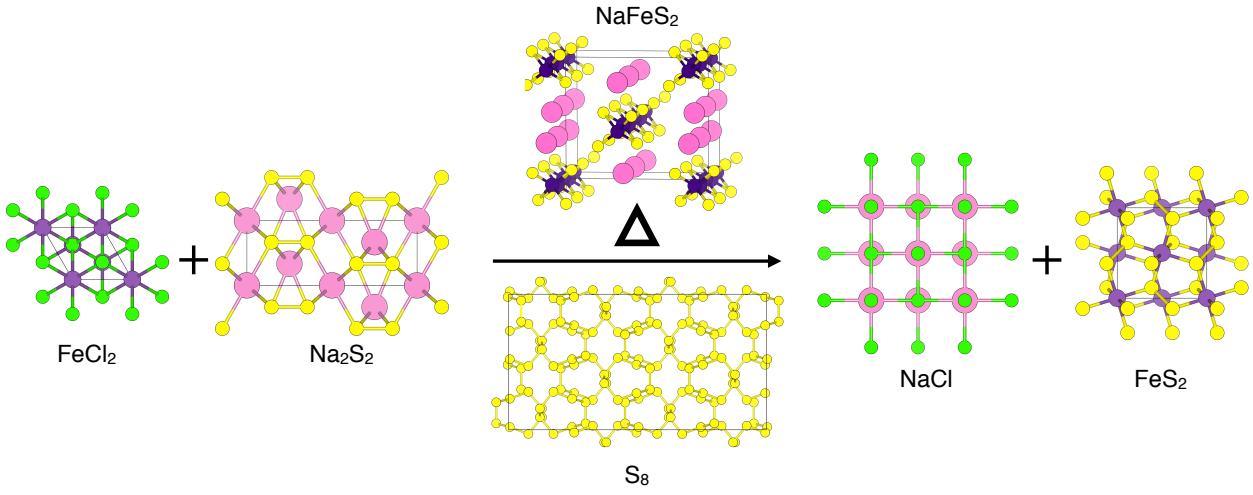

Figure 2.1: Schematic description of the metathesis reaction. Upon heating, iron chloride and disodium disulfide react to form sodium chloride and iron disulfide in the solid state. The reaction proceeds through metathesis, forming sodium iron sulfide and sulfur as reaction intermediates.

Here, the salt-exchange metathesis reactions of metal dihalides with disodium disulfide,

$$\mathrm{Na_2S_2} + M\mathrm{Cl_2} \longrightarrow M\mathrm{S_2} + 2\,\mathrm{NaCl} \tag{2.1}$$

where M is a divalent 3d transition metal; Mn^{2+}, Fe^{2+}, Co^{2+}, Ni^{2+}, Cu^{2+}, and Zn^{2+} are investigated. The formal reaction, as written, would correspond to a simple salt exchange, where the dimeric persulfide $[S_2]^{2-}$ polyanion exchanges 2 Na^+ cations for M^{2+}, as the pyrite lattice is comprised of the octahedral coordination of M^{2+} by $[S_2]^{2-}$ dimers (Figure 2.1).[75] This metathetical reaction at low temperature (T_{rxn} =350 °C) yields formation of high purity compounds that are thermodynamically stable at ambient pressures (FeS_2, CoS_2, and NiS_2). While this metathesis reaction reaches stoichiometric completion in the end, high-resolution synchrotron powder x-ray diffraction (HRSXRD) data suggest a far more complex mechanism than crystal chemistry would suggest, or through reductive recombination to the elements or ionic exchange as previously hypothesized.[55,65,76,77]

2.2. Materials and Methods

Note on author contributions: This chapter was published in *Journal of the American Society*, **2014**, volume 136, page 15654, by Andrew J. Martinolich and James R. Neilson. AJM performed the experiments, analyzed the data, and wrote the initial draft of the manuscript. JRN analyzed data and supervised the project. All authors contributed to the editing and finalization of the manuscript.

All reagents were purchased from Sigma Aldrich or NOAH Technologies at a purity of 98% or higher. Sulfur was additionally purified through vapor transport in an evacuated

sealed tube with a temperature gradient from 550 °C to 400 °C. The impurities were left in the hot end of the tube while sulfur condensed in the cooler end of the tube as the vessel cooled.

Na_2S_2 was prepared from the elements in a manner with which to avoid direct contact of the elements which could produce an exothermic thermite reaction. In an argon-filled glove box, sodium and sulfur were placed in separate alumina crucibles and sealed in the same silica tube, with the sulfur on top. The tube was then evacuated to < 10 mTorr and sealed without exposure to the atmosphere. The tube was then heated to 200 °C for 24 hours to allow sulfur vapor to corrode the sodium. The resulting heterogeneous solid was homogenized and pelleted in the glove box, resealed, and heated for an additional 12 hours at 300 °C.

For the solid-state metatheses of MS_2, anhydrous MCl_2 and Na_2S_2 were ground to a homogenous powder and pelletized in an argon-filled glove box. The pellet was then placed in an alumina crucible and sealed in a quartz tube, evacuated to < 10 mTorr without exposure to the atmosphere. The reaction vessel was then heated at 1 °C min^{-1} in a box furnace to the specified temperature for 24 hours and furnace cooled. The product was then recovered in an argon glove box, washed 5 times with anhydrous methanol under an inert atmosphere using Schlenk techniques, dried under vacuum at room temperature, then recollected in the glove box.

Purity of the Na_2S_2 was confirmed by x-ray diffraction using a Bruker APEX II single crystal diffractometer (MoKα radiation, $\lambda = 0.7107$ Å) with powder in a sealed quartz capillary; the two-dimensional data were radially integrated for analysis. Powder x-ray diffraction data (PXRD) were collected on a Scintag X-2 Diffractometer with CuKα ra-

diation. High-resolution synchrotron powder x-ray diffraction data were collected from powders sealed in quartz capillaries loaded into Kapton® capillaries on the beam line 11-BM-B ($\lambda = 0.413673$ Å).[78] Rietveld analyses were performed using EXPGUI/GSAS.[79,80] Physical properties measurements were performed using a Quantum Design, Inc. Dynacool PPMS, using the electronic transport option and vibrating sample magnetometer. Differential Scanning Calorimetry was performed on samples hermetically sealed in the glove box using a TA Instruments 2920 Modulated DSC with a 1 °C min^{-1} ramp rate in order to replicate the reaction conditions.

2.3. Results

From differential scanning calorimetry (DSC), significant exothermic events occur on heating the reaction even after the formation of NaCl (Figure 2.2a). Both thermodynamic and kinetic effects are required to reconcile the DSC and powder x-ray diffraction (PXRD) data. From PXRD of a 24 hour reaction, NaCl forms by 50 °C (Figure 2.2b); however, the DSC trace with a heating rate of 1 °C min^{-1}, shows that all exothermic processes occur above ∼100 °C (Figure 2.2a). This suggests that there is a low activation barrier for NaCl formation, but the formation is kinetically slow below 100 °C due to the requisite diffusion through the solid matrix. Furthermore, a pressed pellet of $FeCl_2$ and Na_2S_2 slowly darkens from pale yellow to black over the course of ∼2 months in either an inert or dry O_2 environment at room temperature, indicative that a reaction is taking place very slowly.

When an exotherm is triggered by heating to 175 °C, the reaction is far from complete, even after 24 hours of equilibration, as indicated by the small mole fraction of FeS_2 visible

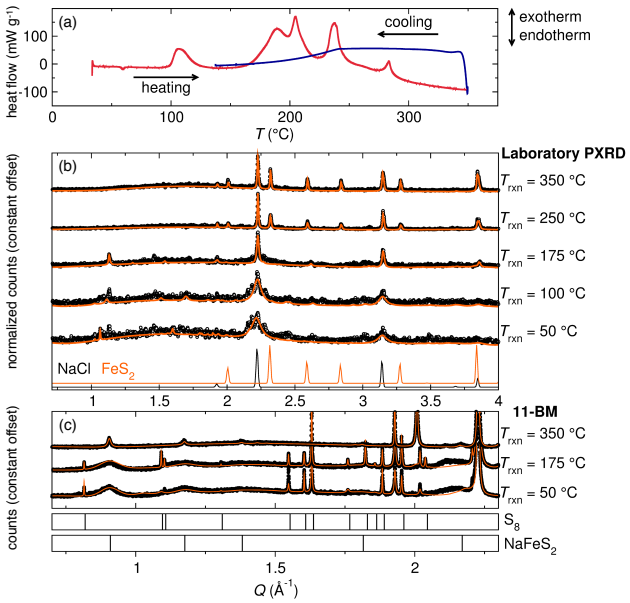

Figure 2.2: (a) DSC of the reaction of $FeCl_2$ with Na_2S_2 shows multiple exothermic processes as the temperature of the reaction increases. The data are normalized per gram of total reaction mixture. (b) PXRD patterns (black symbols) and corresponding fits determined through the Rietveld method (orange lines) of the reaction at the temperatures shown. NaCl formation is seen throughout, while FeS_2 is not seen until T_{rxn} =250 °C. (c) HRSXRD patterns of the same reaction products show S_8 formation at low reaction temperatures, as well as a significant diffuse background component indicative of a disordered phase, which crystallizes into $NaFeS_2$. [data plotted as $Q = 4\pi sin(\theta)/\lambda$, $\lambda = 1.5418$ Å for (b) and $\lambda = 0.41367$ Å for (c)]

in the product (Figure 2.2b,c; Table 2.1). At temperatures greater than 175 °C, there is sufficient thermal energy (for diffusion and other activated processes) as to allow for reaction completion.

HRSXRD of the reaction of $FeCl_2$ and Na_2S_2 at 350 °C reveals quantitative reaction completion and high-purity FeS_2. Rietveld analysis of the HRSXD data reveals 68.4(2) mol% NaCl and 30.4(2) mol% FeS_2 (Figure 2.3a). The remaining 1.3(2) mol% is monoclinic $NaFeS_2$.[81] The $NaFeS_2$ and NaCl were washed away with anhydrous methanol, which resulted in 99.63(1)% phase-pure pyrite FeS_2, along with a 0.37(7) mol% of Fe_7S_8 impurity (Figure 2.2b); this small phase fraction was further confirmed by determination of the ferromagnetic response of the sample, which also confirms less than 1 mol% of a Fe_7S_8 impurity.

The Fe_7S_8 phase was not observed in the diffraction data before washing, and may have formed through decomposition of the $NaFeS_2$ or minor oxidation of the pyrite FeS_2 upon washing. Electronic transport measurements were performed on cold-pressed pellets and show an increase in resistivity upon cooling, confirming the material's bulk semiconducting nature.

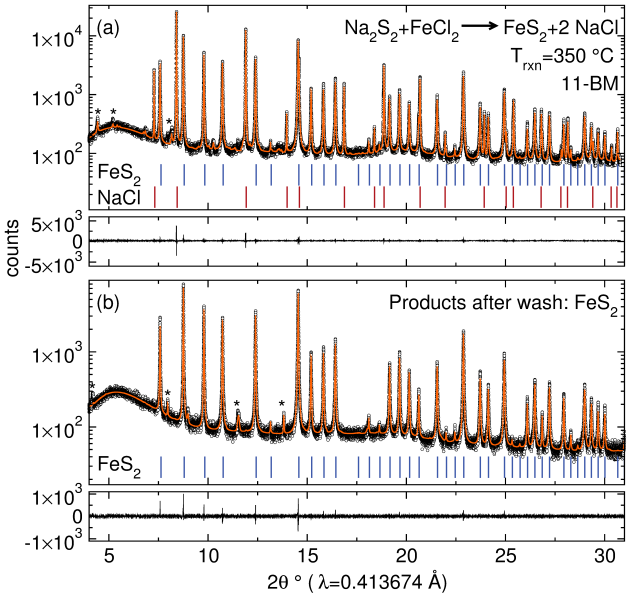

Figure 2.3: HRSXRD and Rietveld analysis of the products of reaction 1 (a) before and (b) after washing with anhydrous methanol, showing the data (black circles), calculated fit (orange lines) and difference between the two (black lines). Ticks below the data indicate expected reflections. Asterisks in (a) denote monoclinic $NaFeS_2$, 1.3(2) mol%. Asterisks in (b) denote Fe_7S_8, 0.37(7) mol%. Minority phases were incorporated into the refinements; their reflections were omitted for clarity.

While the reaction achieves stoichiometric completion by $T_{rxn} = 350$ °C (*i.e.*, with seemingly little activation barrier), it does not do so through topochemical transformations or diffusive salt exchange. There is extensive redox chemistry that takes place, as indicated by the formation of several crystalline intermediates. HRSXRD data of the products from incomplete reactions ($T_{rxn} = 50$ and 175 °C) yield insight into the reaction pathway (Figure 2.2c). The diffraction patterns have an appreciable, diffuse, non-crystalline backgrounds, as well as broad humps which sharpen at $T_{rxn} = 350$ °C and index to the expected

Table 2.1: Phase fractions at different reaction temperatures from analysis of the reaction products of Eqn. 1 by High-resolution Synchrotron PXRD (SXRD) and laboratory PXRD (PXRD) for M= Fe^{2+} and Co^{2+}.

	M = Fe^{2+}; Mole percent (PXRD/SXRD)			
T_{rxn}	NaCl	FeS_2	S_8	$NaFeS_2$
50 °C	98(1)/86.1(1)	0/0	1.4(2)/7.25(3)	0.8(2)/6.70(5)
100 °C	97(1)	0	3.0(3)	0.45(4)
175 °C	88(2)/87.0(1)	0/3.49(5)	1.4(5)/3.97(3)	10.8(5)/5.59(4)
250 °C	60(3)	39(2)	0	0
350 °C	70(2)/68.3(1)	30(1)/30.37(6)	0/0	0/1.28(2)
	M = Co^{2+}; Mole percent (PXRD)			
T_{rxn}	NaCl	CoS_2	Na_2CoS_2	CoS
100 °C	97(1)	0	2.5(7)	0
175 °C	92(1)	0	8(1)	0.7(4)
250 °C	85(2)	14(3)	0	0[a]
350 °C	73(1)	13(4)	0	11.0(9)[b]

[a] Also includes 0.36(4) mol% Co_9S_8. [b] Also includes 2.7(4) mol% Co_3S_4.

reflections of monoclinic $NaFeS_2$. The observation of $NaFeS_2$ is surprising, as it would indicate the formal oxidation of Fe^{2+} to Fe^{3+} and reduction of $[S_2]^{2-}$ to 2 S^{2-};[82] there are no persulfide dimers in the structure of $NaFeS_2$ that would indicate a lesser negative charge on the sulfur.

At both intermediate temperatures, there are also numerous, sharp, low-Q reflections; all of which index to orthorhombic S_8,[83] suggesting that there is also formal oxidation of the $[S_2]^{2-}$ to 2 S^0. However, crystalline sulfur is not present in the HRSXRD data of the 350 °C reaction and did not condense in the sealed ampoule; this suggests that sulfur also participates as an intermediate in the reaction mechanism. By HRSXRD, no pyrite is observed at 50 °C but crystallites are detected in the T_{rxn} =175 °C products (Figure 2.2c, Table 2.1).

Similar trends are seen in the temperature dependent reaction of $CoCl_2$ and Na_2S_2 (Figure 2.4). At low temperatures, Na_2CoS_2 is observed, which has an analogous structure to $NaFeS_2$; the extra sodium compensates for the divalent charge of Co^{2+} with sulfide, S^{2-} anions. While comparable to the reaction with iron chloride, CoS_2 formation is more

sensitive to temperature. At $T_{rxn} = 350$ °C, CoS_2 formation is accompanied by the sulfur-deficient phases CoS and Co_3S_4. Despite CoS_2 being stable up to 950 °C,[11] progression through this reaction pathway may be altered by the increased mobility of the sulfur. As the reaction temperature is increased, we infer the volatilization of the sulfur intermediate overcomes the favorability of CoS_2 formation, leading to these sulfur-deficient phases.

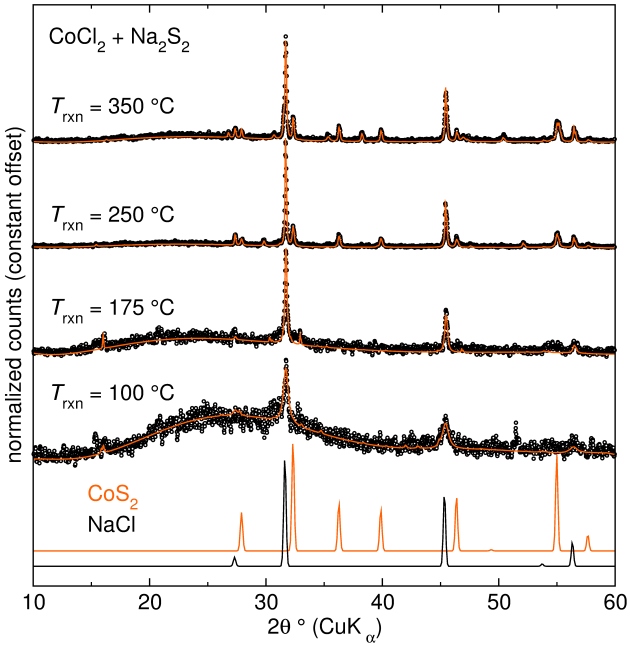

Figure 2.4: PXRD patterns of the products from the solid-state metathesis reactions of CoS_2 with Na_2S_2 (black circles) and corresponding Rietveld analyses (orange lines) at various temperatures. At low temperatures, S_8 and Na_2CoS_2 are detected. At increased temperatures, the formation of sulfur deficient phases Co_3S_4, CoS, and Co_9S_8 are detected, despite the stability of CoS_2 up to 950 °C.

In reactions with MCl_2, (M = Mn, Fe, Co, Ni, Cu, and Zn) only the FeS_2, CoS_2, and NiS_2 pyrite are formed (Figure 2.5). Only these pyrite-type compounds are found on the binary phase diagrams determined for near ambient pressures.[7,9–12,84] While pyrite MS_2 phases have been reported at non-ambient pressures for manganese, copper, and zinc,[14,15,70] the thermodynamically favorable phases of MnS, CuS, and ZnS are observed, with the remnant

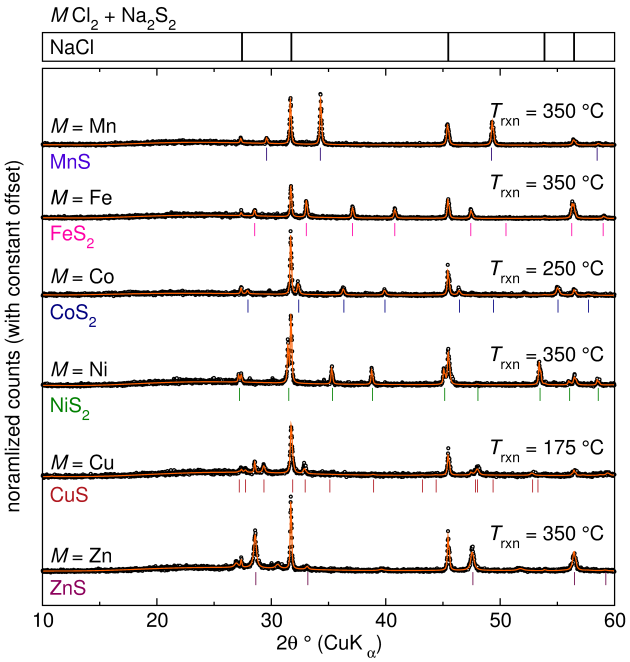

Figure 2.5: PXRD patterns of the products from the solid-state metathesis reactions of divalent transition metal chlorides with Na_2S_2 (black circles) and corresponding Rietveld analyses (orange lines) display the formation of either MS or MS_2, as shown by the expected reflections under each pattern. The formation of NaCl is conserved. CuCl and wurtzite ZnS were also incorporated into the respective Rietveld refinements, ticks were omitted for clarity.

sulfur condensing on the on the side of the ampoule as it cooled according to the reaction:

$$\mathrm{Na_2S_2} + M\mathrm{Cl_2} \longrightarrow M\mathrm{S} + \mathrm{S}_{(g)} + 2\,\mathrm{NaCl} \tag{2.2}$$

The reaction with $ZnCl_2$ produced a mixture of the high- and low-temperature polymorphs of ZnS, with the wurtzite and zinc blende structures, as previously shown.[65]

2.4. Discussion

By correlating features in the DSC to changes in the observed phases, we can elucidate the elusive mechanism for these low-temperature solid-state metathesis reactions. Primarily, the melting or decomposition of any reagents during the reaction can be ruled out.

Na_2S_2 does not decompose until 470 °C, and $FeCl_2$ does not melt or decompose until 677 °C.[85,86] While Na_2S_2 undergoes a structural phase transition at 170 °C,[85] crystalline Na_2S_2 is not observed in any of the x-ray diffraction patterns. This precludes formation of either S^{2-} or Fe^{3+} ions through decomposition of the reactants and must result from their reaction.

Sodium chloride provides a driving force to initiate the reaction; however, it does not provide a driving force to drive the reaction to completion. NaCl formation is observed by XRD at lower temperatures ($T_{rxn} = 50$ °C) than the exothermic release just above $T = 100$ °C observed from DSC (Figure 2.2). Furthermore, the exothermic processes shown here contrast the formation of pyrite NiS_2 from the previously reported metathesis reaction of K_2NiF_6 and 2 $Na_2S_5 \cdot 0.06$ H_2O. There, a vigorous exothermic reaction occurs around T_{rxn} ∼65 °C, with a peak heat flow of ∼1700 mW g^{-1}.[76] Here, the maximum heat flow is ∼200 mW g^{-1}, reflecting a weaker overall driving force and ability to follow the reaction intermediates. Taken together, these results indicate that a small amount of thermal energy is required for diffusion, which is sufficient to initiate the formation of NaCl, but not the pyrite phase.

The exothermic release just above $T = 100$ °C corresponds to the formation of NaCl and formation of a poorly ordered $NaFeS_2$ phase. In the DSC experiment, the heating rate was 1 °C/min, which is not likely slow enough to observe completion formation of NaCl below 100 °C; therefore, the formation of NaCl at lower temperatures is not likely. Furthermore, there is a significant increase in the NaCl diffraction intensity (with a decrease in peak width) when comparing the $T_{rxn} = 50$ °C and $T_{rxn} = 175$ °C diffraction data. The same trend is observed during the formation of CoS_2 (Figure 2.4). The comparison of the prod-

ucts from these two reaction temperatures also shows a significant increase in the amount of $NaFeS_2$ (or Na_2CoS_2) present in the product (Table 2.1). Furthermore, there is not a substantial increase in the intensity of the diffraction from NaCl between the $T_{rxn} = 175$ °C and $T_{rxn} = 350$ °C diffraction data in either the iron or cobalt containing products; however, quantification of this change is not straightforward. Together, these imply that the initial exotherm is the initiation of the reaction through formation of NaCl and $NaFeS_2$ (or Na_2CoS_2), with a low activation barrier that is rapidly overcome by heating to 100 °C:

$$\mathrm{FeCl_2 + Na_2S_2 \xrightarrow{E_a \sim 100^\circ C} NaFeS_2 + NaCl + \tfrac{1}{2}\,Cl_{2(g)}.} \tag{2.3}$$

The theoretical enthalpy of this reaction is $\Delta H_{rxn} = -2.8$ kJ mol^{-1} (since ΔH_f°($NaFeS_2$) = –331.3 kJ mol^{-1} [87]). Such a reaction is barely exothermic, which would explain the small exotherm observed in DSC that is concomitant with the observation of $NaFeS_2$ and NaCl. The thermochemistry of the reaction,

$$\mathrm{NaFeS_2 + \tfrac{1}{2}\,Cl_{2(g)} \longrightarrow FeS_2 + NaCl,} \tag{2.4}$$

is strongly exothermic relative to Eqn. Equation 2.5, as $\Delta H_{rxn} = -258.4$ kJ mol^{-1}. The presence (or absence of) $Cl_{2(g)}$ [or $S_8(s)$] does not influence the thermochemical calculation; therefore, it is clear that the significant exotherm observed above $T > 175$ °C must arise from the formation of FeS_2 and NaCl.

From a control reaction, it was confirmed that Cl_2 gas is not evolved. The reaction was performed in the presence of a sodium metal getter, with the reaction mixture in a crucible

on top of a crucible containing the sodium and both crucibles sealed into an evacuated SiO_2 ampoule. The expectation would be that if chlorine gas were being produced, NaCl would form on the surface of the liquid sodium metal. After reaction at 350 °C for 24 hours, no NaCl was formed, but instead Na_2S was found in the getter crucible. Accordingly, the reaction mixture of $FeCl_2$ and Na_2S_2 formed FeS and NaCl. Since Cl_2 was not detected, it provides evidence that the chlorine must be integrated into the low-density $NaFeS_2$ intermediate.

After heating the mixture of Na_2S_2 and $FeCl_2$ at 175 °C for 24 hours, one observes $NaFeS_2$, S_8, and NaCl. From the analysis of density functional theory calculations, $NaFeS_2$ is reported to be unstable with respect to decomposition into FeS_2, FeS, and Na_2S.[88] This is further confirmed by our attempts to prepare $NaFeS_2$, which were unsuccessful. Preparation of related compounds is best achieved by reaction of the alkali with the transitional metal chalcogenide as a pre-reaction, followed by homogenization and reaction at elevated temperature.[19,89–92] Reaction of FeS_2 with sodium metal yielded only FeS_2, Na_2S, and a sulfur-deficient $FeS_{(2-x)}$ phase. Instead, preparation of $NaFeS_2$ requires the leaching of aqueous suspensions or electrochemical means.[81,82,87] These findings further implicate $NaFeS_2$ as an intermediate phase in the reaction.

Collectively, these data provide insight into the complete mechanism of pyrite formation *via* metathesis. The metathesis reaction does not appear to be limited by solid-state diffusion, even at room temperature, and the reaction does not appear to be susceptible to thermal runaway. Rather than the simple salt exchange between Fe^{2+} and $[S_2]^{2-}$, there appears to be a more complicated reaction mechanism predicated on the formation of low-density crystalline intermediates. From XRD, it is apparent that NaCl forms first, while the

Fe and S combine to form the intermediates $NaFeS_2$ and S: $FeCl_2 + Na_2S_2 \longrightarrow x\ NaCl + y\ NaFeS_2 + z\ S \longrightarrow FeS_2 + 2\,NaCl$. However, this does not stoichiometrically balance with chlorine, and chlorine gas was not detected.

Therefore, we speculate that the reaction may proceed through the formation of NaCl, and attack of the $FeCl_2$ lattice by sulfur through dispropotionation of the persulfide anion, $[S_2]^{2-} \longrightarrow S^{2-} + S^0$:

$$\mathrm{FeCl_2 + Na_2S_2} \xrightarrow{E_a \sim 100^\circ\mathrm{C}}$$

$$(2-x)\ \mathrm{NaCl} + \mathrm{Na_{1-0.5x}FeS_{(2-x)}Cl_x} + x\ \mathrm{S} \tag{2.5}$$

$$\xrightarrow{\sim 175^\circ\mathrm{C}} \mathrm{FeS_2} + 2\,\mathrm{NaCl}. \tag{2.6}$$

The first step, Equation 2.5, has a low activation barrier; it can take place even at room temperature over the course of several months. Evidence in favor of such a mechanism with the incorporation of Cl in to $NaFeS_2$ is provided by the poor crystallinity of the observed $NaFeS_2$ phase, in addition to the distinct, larger lattice parameters of the monoclinic $NaFeS_2$ phase relative to the previously reported compound, as to accommodate the Cl^- ions which provide less electrostatic screening between metal cations.[93,94] Such a mechanism, derived by considering only the observed crystalline products, requires just partial oxidation of Fe^{2+} to Fe^{3+} during the early stages of $FeCl_2$ attack, as the iron valance is given by $Fe^{(3-x/2)+}$, where x is given in Equation 2.5. However, our observations and analysis do not preclude the formation of additional amorphous intermediates.

Furthermore, these redox activities can be rationalized as a reaction between the two intermediates, elemental sulfur and $NaFeS_2$. Comproportionation of the sulfur can occur when the S^{2-} anion reduces both the Fe^{3+} and S^0 to form pyrite:

$$3\,S^{2-} + 2\,Fe^{3+} + S^0 \longrightarrow 2\,FeS_2. \tag{2.7}$$

From Rietveld refinements of the HRSPXRD data, the nominal ratios of Fe^{3+}:S^{2-}:S^0 are 1:2:1 at 50 °C and 1.375:2.75:1 at 175°C. Therefore, discrepancies between the stoichiometry of the balanced chemical reaction and the observed values may be attributed to the poor crystallinity or sulfur deficiency of the $NaFeS_2$ intermediate.

The removal of $NaFeS_2$ is predicated on the formation of NaCl, which leads to the formation of FeS_2. The reactions with $M = Co^{2+}$ or Ni^{2+} also have suitable intermediates with the alkali-rich phases related to the structures of Na_2CoS_2 or $K_2Ni_3S_4$, the former of which was detected in the low temperature reactions of $CoCl_2$ and Na_2S_2. The resulting metal sulfides are all thermodynamically stable phases at ambient pressure, but not necessarily at ambient temperature, as shown by the formation of both zinc blende and wurtzite ZnS, along with NaCl and sulfur. This reveals the possibility of a synthetically-controlled route towards formation of non-ambient and ambient phases through metathesis.

2.5. Conclusion

Solid-state metathesis can be used to prepare pyrite metal disulfides at low temperature and without extensive self-heating or thermal runaway. While robust for a number of other transition metal disulfides, it appears that a major driving force for product formation is

not primarily the formation of the metathesis byproduct, NaCl. Instead, from a combination of HRSXRD and DSC, formation of the thermodynamically stable pyrite phases drives the overall reaction, while a low activation barrier for NaCl formation and favorable intermediate formation enables initiation of the reaction and without extensive self heating. Through careful analysis of the reaction intermediates, the metathesis involves significant atomic rearrangements in the formation of alkali-rich metal sulfides at low temperatures. This approach provides wide implications for the preparation of novel compounds or low-decomposition temperature materials that have substantial activation barriers that prevent their facile formation.

3. Circumventing Diffusion in Kinetically-Controlled Solid-State Metathesis Reactions[†]

3.1. Introduction

Solid-state chemical reactions are impeded by diffusion. Therefore, comparatively little can be done to gain kinetic control of solid-state chemical reactions in contrast to other fields of synthetic chemistry.[2,4,5] Instead, much reliance is put into reaching conditions in which solid-state diffusion is enhanced (i.e., higher temperatures) and the reactants are allowed to equilibrate and form the products that are most stable in that environment. Syntheses of nanomaterials are now approaching a "total-synthesis" framework to rationally design and tailor colloidal assemblies.[96]

Generally, the formation of metastable solid materials relies on chemical (de)intercalation or exchange of one type of ion from the lattice while the other ions remain immobilized in the lattice. This can be achieved in solution[17,19,97] or in the solid phase[29,30,32] to form metastable materials that are structurally analogous to the stable precursor but with a different composition. This inherently limits these processes to materials with mobile ions and a framework that can be oxidized or reduced and maintain its structure. Reactive alkali chalcogenide fluxes have the ability to enhance diffusion at moderate temperatures,[38] but the predictability of these reactions is in its infancy.[39,40] Solid state metathesis (*i.e.*, double ion exchange) reactions permit compositional predictability and allow for the ini-

[†]Substantial portions of this chapter have been reproduced with permission from A. J. Martinolich, J. A. Kurzman, and J. R. Neilson, *J. Am. Chem. Soc.* **2016**, *138*, 11031–11037, reference 95, © 2016 the American Chemical Society

tiation of solid-state reactions at low temperatures due to the formation of a thermodynamically stable byproduct, such as NaCl. These reactions initially garnered excitement for their ability to self-ignite to achieve short-lived temperatures in excess of 1000 °C, thus permitting the preparation of refractory[55–57,62,65,76,77] and ultra-hard materials.[58–60] More recently, our group has shown that with non-igniting reactions, solid-state metathesis can be performed in the limit of kinetic control,[63] and the reaction pathway can be chemically altered in order to isolate metastable phases.[98,99]

Here, we study solid state metathesis reactions, $M\text{Cl}_2 + \text{Na}_2\text{S}_2$ (M = Fe, Co, Ni), prepared in two different ways as to proceed in either a diffusion-limited or a nucleation-limited manner. The reaction $M\text{Cl}_2 + \text{Na}_2\text{S}_2$ (M = Fe, Co, Ni) prepared in strictly inert conditions reacts through a diffusion-limited pathway, forming several sub-stoichiometric $M_x\text{S}_y$ ($2x > y$) intermediates before the stoichiometric $M\text{S}_2$ product, as determined by *in situ* synchrotron powder X-ray diffraction. Correlation of these *in situ* diffraction data to differential scanning calorimetry (DSC) indicates that the NaCl formation is slow and only mildly exothermic in the strictly anhydrous reactions, in contrast to the standing hypothesis that these reactions are driven by the formation of the NaCl byproducts. However, if the reactants are first exposed to humid air, NaCl formation occurs immediately upon grinding at room temperature, thus displacing the counterions into an amorphous matrix resembling known M-S phases with low coordination numbers. Heating this mixture nucleates the crystalline $M\text{S}_2$ phase directly without substoichiometric intermediates. In these partially hydrated reactions, the DSC does not show significant enthalpic signatures upon crystallization of the product. Together, our results provide an approach to overcome

solid-state diffusion in a bulk solid-state reaction and provide insight to the mechanistic control of solid-state reactions.

3.2. Materials and Methods

Note on author contributions: This chapter was published in *Journal of the American Society*, **2016**, volume 138, page 11031, by Andrew J. Martinolich, Joshua A. Kurzman, and James R. Neilson. AJM performed in-house experiments, executed *in situ* synchrotron experiments, analyzed the data, and wrote the initial draft of the manuscript. JAK executed *in situ* synchrotron experiments. JRN analyzed data and supervised the project. All authors contributed to the editing and finalization of the manuscript.

All reactants were prepared and stored an argon-filled glove box with H_2O and O_2 levels ≤ 0.1 ppm. All transition metal chlorides were used as purchased, with purity $>98\%$. Na_2S_2 was synthesized through the indirect reaction of Na + S; in a sealed 14 mm i.d. vitreous silica tube, an alumina crucible containing purified elemental sulfur was placed on top of an alumina crucible containing $\approx$ 1.02 equivalents of elemental sodium. The excess was to account for observable oxidation on the surface of the sodium metal. The reactants were then heated at 200 °C for 24 hours, at which point all material could be found in the originally-sodium containing crucible. The heterogeneous product was then collected in the glove box, ground, pelleted, and resealed, and heated at 300 °C for 24 hours to form Na_2S_2, at which point a yellow powder was collected in the glove box. To confirm purity of the Na_2S_2, air-free powder diffraction data were collected in a sealed glass capillary using a Bruker APEX II single crystal diffractometer (MoKα radiation, λ = 0.7107 Å).

Laboratory PXRD data were collected with Bruker D8 Discover X-ray Diffractometer using a CuKα radiation and a Lynxeye XE-T position sensitive detector. Air-sensitive samples were prepared on a zero-diffraction off-axis Si wafer in an argon glovebox before being sealed off with Kapton® tape.

The reaction mixtures of MCl$_2$ and Na$_2$S$_2$ were combined in 1:1 stoichiometric ratios and ground homogeneously. They were then evacuated and sealed in extruded silica capillaries (o.d. = 0.7 mm). For air-exposed reactions, the reaction mixtures were ground homogeneously in an Ar-filled glove box, then removed to a fume hood in ambient atmosphere. The reaction mixtures all begin to darken in appearance within seconds and are completely black after ca. 60 seconds of grinding. Exact humidity levels were not controlled, but were generally $\leq$ 50% as monitored by an ambient humidity sensor. The reactant mixtures do not deliquesce. The reaction mixtures were then evacuated to ¡10 mtorr and sealed in extruded silica capillaries. *In situ* synchrotron X-ray diffraction data was collected using beamline 17-BM-B (λ = 0.75009 Å) at the Advanced Photon Source at Argonne National Laboratory. The samples were heated at 3 °C min^{-1} from room temperature to 400 °C using a resistive heater as previously described.[100] Diffraction data were continuously collected using a 2048$\times$2048 pixel Perkin-Elmer 2D plate detector in 30 second increments, each pattern consisting of three 10 s subframes, while the sample was continuously rotated by 5° along its long axis. The 2D diffraction patterns were then radially integrated using GSAS-II.[101] A LaB$_6$ standard (NIST 660b) was used to calibrate the sample-to-detector distance, which was nominally 300 mm. *Ex situ* total scattering data were collected on beamline 11-ID-B (λ = 0.2114 Å) at the Advanced Photon Source at Argonne National Laboratory. The *in situ* total scattering data were collected on beamline

11-ID-C (λ = 0.1115 Å) at 10 °C intervals and the data was then radially integrated using Fit2D.[102] The pair distribution functions *G(r)* were then extracted using PDFgetX3[103] and fit using PDFGUI.[104] Rietveld analyses were performed using EXPGUI/GSAS.[79,80] Sequential Rietveld refinements were executed in small sections (determined by visual inspection) and maximum damping was applied to prevent unphysical outcomes in the fits.

Differential scanning calorimetry data were collected on a TA Instruments DSC on homogeneously ground reaction mixtures (approx. 10 mg) hermetically sealed in aluminum cans. The temperature ramp was 3 °C min^{-1} to replicate the reaction collected *in situ*. The enthalpy of each reaction was approximated by integrating the DSC curves after subtracting a linear baseline. Hess's law calculations were performed using tabulated values for the standard formation energy of the reactants and products.[105]

3.3. Results

The reactions $M\text{Cl}_2 + \text{Na}_2\text{S}_2 \longrightarrow 2\,\text{NaCl} + M\text{S}_2$ (M = Fe, Co, or Ni) have been previously reported, and the reactions typically require heating the reactants to $T \geq 250$ °C for the reaction to proceed when performed in anhydrous conditions.[63,65] In this contribution, these reactions are described in detail from experiments involving *in situ* synchrotron X-ray diffraction (SXRD, under vacuum) and differential scanning calorimetry (DSC, under argon) to study their reaction progress and energetic profiles as a function of temperature from 25 °C $\leq T \leq$ 400 °C. The reactions were performed in two different ways and will be discussed in order: (a) the reactants were initially ground in an Ar-filled glove box, then

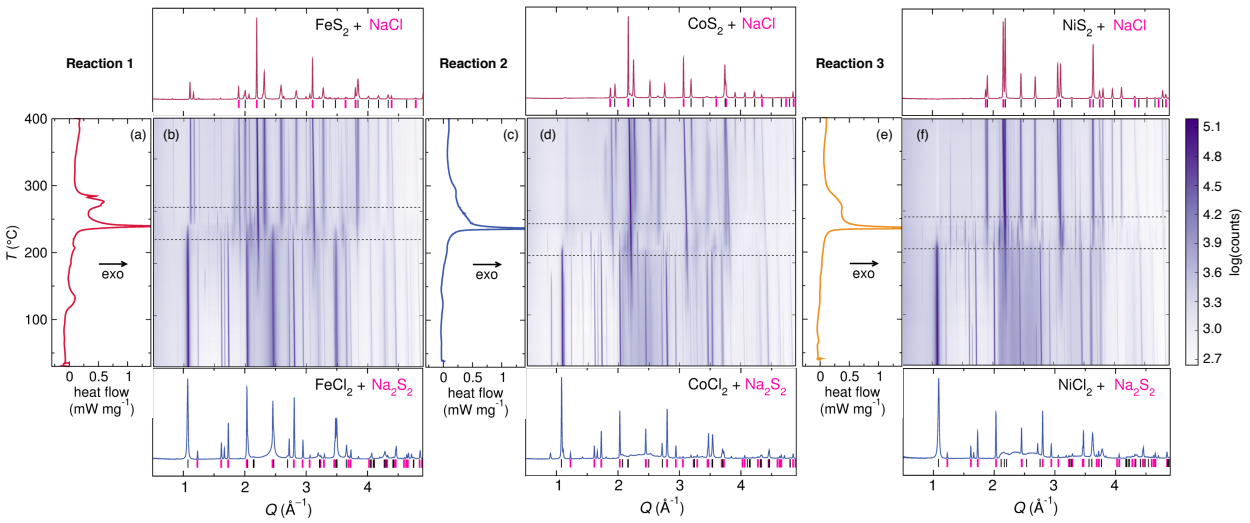

Figure 3.1: *In situ* DSC [(a), (c), (e)] and SXRD [(b), (d), (f)] of the strictly anhydrous solid-state metathesis reactions of $M\mathrm{Cl}_2 + \mathrm{Na}_2\mathrm{S}_2 \longrightarrow M\mathrm{S}_2 + 2\,\mathrm{NaCl}$, where M = Fe, Co, and Ni, respectively. Each reaction progresses through three major zones: reactants at low temperatures (bottom panels), a highly reactive zone with transient intermediates with the major exotherm in the DSC (between dashed lines), and the expected products at high temperatures (top panels). Color plots are shown on a logarithmic scale to accentuate minor phase contributions during the reactive zone.

heated in vacuum (SXRD) or argon (DSC); (b) the reactants were initially ground in air, then heated in an inert atmosphere.

The anhydrous reactions $M\mathrm{Cl}_2 + \mathrm{Na}_2\mathrm{S}_2 \longrightarrow M\mathrm{S}_2 + 2\,\mathrm{NaCl}$ (M = Fe, **1**; Co, **2**; Ni, **3**), mixed under argon and prepared for analysis without exposure to air were studied upon heating from 25 °C $\leq T \leq$ 400 °C using DSC (Figure 3.1a, c, e) and SXRD (Figure 3.1b, d, f). Each reaction occurs in a similar fashion, progressing from reactants to products with the exothermic formation of multiple crystalline intermediates. A summary of the observed crystalline intermediates is provided in Table 3.1.

As the reactants are heated, the first phase to crystallize in appreciable amounts is NaCl. This occurs at relatively low temperatures ($T \approx 100$ °C) in **1**–**3**. In all cases, various sodium sulfide intermediates also crystallize concomitant with NaCl formation. A small exotherm is also observed in **1** at $T \approx 130$ °C that may be attributed to the formation of NaCl; an obvious exotherm is not visible in **2** or **3** with the initial formation of NaCl. The small

Table 3.1: Summary of product formation temperatures, intermediates, and energetics in Reaction **1–6**.

Reaction	Reactive zone T	$T_f(MS_2)$	T_f(NaCl)	Crystalline Intermediates	Integrated exotherm (kJ mol^{-1})	Theoretical reaction enthalpy (kJ mol^{-1})
1	222–257 °C	222 °C	115 °C	Na_2S_4, Na_2S_5, Fe_7S_8, Fe_3S_4, $Na_3Fe_2S_4$, marcasite FeS_2	–141	–261
2	192–230 °C	260 °C	100 °C	Na_2S_4, Na_2S_5, Co_9S_8, CoS, Co_3S_4	–133	–263
3	196–242 °C	228 °C	90 °C	Na_2S_4, Ni_3S_2, ht-NiS, rt-NiS	–137	–249
4	n/a	155 °C	n/a	none	–15	–261
5	n/a	240 °C	n/a	none	–13	–263
6	n/a	155 °C	n/a	none	–36	–249

exotherm may also be attributed to the slow, gradual formation of NaCl which spreads out the release of heat over a large range of temperatures. Along with NaCl formation is the appearance of several sodium-poor Na-S phases (e.g., Na_2S_4 and Na_2S_5). The appearance sulfur-poor binary M-S phases (e.g., Fe_7S_8, Fe_3S_4, Co_9S_8, CoS, Co_3S_4, Ni_3S_2, and NiS), and one ternary $Na_3Fe_2S_4$ phase occurs approximately at the temperature of the major exotherm. Several of these intermediate phases are expected to be metastable under the experimental conditions according to their bulk equilibrium phase diagrams,[10–12] such as spinel Fe_3S_4, marcasite FeS_2, hexagonal CoS, and the high-temperature polymorph of NiS. The end of the reactive zone concludes with formation of the expected MS_2 phase. Integration of the DSC curves (correcting for a linear sloping baseline offset) yields the integrated reaction enthalpy, which is lower than the theoretical reaction enthalpy determined from Hess's Law (Table 3.1), in contrast to the self-igniting metathesis reactions.[55,56] Comparison of the temperature of the major exotherm detected via DSC to the relative phase fractions of the reactants and products indicates that *the sharp exotherm is not due to the formation of NaCl*, but instead reactivity of the metal sulfide phases and MS_2 product formation (Figure 3.2).

The reactions follow a completely different pathway if the reactants are exposed to air before preparation for DSC and *in situ* SXRD (M = Fe, Reaction **4**; M = Co, Reaction **5**; M = Ni, Reaction **6**; Figure 3.3a-f). In all cases, crystalline NaCl forms upon grinding the reactants in air at room temperature. The yield of NaCl immediately after grinding is approximately 50% in all cases, determined via PXRD with a known amount of internal Si standard. There is a significant amount of diffuse scattering visible in the diffraction data after subtraction of the silica capillary background. There is also a small amount of $NaFeS_2$ and elemental sulfur detected at room temperature in **4**, similar to our previous *ex situ* study.[63]

As the reaction mixture is heated, the expected MS_2 product crystallizes directly and the diffuse background decreases. In contrast to the air-free experiments, there is no apparent reactive zone, no progression of crystalline M–S binary intermediates, and no polymorphism in the products. The distinct DSC results show subtle endothermic processes

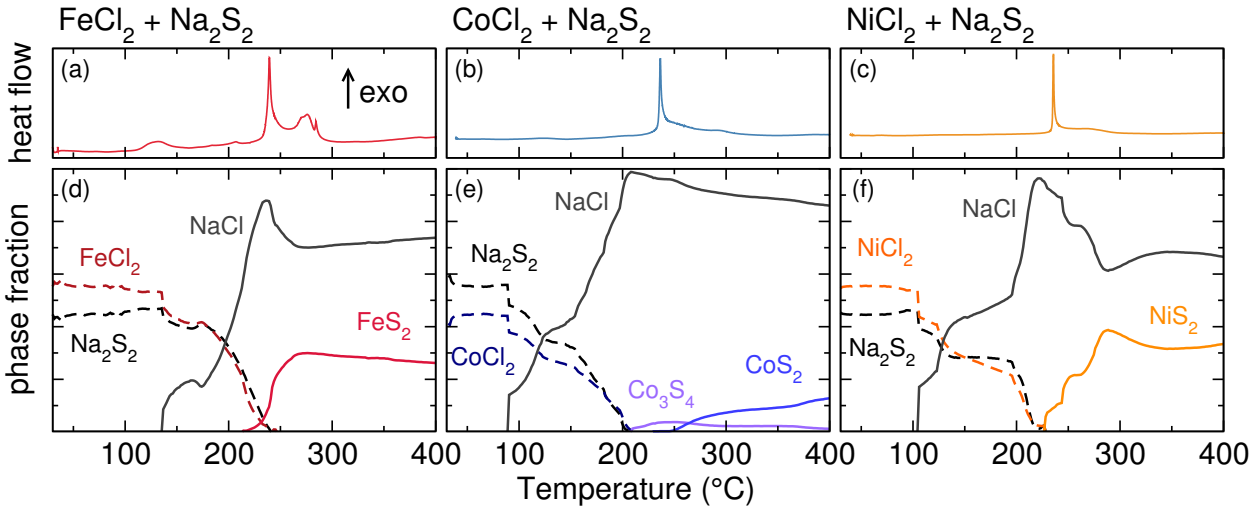

Figure 3.2: DSC (a, b, c) compared to relative crystalline phase fractions (d, e, f) of the reactants and the majority products as a function of temperature extracted from sequential Rietveld refinements indicating the general reaction progression of the air-free solid state metathesis reactions (omitting other crystalline intermediates with i 10 mol % phase fractions). The phase fraction of NaCl peaks before the major exotherm, indicating that the exotherm is released due to the crystallization and progression of the MS_x phases.

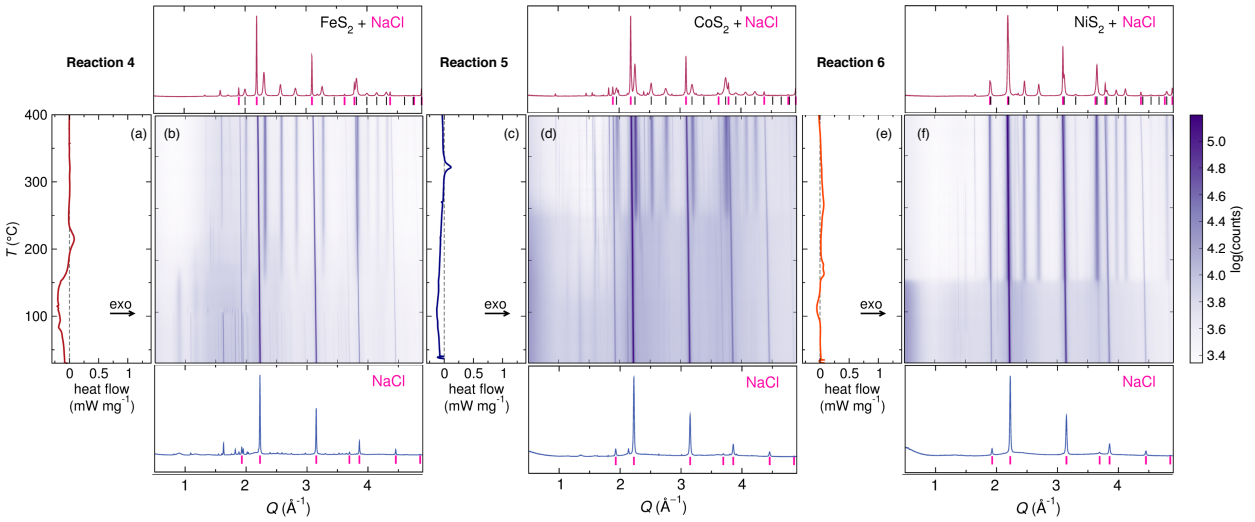

Figure 3.3: *In situ* DSC [(a), (c), (e)] and SXRD [(b), (d), (f)] of the air-exposed solid state metathesis reactions of $M\mathrm{Cl}_2 + \mathrm{Na}_2\mathrm{S}_2 \longrightarrow M\mathrm{S}_2 + 2\,\mathrm{NaCl}$, M = Fe (Reaction **4**), Co (Reaction **5**), and Ni (Reaction **6**), respectively. In the air exposed reactions, the reaction pathway is extensively altered compared to the air-free reactions, with NaCl present throughout and no apparent crystalline intermediates, the products instead crystallizing out of the reaction mixtures. There are significant diffuse features in the background as well, indicating the presence of an amorphous phase. This is especially apparent in **5** and **6**. The diffraction patterns of the as-prepared reactants and the products at 400 °C are shown below and above each color plot, respectively.

at low temperatures with a small exotherm observed upon $M\mathrm{S}_2$ crystallization. Integration of the exotherms indicate that these processes are an order of magnitude less exothermic than the air-free reactions. At 400 °C, the ratio of NaCl to $M\mathrm{S}_2$ is approximately 2:1 in all cases as anticipated from the balanced chemical reaction. These results, along with those from Reactions **1**–**3**, are summarized in Table 3.1.

To probe the nature of the diffuse scattering in the air-exposed reactions, the structure of the residual metal sulfide was investigated using pair distribution function (PDF) analysis of total X-ray scattering data of the as-ground mixture (Figure 3.4) and as a function of temperature for Reaction **4** (Figure 3.5). In the as ground samples, the majority of the correlations visible in the PDF correspond to highly crystalline NaCl, as quantitatively modeled. Therefore, after constraining the NaCl phase to fit the PDF at longer r ($r > 10$ Å), the difference between the NaCl fit and the experimental PDF reveals the short-range

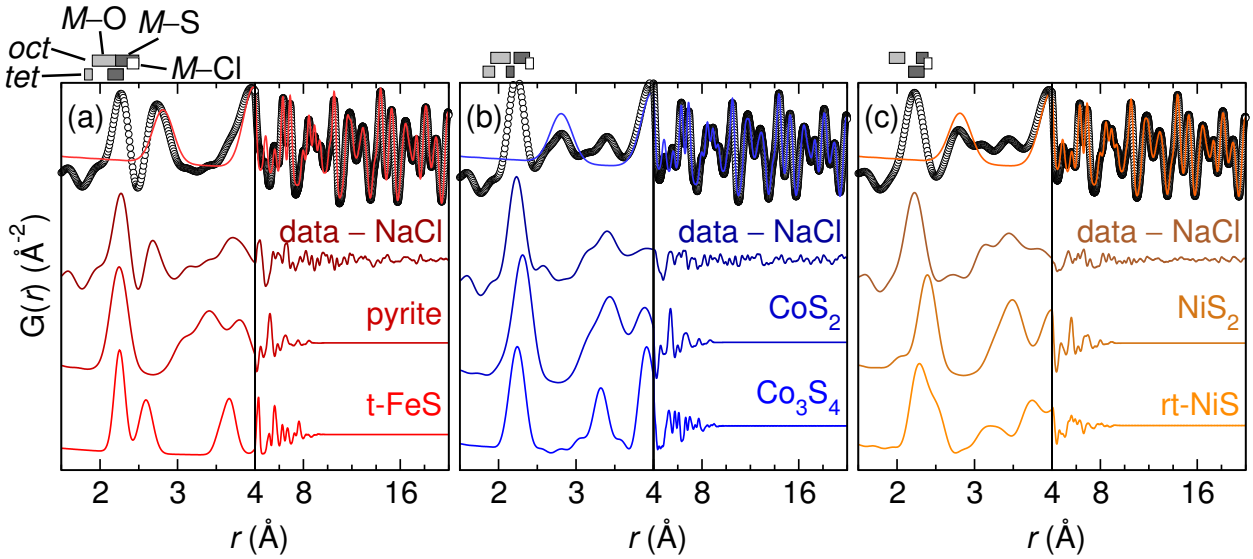

Figure 3.4: Pair distribution function (PDF) analyses of the as-prepared air-exposed reaction mixtures. Fits to NaCl were applied and the difference was then compared to calculated PDFs of a number of transition metal sulfides, shown below. The calculated PDFs are truncated using spherical diameter particle cutoff of 10 Å. Qualitative comparison to the difference curves indicate that all reaction mixtures have some structural similarities to the MS_2 product that forms.

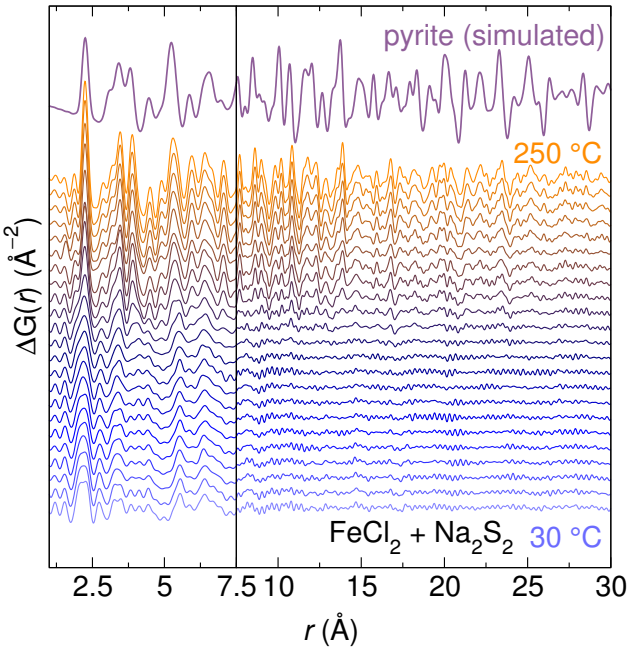

Figure 3.5: *In situ* differential PDF analysis of **Reaction 4** ($FeCl_2$+Na_2S_2 with the pairwise correlations arising from NaCl subtracted. The differential PDF at lower temperatures reveals only short range correlations; longer range correlations consistent with crystallization gradually grow in starting around T $\approx$ 160 °C, in agreement with *in situ* PXRD data. The high temperature differential PDF is identical to that of pyrite FeS_2. The offset data are taken in 10 °C increments.

order of an amorphous metal sulfide phase with a low coordination number. Comparison of this difference curve to calculated PDFs of various spherically-truncated crystalline metal sulfides indicates that the phases have short-range order that is structurally similar, but not the same, to intermediate MS phases or the resultant MS_2 products that form. The nearest-neighbor pair correlation peak appears at a distance consistent with known M–S phases, rather than M–O or M–Cl bond lengths as indicated in Figure 3.4. *In situ* PDF analysis of Reaction **4** (Figure 3.5) also indicates that upon air exposure, a short-range ordered intermediate forms that resembles pyrite FeS_2 is observed at low *r*, which then crystallizes at $T \approx 160$ °C, in agreement with the *in situ* SPXRD.

A number of control reactions were executed to support that it is indeed the exposure to atmospheric H_2O that promotes the amorphous intermediate formation. If the reactants are instead sealed with ca. $1/3$ atm of O_2, no color change is observed after 1 hour at room temperature. Alternatively, a pellet of the reactants in ambient air turns black within seconds. If the reaction mixtures sealed with O_2 are then heated to 100 °C for one hour, PXRD analysis of the mixtures indicate that only the reactants MCl_2 and Na_2S_2 are still present, which is identical to the air-free reactions.

3.4. Discussion

Taken together, these results illustrate that the presented kinetically controlled solid-state metathesis reactions have been executed in a manner that circumvents diffusion to produce crystalline material in the bulk. Thin-film metallurgical junctions have been shown to exhibit kinetically-controlled reactions that are not diffusion limited.[41,42] As the

film thickness increases, one tends to observe a range of intermediate compounds due to the limited diffusion of reactants through the product.[106] By limiting the thickness of the thin films, a distinct solid-state reaction mechanism in which the reactants completely interdiffuse before nucleation of a crystalline phase is observed, as initially shown with iron silicides[41] among other examples.[43] When crystalline, kinetic intermediates are observed, the first phase to form is not necessarily the most thermodynamically stable,[107] but rather, it has been proposed that the the first phase to form is that which allows the largest change in free energy in the shortest period of time (*i.e.*, greatest $\Delta G/\Delta t$).[108,109] This rationalizes the observation of metastable Fe_5Si_3 (a high-temperature phase) in binary Fe-Si couples at low temperature, as well as the formation of amorphous phases.[107] However, it has not been clear how to achieve kinetic control in the synthesis of materials without an intentionally-reduced diffusion length.

The metathesis reactions prepared in an inert argon environment are diffusion limited, akin to "thick" film diffusion couple reactions. This conclusion is based upon the observation of a range of sulfur poor intermediates in all cases, which are both stable (e.g., Fe_7S_8, Co_3S_4, rt-NiS) and metastable (e.g., Fe_3S_4, CoS, ht-NiS) with respect to the reaction conditions at the time of their observation. This indicates that the reaction is essentially progressing as metal and sulfide ions crystallizing as they inter diffuse after NaCl has formed, forming a range of MS_x intermediates before reaching the stoichiometric MS_2 product, depending on the degree of diffusion that has occurred at a given temperature. This sampling of the phase diagram agrees with fundamental studies of diffusion couples in solids and strongly indicates that the reaction is indeed diffusion limited.[107,108] It is possible that amorphous MS_x intermediates may also form, but their presence is not immediately evi-

dent from the *in situ* diffraction experiments. Here, the onset of reactivity, indicated by the formation temperature of NaCl (Figure 3.2), correlates with the enthalpy of formation of the metal chloride precursor. The enthalpy of formation of the metal sulfide products show no such correlation. Our observations are also consistent with the contrasting self-igniting metathesis reactions, in which one observes an initial "induction period".[55–58,62,65] There, the initial formation of NaCl at lower temperatures causes displacement of the metal and sulfur counterions. The diffusion-limited process then initiates the exothermic reaction that self-heats the reaction mixture enough to melt the alkali halide, thus allowing for rapid diffusion of the reagents.

If the solid-state metathesis reactions are first ground in ambient atmosphere before sealing under vacuum and annealing (**Reactions 4 – 6**), NaCl forms and a color change to black occurs in all cases. Annealing these reaction mixtures yields direct formation of the $M\mathrm{S}_2$ product at lower temperatures than the air free reactions, and with much less heat released (see Table 3.1). In contrast to the air-free, diffusion-limited reactions, these partially hydrated reactions show no crystalline intermediates before $M\mathrm{S}_2$ product formation. Grinding in air clearly alters the energetic and structural pathways to product formation, yielding an amorphous intermediate that releases little energy upon crystallization. Additionally, we have previously shown that this air exposure does not negatively affect the properties of the resultant material, exemplified by the superconducting transition of metastable cubic CuSe_2.[98]

The formation of the amorphous precursor is a significant alteration to the reaction mechanism. This, in conjunction with the observation of direct $M\mathrm{S}_2$ crystallization, suggests that the air-exposed reactions are limited by nucleation of the product phase rather

than diffusion of the reactants. Regardless of the transition metal, the nearest neighbor in the as-ground PDF corresponds to *M*–S bond lengths for a low coordination number, rather than metal–oxygen or metal–halogen bonds (Figure 3.4). Here, we speculate that the formation of an amorphous intermediate that has the lowest stable coordination geometry of the transition metal with sulfur provides the maximum $\Delta G/\Delta t$ in a kinetically-controlled reaction. In all of these cases we observe an intermediate amorphous phase that resembles the most dense, and lowest coordination number known for these transition metal sulfides (tet-FeS, Co_3S_4, NiS).

The formation of the *M*–S bonds upon grinding the reactants in air aids in explaining why the annealing is so much less exothermic than the air-free reactions. Rather than breaking and making bonds, the intermediate undergoes subtle rearrangements and crystallization, akin to the nucleation of metastable $FeSb_3$ from modulated elemental reactants in a thin-film geometry.[44] Analysis of the *in situ* diffraction profile at the approximate onset of MS_2 crystallization indicates that the MS_2 phases form initially as small nano-sized crystallites (ca. 100s of angstroms) that grow upon annealing, which will have a distinct thermodynamic signature spread out over a wide range of temperatures, as opposed to a sharp crystallization transition.

The key to altering the reaction pathway of these reactions from diffusion-limited to nucleation-limited is grinding the reactants in air. We previously showed that the air exposure of a metathesis reaction can lead to the formation of a metastable cubic polymorph of $CuSe_2$.[98] We later confirmed a trace amount of a Lewis base, such as triphenylphosphine, mirrors this chemical activity by facilitating atom-transfer reactions during the double exchange reaction, as noted by the observation of stable adducts (e.g.,

Se:PPh_3, $[Cu(PPh_3)_n]^+$).[99] In thin-film diffusion couples (i.e., modulated elemental reactions[41–44]), solid-state interdiffusion is achieved at lower temperature by decreasing the physical length scale over which the reagents must diffuse to form the new material. As summarized in Figure 3.6, we show that a chemical additive, such as trace H_2O (g), can accomplish the same effect in a solid-state metathesis reaction to circumvent solid-state diffusion.

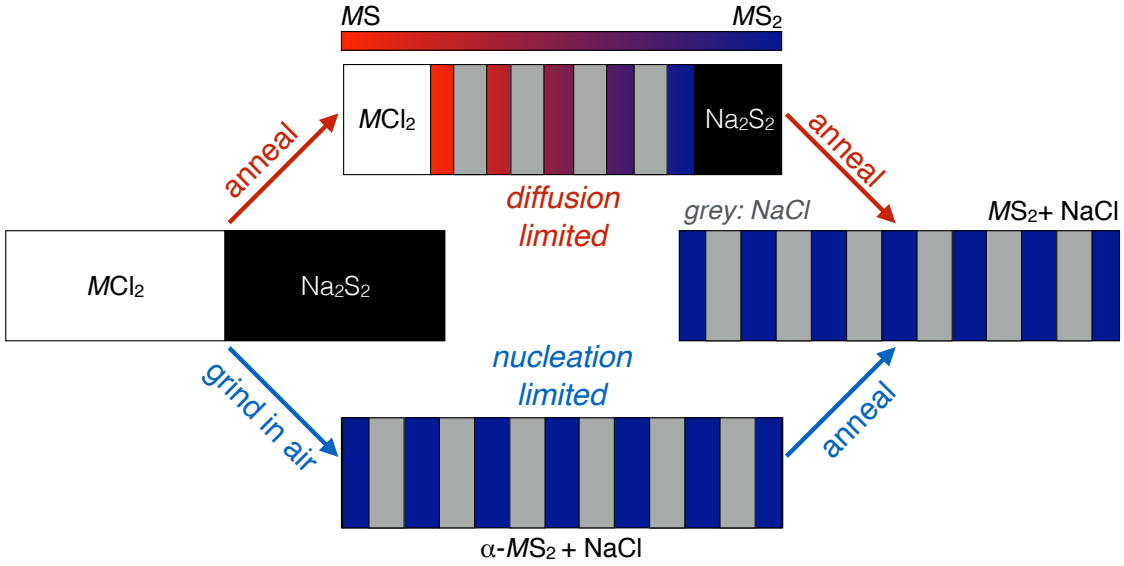

Figure 3.6: Scheme illustrating the different observed reaction pathways of the metathesis reactions. Preparing the the reactants in a strictly air-free and anhydrous manner leads to a diffusion-limited reaction which in turn allows the formation of a range of MS_x phases ($x \leq 2$). Grinding the reactants in air allows NaCl formation along with an amorphous (α) material of the nominal composition MS_2. Annealing leads to direct nucleation of the crystalline MS_2 phase.

3.5. Conclusions

The solid-state metathesis reactions of $MCl_2 + Na_2S_2$ show the structural signatures from the progression of reactants to intermediates to products, determined from *in situ* structural and thermochemical analysis of the reactions. However, the formation of NaCl in anhydrous metathesis reactions proceeds slowly and without appreciable energy release.

The gradual formation of NaCl allows displacement of the *M* and S counterions to form intermediates that are substoichiometric with respect to the final products, such as metal-sulfide binaries, a range of Na_2S_x phases, and some ternary phases. If the reactants are exposed to humid air, H_2O can facilitate atom transfer before heating, thus crystalline NaCl forms directly along with an amorphous *M*–S phase with a low coordination number. This indicates that the reaction is no longer limited by solid-state diffusion (i.e., the NaCl and M–S bonds have already formed). Instead, product formation is limited by nucleation of the crystalline MS_2 phase. The results provide the pathway to direct synthetic solid state chemistry towards a paradigm of materials by design. From these results, one can design a wide range of reactions to target discovery of new metastable polymorphs or stable compounds that have not been kinetically accessible using traditional solid-state chemistry.

4. Polymorph Selectivity of Superconducting $CuSe_2$ Through Kinetic Control of Solid-State Metathesis[†]

4.1. Introduction

In preparative solid-state chemistry, different polymorphs are often selected by changing extrinsic parameters to favor distinct atomistic configurations with the lowest thermodynamic free energy. While many extrinsic factors influence polymorph thermodynamic stability, such as pressure (graphite *vs*. diamond), temperature (ZnS[9]), and specific surface area (TiO_2[16]), such polymorphs can be kinetically stable (*i.e.*, metastable) at ambient conditions. However, kinetic control, in this case, the ability to prevent a system from reaching the thermodynamic equilibrium product, can be exercised through alteration of the pathway to product formation. This is largely unexplored in the formation of bulk, solid-state materials.

Transition metal chalcogenides of the pyrite structural family give rise to myriad functional electronic properties, including superconductivity (*cf.*, CuS_2, $CuSe_2$, $IrSe_2$);[15,110] however, many of these crystals can be produced only at high pressure. $CuSe_2$ exists in two known polymorphs: marcasite $CuSe_2$ and the high-pressure phase, pyrite $CuSe_2$, which is metastable under ambient conditions (Figure 4.1).[111] The superconducting transition temperature is strongly influenced by the structure: T_c = 2.4 K and 0.7 K for pyrite and marcasite, respectively.[15,112]

[†]Substantial portions of this chapter have been reproduced with permission from A. J. Martinolich, J. A. Kurzman, and J. R. Neilson, *J. Am. Chem. Soc.* **2015**, *137*, 3827–3833, reference 98 © 2015 the American Chemical Society

The preparation of metastable materials (without the use of other extrinsic thermodynamic parameters, such as pressure) often involves *chimie douce* reactions,[19,113–116] where a difference in relative mobilities of ions in the lattice permits topochemical transformations into metastable polymorphs, as first exemplified by the oxidative deintercalation of $LiVS_2$ to yield a new polymorph of VS_2.[17] However, examples in which metastable polymorphs can be produced through kinetic control without such topochemical relations are not widely understood. High-temperature solvents, such as the reactive alkali chalcogenide fluxes, can be used to produce compounds that are metastable under ambient conditions;[117] however, an understanding of the kinetic pathways or thermodynamic conditions that control their formation is limited.[40]

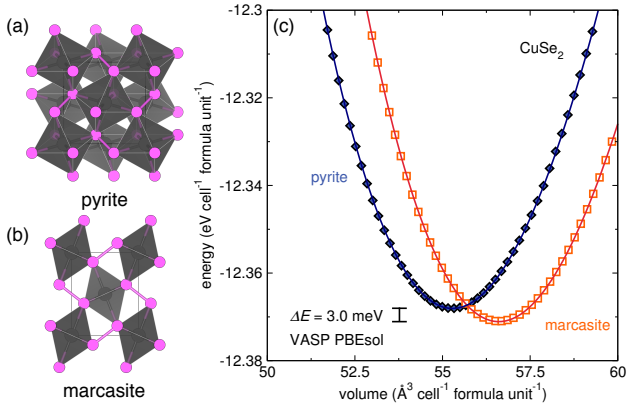

Figure 4.1: Atomistic representations of (a) pyrite and (b) marcasite polymorphs of $CuSe_2$. (c) The total energy from DFT calculations (VASP, PBEsol) illustrate that marcasite is more stable by a small margin (~ 3.0 meV); approximately 1.2 GPa of external pressure stabilizes pyrite $CuSe_2$. Symbols result from individual DFT calculations; lines are fits to the Birch-Murnaghan equation-of-state.[118]

In this work, kinetic control over the formation of distinct polymorphs of the superconductor $CuSe_2$ is demonstrated by altering the pathway through which a solid-state metathesis reaction occurs. Preparation of the pyrite modification of $CuSe_2$ (p-$CuSe_2$) in 100% yield typically requires application of pressure in excess of 1 GPa,[15] in agreement with the reported equilibrium phase diagram[119] and density functional theory (DFT) calcu-

lations (Figure 4.1c). In the metathesis reaction (*i.e.,* double-displacement) between $CuCl_2$ and Na_2Se_2, marcasite $CuSe_2$ and 2 NaCl are produced when performed under strictly anhydrous conditions. However, partial solvation of the reaction mixture by exposure to humid air before heating (and not exposure to dry O_2) enables the formation of bulk pyrite $CuSe_2$. By following the air-exposed reaction *in situ*, we observe that the solid-state metathesis occurs through endothermic and displacive transitions involving crystalline intermediates rather than through an exothermic and reconstructive transition. Partial solvation of the reaction mixture greatly reduces the initial activation barrier and allows the reaction to proceed under *kinetic* control, where the rate-limiting step appears to be diffusion of elemental selenium into the reaction intermediate CuSe, which forms upon air exposure.

4.2. Materials and Methods

Note on author contributions: This chapter was published in *Journal of the American Society*, **2015**, volume 137, page 3827, by Andrew J. Martinolich, Joshua A. Kurzman, and James R. Neilson. AJM performed in-house experiments, executed *in situ* synchrotron experiments, analyzed the data, and wrote the initial draft of the manuscript. JAK executed *in situ* synchrotron experiments. JRN analyzed data and supervised the project. All authors contributed to the editing and finalization of the manuscript.

Na_2Se_2 was synthesized from the elements with a 2% excess of Na to account for surface oxidation in a sealed tube at 400 °C. The reactants were separately contained in different alumina crucibles to prevent a violent thermite reaction; after 12 hours of reaction all

product was found in the crucible originally containing the sodium. Purity of the Na_2Se_2 was confirmed through PXRD using a Bruker APEX II single crystal diffractometer (MoKα radiation, $\lambda = 0.7107$ Å) with powder in a sealed quartz capillary; the two-dimensional data were radially integrated for analysis. Otherwise, laboratory PXRD measurements were collected on a Scintag A2 diffractometer with CuK_α radiation.

To isolate pure pyrite $CuSe_2$, stoichiometric amounts of Na_2Se_2 and anhydrous $CuCl_2$ were weighed in an argon-filled glove box and ground to an homogenous powder. Upon removal from the glove box, the powder was further ground until a color change from deep brown to black was evident. The black powder was then pelleted and sealed in an evacuated fused silica ampoule and heated to 100 °C at a rate of 1 °C min^{-1} and held constant for 24 h. Control reactions were held at 100 °C for 72 hours and 1008 hours. The products were then washed several times with anhydrous methanol to remove the NaCl and dried under vacuum.

To form marcasite $CuSe_2$, stoichiometric amounts of Na_2Se_2 and anhydrous $CuCl_2$ were weighed in an argon-filled glove box and ground to a homogenous powder and pelleted. The pellet was then sealed in an evacuated quartz ampoule without exposure to the atmosphere and heated to 300 °C at a rate of 1 °C min^{-1} and held constant for 24 h.

CuSe was formed from the elements at 300 °C in a sealed tube for 24 hours. The product was then ground together with selenium shot until homogeneous, pelleted, and reacted in an evacuated quartz ampoule to form $CuSe_2$ at 100 °C for the specified times. Additionally, marcasite $CuSe_2$ (formed by metathesis) was ground homogeneously with two equivalents of NaCl, pelleted, sealed in a quartz ampoule under vacuum, and reacted at 100 °C for the specified times.

In situ X-ray diffraction experiments were executed using beamline 17-BM-B ($\lambda = 0.75009$ Å) at the Advanced Photon Source at Argonne National Laboratory. The reaction mixture was ground in air and packed into a 0.20 mm diameter capillary and sealed under vacuum. To heat the reaction mixture, a resistive heater and thermocouple were used as previously described.[100] The reaction mixture was heated at a constant rate of 3 °C min^{-1} from room temperature to 370 °C.

In situ pair distribution function analysis experiments were executed using beamline 11-ID-C ($\lambda = 0.11165$ Å) at the Advanced Photon Source at Argonne National Laboratory. The reaction mixture was ground in air and packed into a 0.70 mm diameter extruded silica capillary and sealed under vacuum. To heat the reaction mixture, a resistive heater and thermocouple were used as previously described.[100] Diffraction measurements were continuously collected using a 2048$\times$2048 pixel Perkin-Elmer 2D plate detector in 30-second increments, each pattern consisting of three 10-second subframes, while the sample was continuously rotated by five degrees along its long axis. For PDF experiments, the reaction mixture was heated to the specified temperature at 5 °C min^{-1} and allowed to dwell for five minutes at each temperature before data were collected. The 2D diffraction patterns were then radially integrated using GSAS-II (diffraction) or Fit2D (PDF).[102,79,80,101] The pair distribution functions, $G(r)$, were extracted using PDFgetX3[103] and fit using PDFGUI.[104]

Rietveld refinements were executed sequentially in the EXPGUI frontend to GSAS. The full set of diffraction patterns were split into six separate sets based on visual inspection to determine at which temperatures require addition or deletion of phases in the refinement (temperature ranges 28–92 °C, 92–123 °C, 123–163 °C, 163–240 °C, 240–247 °C, 247–283 °C, and 283–367 °C). The lowest temperature in each set was refined by hand and

served as a starting point for each sequential refinement. Maximum dampening was applied to all parameters to maintain reasonable values. The fits were then compared within each set, and to the adjacent sets, to confirm adequate fits and continuity across the entire set of diffraction patterns. Phase fractions were extracted from weight percent values and converted to molar percents.

Magnetic measurments were performed using a Quantum Designs Inc. MPMS. Heat capacity measurements were performed using a Quantum Designs Inc. Dynacool PPMS. DSC measurements were performed using a TA instruments DSC on samples hermetically sealed in an argon environment. The heating rate for the DSC measurements was 1 °C min^{-1}.

Density functional theory (DFT) calculations with projector-augmented-wave (PAW) potentials with Cu $3p$ semi-core states treated as valence states[120] were implemented using the *Vienna Ab Initio Simulation Package* (VASP)[121] within the generalized gradient approximation to account for exchange and correlation effects (PBEsol[122]). Ferromagnetic, antiferromagnetic, and non-magnetic configurations were tested; the non-magnetic state was lowest in energy. The plane-wave energy cutoff was 800 eV for all calculations, which were performed on a $10 \times 10 \times 10$ and $12 \times 10 \times 14$ k-mesh for pyrite and marcasite, respectively. For ionic relaxations, forces were converged to within 0.01 eV Å^{-1}; within each self-consistency cycle, the total energy was converged below 10^{-6} eV. Convergence tests were performed with respect to the Γ-centered k-mesh and band cutoff.

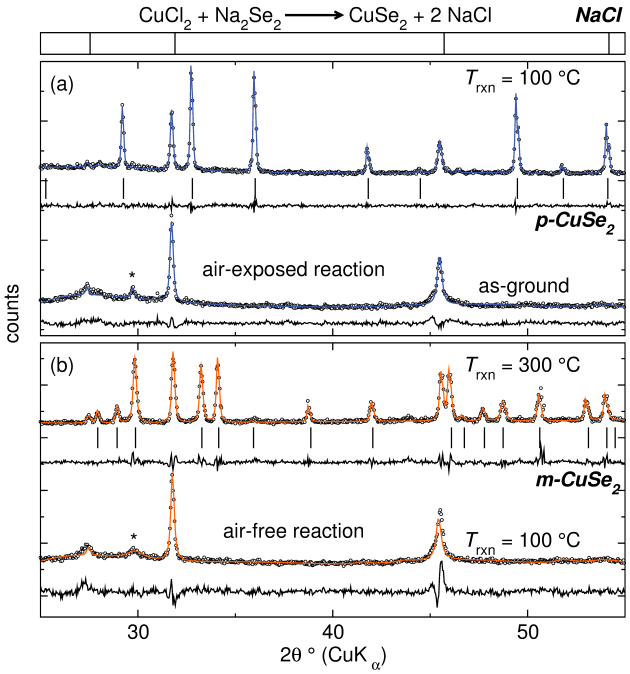

Figure 4.2: Powder x-ray diffraction (PXRD; black symbols) comparison of metathesis products from reactions that have been (a) air-exposed and (b) strictly air-free, along with their Rietveld analyses (colored lines) and difference curves (black lines). Asterisks indicate reflections from crystalline Se. The expected reflections of NaCl are shown above the refinements.

4.3. Results

From our DFT calculations, shown in Figure 4.1c, we confirm that marcasite is 3.0 meV lower in energy in the ground state (electronically for $T = 0$ K). Furthermore, the calculated energies were fit to a Birch-Murnaghan equation-of-state to extract the ground-state volume and bulk modulus.[118] For marcasite $CuSe_2$, the bulk modulus is $B = 78.9$ GPa and ground-state volume is $V_o = 56.6$ Å^3 cell^{-1} formula unit^{-1}. Pyrite $CuSe_2$ becomes lower in energy at a volume of ~ 55.7 Å^3 cell^{-1} formula unit^{-1}. For marcasite, this would correspond to bulk, volumetric strain of 1.6%, and thus a hydrostatic pressure of ~1.25 GPa, consistent with the experimental pressures reported for bulk synthesis.[15] Despite these differences, the two polymorphs are close in energy.

The metathesis reaction of Na_2Se_2 and $CuCl_2$ was performed in two distinct ways to influence polymorph selection of $CuSe_2$:

$$\mathrm{Na_2Se_2(s) + CuCl_2(s) \xrightarrow[\text{grinding}]{\mathrm{H_2O(g)}} \xrightarrow{\Delta} \text{pyrite } CuSe_2(s) + 2\,NaCl(s),} \tag{4.1}$$

or,

$$\mathrm{Na_2Se_2(s) + CuCl_2(s) \xrightarrow{\Delta} \text{marcasite } CuSe_2(s) + 2\,NaCl(s).} \tag{4.2}$$

When the reactants are ground in humid air (Eqn. 4.1), a color change quickly occurs from brown to black, yielding NaCl, Se, and poorly crystallized phases (Figure 4.2a, bottom). The mixture does not deliquesce. Annealing this mixture at 100 °C (for 24 h) *in vacuo* quantitatively yields bulk pyrite $CuSe_2$ (Figure 4.2a, top). While water inclusion into the crystal structure of pyrite $CuSe_2$ cannot be shown unequivocally, the data suggest that defects in the crystal structure are minimal. The lattice parameter extracted from the Rietveld refinement of the washed pyrite $CuSe_2$ product is 6.125(1) Å, which is 0.2% larger than the reported 6.116(1) Å.[15] Reaction of air-exposed $CuCl_2 + Na_2Se_2$ at 100 °C for six weeks yielded a mixture of both marcasite and pyrite $CuSe_2$, suggesting that the water does not provide a thermodynamic preference for the pyrite polymorph.

The physical properties of pyrite $CuSe_2$ produced under kinetic control were measured to confirm formation of a pure product that exhibits bulk superconductivity. Temperature-dependent magnetic susceptibility measurements reveal a significant diamagnetic response indicative of bulk superconductivity below T_c = 2.4 K, with bulk volume exclusion of the magnetic field (4 $\pi\chi \sim -1$ emu cm^{-3}) (Figure 4.3a). The superconducting transition temperature is unaffected, and H_{c2} is small; together, these suggest that there are no

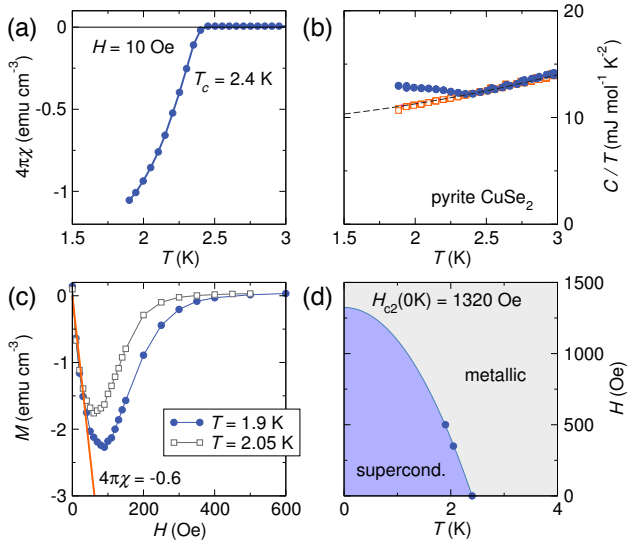

Figure 4.3: Physical properties of the washed pyrite $CuSe_2$ prepared under kinetic control. (a) Magnetic susceptibility as a function of temperature in a 10 Oe field yields a diamagnetic transition at 2.4 K. (b) Heat capacity divided by temperature as a function of temperature in a 10 Oe field (blue) and 1000 Oe field (orange) shows an increase in heat capacity at the same temperature, indicative of a superconducting transition. (c) Magnetic susceptibility as a function of field at multiple temperatures allows the formation of (d) an electronic phase diagram. The line between the two phases traces $H_{c2}(T)$.

significant inclusions into the crystal structure.[123,124] The magnetic susceptibility below T_c indicates total exclusion of magnetic flux from the material and bulk superconductivity, which would not be the case with extensive H_2O inclusion into the crystal structure. Heat capacity measurements also indicate superconductivity, showing the beginning of the jump in the specific heat below T_c. The lack of a sharp jump likely indicates the presence of defects within the crystal, as expected from the low-temperature preparatory route (Figure 4.3b), but is also observed in many other materials (e.g. $Fe_{1+\delta}Se$[125]). Application of a moderately low magnetic field removes the anomaly in the specific heat, as expected given the low H_{c2} of the superconducting state.

Measurements of magnetization as a function of applied field at varied temperatures of the bulk superconductor pyrite $CuSe_2$ indicate that pyrite is a type-II superconductor. Using a two-fluid model ($H_{c2}[T] = H_{c2}[0\text{ K}][1 - (T/T_c)^2]$), we estimate $H_{c2}[0\text{ K}]\sim$1320

Oe. (Figure 4.3c). From this, an electronic phase diagram can be constructed describing the superconducting behavior of the material as a function of temperature and applied field (Figure 4.3d), thus confirming the bulk properties of the material.

When reacted under strictly anhydrous conditions (Eqn. 4.2), no product is formed at $T_{rxn} = 100$ °C after 24 h. NaCl only crystallizes upon exposure to the atmosphere when preparing the sample for PXRD (Figure 4.2b, bottom). This was also confirmed by air-free diffraction of the product in a sealed glass capillary, which showed only starting materials. As a control, incubation of the anhydrous mixture in dry $O_2(g)$ for 24 hours before annealing does not promote a reaction, which suggests that humidity plays a role. When annealed at 300 °C without exposure to the atmosphere, marcasite $CuSe_2$ forms (Figure 4.2b, top, Eqn. 4.2).

The reaction pathway was probed with both *in situ* SXRD and DSC in order to understand the nature of intermediate products (Figure 4.4). The energetics of the reaction vary

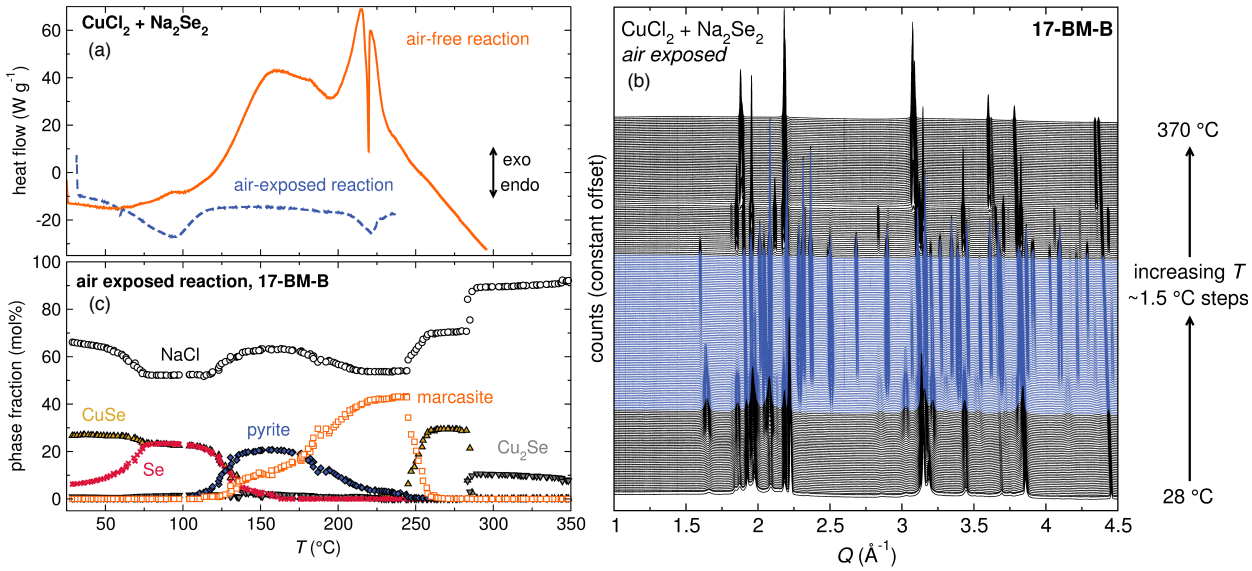

Figure 4.4: (a) DSC curves of the air-free (orange) and air-exposed (blue) reaction of $CuCl_2$ and Na_2Se_2. (b) *In situ* SXRD data collected from the air-exposed reaction mixture, as heated under vacuum. (c) The extracted phase fractions from the Rietveld refinements of the *in situ* SXRD measurements of the air-exposed reaction.

drastically with alteration of the preparatory route. When ground in air, no exotherms are detected by DSC, but rather, a small endotherm near $T = 100$ °C coincides with the initial formation of pyrite $CuSe_2$ (Figure 4.4a). The air-free sample shows significant exotherms as the reaction is heated and NaCl forms (since there is none present after heating at $T = 100$ °C). Both samples show an endotherm around T= 220 °C, likely due to the melting of selenium.

In situ SXRD of the reaction that produces pyrite $CuSe_2$ elucidates the nature of intermediates and decomposition products (Figure 4.4b). After grinding in air and before heating, NaCl, CuSe, and Se are observed, as well as a trace amount of Cu_2Se. As the reaction mixture is heated, the crystalline intermediates (Covellite CuSe and Se) react to form pyrite, followed by marcasite at slightly higher temperatures.

Quantitative phase analysis of the diffraction data with the Rietveld method show that NaCl formation is quantitative before heating. The relative phase fraction only changes due to the increase or decrease of other crystalline components in the reaction mixture (Figure 4.4c). As the reaction mixture is heated, the selenium further crystallizes, noted by a sharpening of Bragg peaks and the decrease in background, which is consistent with the presence of a noncrystalline Se component in the as-ground mixture. By $T \sim 75$ °C, CuSe and Se formation is quantitative with 2 NaCl. From this mixture, pyrite begins to form at $T \sim 90$ °C, at the expense of CuSe and Se, as per the reaction $\mathrm{CuSe} + \mathrm{Se} \longrightarrow p\text{-}\mathrm{CuSe_2}$. The onset of marcasite formation occurs at ~ 110 °C, along with continued pyrite growth. The phase fraction of pyrite begins to decline at $T \sim 175$ °C as the phase fraction of marcasite increases. As the temperature continues to increase, a two-step decomposition occurs to CuSe and Cu_2Se at $T \sim 245$ °C and $T \sim 280$ °C, respectively.

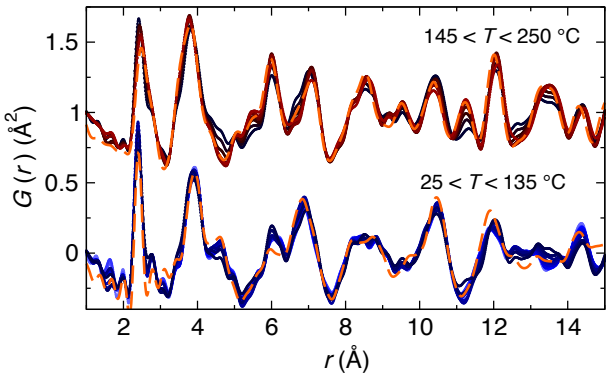

Figure 4.5: PDF analysis of the synchrotron PXRD data. No major changes in the local structure occur below 145 °C, which suggests that the intermediate structures have close relationships to one another. At these lower temperatures, the phases NaCl, CuSe, pyrite $CuSe_2$ provide a reasonable description of the local structure, whereas NaCl, marcasite, pyrite, and CuSe are found at the higher temperatures. At the shortest distances (r 2.2∼2.3 Å), there is some intensity in $G(r)$ that is not accounted for by the calculated patterns, which suggests the presence of some poorly-ordered or amorphous components. (fit curve: dashed orange lines; higher temperature data offset for clarity).

PDF analysis of the total scattering data reveals minimal changes to the local atomic separations for low reaction temperatures, despite the myriad transformations between crystalline phases (Figure 4.5). While the overlap of multiple phases precludes a unique description of $G(r)$, at temperatures below $T = 140$ °C, the local structure is consistent with a linear combination of CuSe [28(11) mol%], pyrite [11(8) mol%] and NaCl [61(17) mol%]. Above $T = 140$ °C, removal of CuSe provides a better description of the PDFs [$CuSe_2$: 36(7) mol%; NaCl: 64(7) mol%, Figure 4.5]. Additionally at low temperatures, the nearest-neighbor correlation is not well described, which suggests there there are poorly-ordered phases between the crystalline phases. While the *in situ* PXRD shows a vast number of changes at low temperatures, the local structure does not, which suggests that there are close structural relationships between the intermediates (CuSe and Se) and product, pyrite $CuSe_2$.

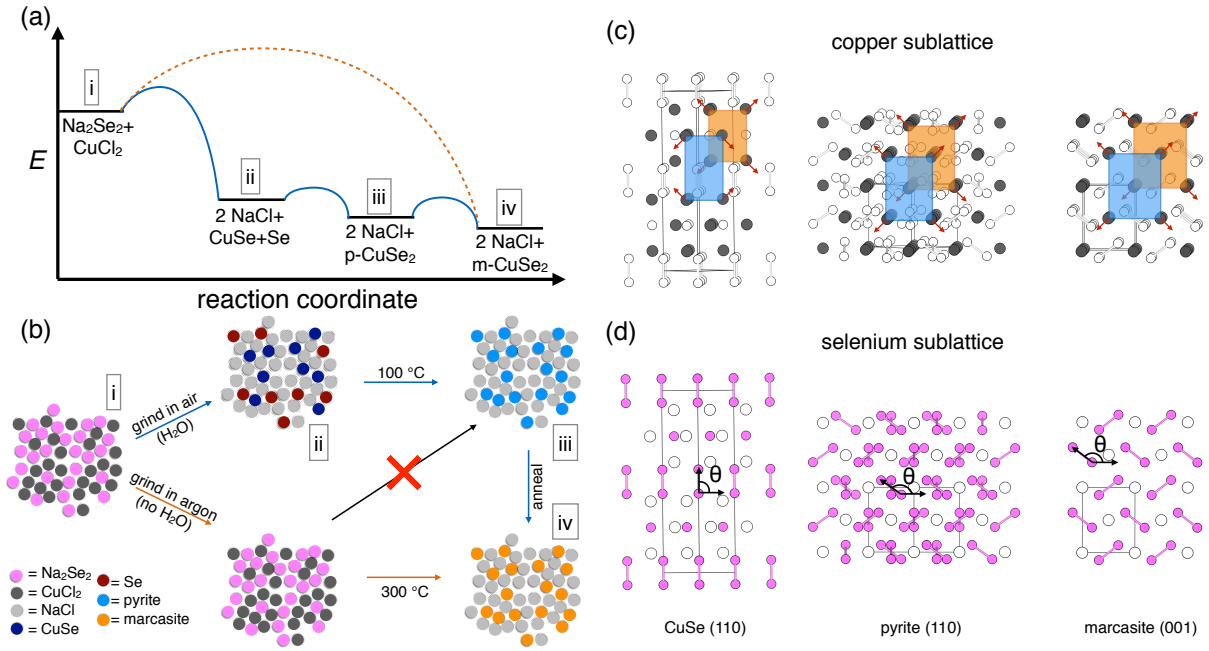

Figure 4.6: (a) Proposed schematic reaction pathway that permits kinetic control of pyrite $CuSe_2$ formation through air exposure. Grinding in air dissipates a large amount of energy through NaCl formation, minimizing the enthalpy difference between the intermediates and pyrite $CuSe_2$ phase. (b) A simplified, proposed reaction scheme of the selective formation of either pyrite or marcasite $CuSe_2$ through solid-state metathesis. The key difference between the formation pathways is that air exposure and thus partial solvation, is necessary to form the reaction intermediates that transform into pyrite. Without partial solvation, pyrite $CuSe_2$ formation is not possible through metathesis. The Roman numerals correspond to the different energy levels in (a). Comparison of the (c) copper and (d) selenium sublattices in covellite CuSe, pyrite $CuSe_2$, and marcasite $CuSe_2$. The transition between the three structures can be explained by a progression of expansion and relaxation. Counterions are shown in white. The corresponding changes in the Cu-Cu distances and selenium dimer rotation are listed in Table 1.

4.4. Discussion

While solid-state metathesis has been extensively explored as a rapid synthetic approach to the formation of refractory borides, carbides, silicides, pnictides, and chalcogenides, these reactions often proceed violently through a propagating ignition wave.[55,57] Depending on the precursors used, solid-state metathesis reactions can also be non-self-igniting,[65] and the reactions have recently been shown to take place via metastable crystalline intermediates.[63] Here, the results indicate that the reaction proceeds at low tem-

perature, thus allowing for kinetic control. This refers to the isolation of the metastable pyrite $CuSe_2$ polymorph, which would be otherwise impossible if executed at higher temperatures, where only marcasite $CuSe_2$ forms. The distinct reactivity between the air-free and air-exposed reactions originates from partial solvation of the reaction mixture. Liquid-assisted mechanochemical reactions have also been used to alter reactions that form organic molecules and metal-organic frameworks,[126,127] and surface hydration has been shown to control polymorphism of nanocrystalline ZnS.[128] Here, partial hydration appears to influence the activation barriers separating crystalline intermediates.

Based on our experimental observations, the schematic reaction coordinate diagram proposed in Figure 4.6a illustrates how kinetic control is likely accomplished. When ground in air, no exotherms appear in the DSC data, because NaCl has already been formed upon grinding, as confirmed by PXRD (Figures 4.2a and 4.4b). We infer that partial hydration of the reactants increases the mobility of the sodium and chloride ions in the solid matrix, which react to form NaCl with a low activation barrier. This in turn drives forward the formation of CuSe and crystalline selenium through the displacement of the remaining ions. Concomitantly, the small endotherm between 60 °C and 100 °C in the air-exposed reaction, indicates that (a) the energy from forming NaCl has already been released and (b) a small activation barrier must be overcome for CuSe and Se to react to form pyrite $CuSe_2$. Upon further heating ($T \sim 130$ °C), the third activation barrier is overcome as pyrite recrystallizes into marcasite $CuSe_2$.

These results are summarized in Figure 4.6b, the steps of which are correlated to the reaction coordinate in Figure 4.6a. Grinding the reactants in air allows energy to be dissipated through the formation of NaCl without exogenous heating (i $\longrightarrow$ ii). From the inter-

mediates of CuSe and Se, heating forms pyrite, then marcasite (ii $\longrightarrow$ iii $\longrightarrow$ iv). Without the initial exposure to air, more heat must be applied to the system, in order to (a) overcome a larger activation barrier which (b) releases sufficient energy from NaCl formation as to drive formation of the most-stable product, marcasite $CuSe_2$ (i $\longrightarrow$ iv).

As a control, CuSe (prepared from the elements) and Se were reacted at $T_{rxn} = 100$ °C. After 24 hours, a small amount of pyrite was detected in the products, as well as unreacted CuSe and selenium. After heating the same reaction mixture for 72 hours, there are equal amounts of pyrite and marcasite, as well as reactants. After eight weeks, four times as much marcasite as pyrite is detected, as well as a small amount of CuSe + Se. As another control, marcasite $CuSe_2$ was mixed with two equivalents of NaCl and held at $T =$100 °C for 500 hours; no pyrite $CuSe_2$ is detected in the products. These controls demonstrate that pyrite $CuSe_2$ is a kinetic product and is in fact metastable at $T = 100$ °C. Previously, mechanochemical reaction of the elements by ball-milling has yielded a mixture of pyrite and marcasite $CuSe_2$, but no phase selectivity or purity was shown.[129]

An additional control of air-exposed $CuCl_2$+Na_2Se_2 was reacted at 100 °C for six weeks. After this long reaction time, both marcasite and pyrite $CuSe_2$ were detected, providing further confirmation of the metastability of the the pyrite polymorph. To determine that it was indeed atmospheric H_2O that caused the transition from $CuCl_2 + Na_2Se_2 \longrightarrow 2\,NaCl +$ CuSe + Se, a silica tube containing the reactants was sealed with $1/3$ of an atmosphere of O_2, and no reaction or color change was observed after heating to 100 °C for 24 hours. Additionally, exposure to N_2 shows no alteration in the reaction mixture.

The activation barriers separating each intermediate phase must be sufficiently small, as the transformations occur at relatively low temperatures. While cursory inspection of

the different crystal structures of CuSe, Se, and pyrite $CuSe_2$ reveals many differences (*e.g.,* distinct Cu coordination, different symmetries and connectivities[15,130]), the lack of significant changes in the PDFs as CuSe and Se transform into pyrite below 140 °C (Figure 4.5) suggests a close structural relationship between these phases. After closer inspection of the reported crystal structures, it is possible to map a displacive transformation with intercalation between the phases.

Table 4.1: Parameters of the phase transitions between CuSe, pyrite, and marcasite, as shown in Figure 6c and 6d.

	Copper sublattice parameters[a]		
	CuSe	pyrite	marcasite
a'	4.93, 6.15	6.12	6.18
b'	3.94	4.32	5.01
plane spacing (Å)	1.97	2.16	2.50
	Selenium sublattice parameters[a]		
	CuSe	pyrite	marcasite
θ	90	125	143
dimer-dimer (Å)	3.94	4.32	5.01
layer-layer (Å)	4.31	3.06	3.09
Se–Se (Å)	2.28	2.35	2.33

[a]Determined from the reported crystal structures of CuSe,[130] p-$CuSe_2$,[131] and m-$CuSe_2$,[131] as determined using VESTA.[132]

To illustrate the relationship, the copper and selenium sublattices are compared separately (Figure 4.6c and 4.6d, respectively). Projection of the copper sublattices comprises overlapping rectangles in the $\{100\}$, $\{101\}$, and $\{001\}$ lattice planes for covellite CuSe, pyrite $CuSe_2$, and marcasite $CuSe_2$, respectively (Figure 4.6c). Alternative crystallographic orientations are depicted in Figure S2. The transformations between the phases can be expressed as expansions and relaxations of rectangles connecting Cu atoms. In CuSe, there are two different sizes of rectangles (Table 4.1). As selenium reacts with the CuSe lattice, the larger rectangles shorten and widen, while the smaller rectangles widen and lengthen. This follows with formation of Se–Se dimers in the trigonal planar Cu–Se $\{004\}$ layers,

which fall in the center of the of the smaller rectangles. Additionally, the space between the rectangles increases as selenium intercalates.

The selenium sublattice of CuSe is comprised of both $[Se_2]^{2-}$ dimers (shown with bonds in Figure 4.6d) and discrete Se^{2-} anions.[133,134] As additional selenium intercalates into the layers of Se^{2-} anions to form dimers, the preexisting dimers tilt away from the c-axis of CuSe. The pyrite $CuSe_2$ selenium sublattice consists of these Se dimers, tilted either along the plane (as shown) or rotated by 90 degrees. As they tilt, the distance between nearest-neighbor dimers increases compared to CuSe, but the layers become close-packed and the Se–Se bond length increases ($CuSe_2$ can be described as two interpenetrating face-centered cubic lattices, with one *fcc* lattice of copper, and the other formed by the center-of-mass of the dimer).[111]

To convert pyrite to marcasite, both the copper and selenium sublattices further relax. The rectangular planes of copper atoms increase in size and move further from one another. The Se–Se dimers relax further off-axis and reorient along the same direction, thus losing the close-packed nature of the pyrite structure.

4.5. Conclusion

While many metastable phases can be formed by tuning an extrinsic thermodynamic parameter (*e.g.,* temperature, pressure, dielectric constant of a solvent), quantitative isolation of the metastable, high-pressure superconducting polymorph of $CuSe_2$ was achieved via kinetic control of solid-state metathesis. The titration of the enthalpy release from NaCl formation enables the reaction to proceed through kinetic control. From close analy-

sis of the reaction pathway using *in situ* x-ray scattering, the activation barriers are limited by displacive structural rearrangement of crystalline intermediates (CuSe and Se): pyrite $CuSe_2$ is a kinetic intermediate in the reaction CuSe + Se $\longrightarrow$ marcasite $CuSe_2$: intercalation of selenium into the CuSe lattice forces the structure to form pyrite on its way to marcasite. Heating the reaction for longer times or higher temperatures leads to recrystallization into the equilibrium marcasite $CuSe_2$ polymorph. This reaction can be thought of as a manifestation of the Ostwald step rule,[135] whereby less stable intermediates form first, since formation of their surface is less energetically costly than the most stable polymorph.[136] These findings provide broad implications for achieving materials by design and the discovery of new, functional materials, demonstrating how altering chemical pathways can influence the crystal structure and thus the properties of the material.

5. Lewis Base Mediated Polymorph Selectivity of Pyrite $CuSe_2$ Through Atom Transfer In Solid State Metathesis[†]

5.1. Introduction

Synthesis of transition metal dichalcogenides is a recurring goal of synthetic inorganic and solid state chemists, due to the varied and tunable electronic properties of the products.[15,70,137] Polymorphism, when more than one crystal structure can be prepared of a single chemical composition, can provide access to novel functionality. However, preparation and isolation of a specific polymorph presents unique challenges, because traditional solid-state chemistry techniques yield products of the lowest energy atomic configuration for a given set of thermodynamic parameters, due to the use of high-temperature conditions to overcome activation barriers associated with solid state diffusion. Thus non-traditional preparatory routes are required in order to isolate polymorphs that may not be in equilibrium with ambient conditions.[2,5,17] While non-self propagating solid-state metathesis (double exchange) reactions do not usually require high-temperature conditions relative to the conditions required for their respective elemental reactions, the propagation of these reactions tend to be limited by the transfer of atomic species between reactants or formation of a new surface.[56,62]

[†]Substantial portions of this chapter have been reproduced with permission from A. J. Martinolich, R. F. Higgins, M. P. Shores, and J. R. Neilson, *Chem. Mater.* **2016**, *28*, 1854–1860, reference 99, © 2016 the American Chemical Society

One such example of polymorphism is the superconductor $CuSe_2$: the compound crystallizes with the marcasite structure at ambient pressures and $T < 340$ °C,[119] and has a superconducting transition temperature, $T_c = 0.7$ K. The pyrite polymorph of $CuSe_2$ has an increased superconducting transition temperature ($T_c = 2.4$ K); its preparation from the elements requires the application of high pressure (65 kbar) and high temperature (1000 °C).[14]

Previously, we used a metathesis reaction to greatly reduce the temperature and pressure requirements to selectively form pyrite $CuSe_2$, which hinged upon exposing the reaction mixture to air before annealing.[98] This additional step of air exposure allows the intermediate reaction $Na_2Se_2 + CuCl_2 \longrightarrow 2\,NaCl + CuSe + Se$ to proceed and decouples the formation of $CuSe_2$ from the exothermic formation of NaCl. Pyrite $CuSe_2$ formation occured upon annealing the reaction mixture at 100 °C and is slightly endothermic. Without air exposure, no reaction occurred at 100 °C, but annealing at 300 °C yields formation of the marcasite polymorph through an exothermic process, similar to previous studies of solid-state metathesis reactions.[56,62,63] We hypothesized that air exposure allows partial solvation of the reactants by atmospheric H_2O, increasing mobility of the ions in the solid matrix, and thus promoting NaCl nucleation and growth, but this hypothesis remained equivocal due the uncontrolled exposure of the reaction to air. The goal of this contribution is to understand the chemical origins of the polymorph selectivity through controlled addition of a reactive, but non-incorporating, molecule to the reaction mixture of $CuCl_2 + Na_2Se_2$.

Small organic molecules have previously been used for a range of atom-transfer reactions in inorganic and nano-scale materials chemistry. Thiosilanes have been used to

form a range of Cd and Hg chalcogenides and organometallic complexes through metathesis.[138] Organosulfides combined with alkyl tin halides results in the formation of a range of organosulfur tin complexes.[139] In forming extended solids, hexamethyldisilathiane has been used as a sulfur source in metathesis reactions; the volatile trimethylsilylchloride byproduct is then easily removed from the metal sulfide product.[140,141] Phosphines have been shown to readily react with elemental sulfur and organosulfides to form $R_3PS(R')$ adducts.[142,143] Alkyl and aryl phosphines are widely used as chalcogen sources, capping agents, and surfactants in nanomaterial synthesis and processing. Trioctylphosphine has been demonstrated to extract sulfur and selenium from iron, cobalt, nickel, and tin chalcogenide nanoparticles, yielding the most metal-rich binary in the metal-chalcogen system.[144] When serving as a sulfur or selenium precursor, alteration of the organic groups on the organophosphine chalcogenide R_3PQ (Q = S, Se) to make them more or less electron-withdrawing has been shown to alter the reactivity of the phosphine and provide control over composition and morphology of nanocrystalline $CdS_{1-x}Se_x$.[145] In all cases, the organic component is used in stoichiometric or excess amounts compared to the transition metal source or product, since it acts as a reagent rather than a mediator of the reaction.

Herein, we show that the formation of the metastable pyrite $CuSe_2$ polymorph through solid-state metathesis of $CuCl_2$ and Na_2Se_2 is enabled by Lewis-base mediated atom transfer of both Cu and Se; nonbasic analogs do not show this selectivity. Ph_3P and tris-*ortho*-tolylphosphine (o-$CH_3Ph)_3P$) are crystalline solids at room temperature, are canonical Lewis bases, and are soluble in most organic solvents. These additives are solid at room temperature and bench stable, leading to relatively few additional experimental hazards. The solubility afforded by the bulky aryl groups thus permits facile separation from the

final product. Quantitative phase analysis of powder X-ray diffraction (PXRD) of the reaction products indicates that small amounts of the Ph_3P promote significant pyrite $CuSe_2$ formation. Nuclear magnetic resonance (NMR) and infrared (IR) spectroscopies support the formation of a Ph_3PSe adduct, and mass spectrometry (MS) indicates the formation of multiple $Cu(Ph_3P)_n^+$ species. These molecular intermediates appear to increase diffusion of the ions in the reaction mixture and are integral to the formation and stabilization of the pyrite polymorph, but are incapable of forming a crystalline product from their direct reaction. The selectivity for the metastable phase is not observed when the exogenously-added organic molecule is changed to be either non-basic or non-melting species.

5.2. Materials and Methods

Note on author contributions: This chapter was published in *Chemistry of Materials*, **2016**, volume 28, page 1854, by Andrew J. Martinolich, Robert F. Higgins, Matthew P. Shores, and James R. Neilson. AJM performed solid state reactions, collected PXRD and NMR data, analyzed the data, and wrote the initial draft of the manuscript. RFH collected GC-MS and IR data, prepared the compounds Ph_4C, $(Ph_3P)_2CuCl_2$, and $(Ph_3P)_3CuCl$, and analyzed data. MPS aided in supervision of the project and provided useful discussion. JRN analyzed data and supervised the project. All authors contributed to the editing and finalization of the manuscript.

All reactants were prepared in an argon-filled glove box. Na_2Se_2 was prepared from the elements, with each contained in a separate alumina crucible to prevent a violent thermite reaction. A 2% excess of sodium was used to account for surface oxidation of the alkali.

The crucibles were put in a silica ampoule, evacuated to $\leq$ 10 mtorr and sealed, then heated at 1 °C min^{-1} to 400 °C and allowed to dwell for 12 h. The reactants (now all in the crucible originally containing the Na) were collected, ground homogeneously, pelleted, and heated a second time with the same parameters. The product was then analyzed using PXRD to confirm purity in a sealed silica capillary on a Bruker Apex II with a MoKα source in transmission mode to keep the sample free from air. Tetraphenylmethane was synthesized according to the literature from treatment of triphenylchloromethane with phenyllithium;[146] its purity was confirmed by ^{1}H NMR and melting point. $(Ph_3P)_2CuCl_2$ was synthesized from $CuCl_2$ and Ph_3P in ethanol; its purity was confirmed by MS and IR spectroscopy.[147] $(Ph_3P)_3CuCl$ was synthesized from CuCl and Ph_3P in chloroform; its purity was confirmed by MS and IR spectroscopy.[148]

The Na_2Se_2 was combined with a stoichiometric amount of anhydrous $CuCl_2$ (Alfa Aesar, 98+%) and ground homogeneously. Ph_3P (Alfa Aesar, 99+%) was then added in various proportions (4–100 mol% per mole $CuCl_2$) to the reaction mixture and reground to homogeneity. Upon grinding the reaction mixture with Ph_3P in an Ar-filled glovebox, a slight color change from brown to black occurs; the color change is especially noticeable with larger amounts of Ph_3P added. The mixture was then pelleted and placed in a scintillation vial with a polytetrafluoroethylene (PTFE) lined screw-top lid and tightened to guarantee a sealed reaction vessel under inert Ar gas. The reaction vessels were then heated from room temperature to 150 °C at a rate of 10 °C min^{-1}. After 24 hours, the mixtures were air quenched.

Reactions of $(Ph_3P)_2CuCl_2 + 2\,Ph_3PSe$ and $(Ph_3P)_3CuCl + 2\,Ph_3PSe$ seeded with $\approx$ 3 mg pyrite $CuSe_2$ were executed under argon in scintillation vials with PTFE-lined caps at

150 °C for 24 hours. The products were washed with benzene and mixed with a known amount of elemental silicon powder (as an internal standard) and PXRD patterns were analyzed using the Rietveld method. Quantitative phase analysis indicated that no more pyrite $CuSe_2$ had formed.

All X-ray diffraction patterns were collected on a Scintag A2 diffractometer with a CuKα source. Fourier transform infrared spectroscopy was performed on a Nicolet 380 FT-IR spectrophotometer. ^{1}H NMR and ^{31}P NMR spectra were collected using an Agilent (Varian) 400 MHz NMR spectrometer in deuterated benzene (C_6D_6). Mass spectrometry experiments were performed in CH_3OH in the positive ion mode on a Finnigan LTQ mass spectrometer, equipped with an analytic electrospray ion source and a quadrupole ion trap mass analyzer. Each measurement was performed with the capillary temperature = 175 °C, spray voltage = 5 kV, and spray current = 91 μamps. Magnetic measurements were performed using the vibrating sample magnetometer option of a Quantum Designs Inc. Physical Properties Measurement System. X-ray photoelectron spectroscopy data were collected on a Physical Electronics ESCA 5800 system with a monochromatic Al Kα X-ray source. High resolution scans of the core levels were performed with a pass energy of 23.5 eV and a step size of 0.10 eV/step.

5.3. Results and Discussion

The reaction $CuCl_2 + Na_2Se_2 + \ n\ Ph_3P$ can be driven to increase the yield of the pyrite polymorph of $CuSe_2$ over 120 hours at 130 °C, regrinding the reaction mixture every 24 hours in an Ar-filled glovebox. At reaction times before 120 hours, CuCl and Se are also

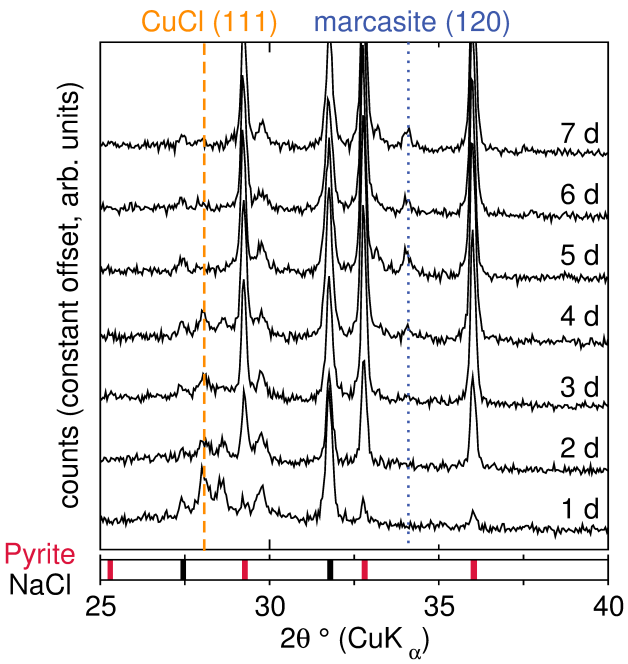

Figure 5.1: PXRD patterns products of reaction between $CuCl_2$ and Na_2Se_2 at 130 °C with ≈ 10 % by mass Ph_3P in the reaction mixture. The reaction mixture was reground every 24 hours in an Ar-filled glovebox. The dashed orange lines at $2\theta \approx 28$ and 34 correspond to the strongest CuCl (orange) and marcasite $CuSe_2$ (blue) reflections, respectively. Expected reflections for pyrite $CuSe_2$ and NaCl are shown below. Pyrite $CuSe_2$ and NaCl are observed throughout; marcasite $CuSe_2$ is observed as all CuCl is consumed.

observed via PXRD (Figure 5.1). Beyond 120 hours, partial conversion from pyrite to marcasite is observed. The slow completion of the reaction is likely caused by the stabilization of the CuCl intermediate by the Ph_3P, as suggested by mass spectrometry (Figure 5.2a). A CH_3OH wash of the products after 4 days at 130 °C analyzed by MS confirmed the formation of $Cu(Ph_3P)_n^+$ (n = 2,3). The colored vertical lines in Figure 5.1 indicate the positions of the strongest CuCl (≈ 28 2θ, orange) and marcasite $CuSe_2$ (≈ 34 2θ, blue) reflections. After 4 days at 130 °C, the CuCl is no longer detected and conversion from pyrite $CuSe_2$ to marcasite is observed. This supports the notion that pyrite is a metastable product of the reaction and its formation is dependent on the other species present in the reaction mixture; as the intermediates are used up the conversion to the marcasite polymorph is observed.

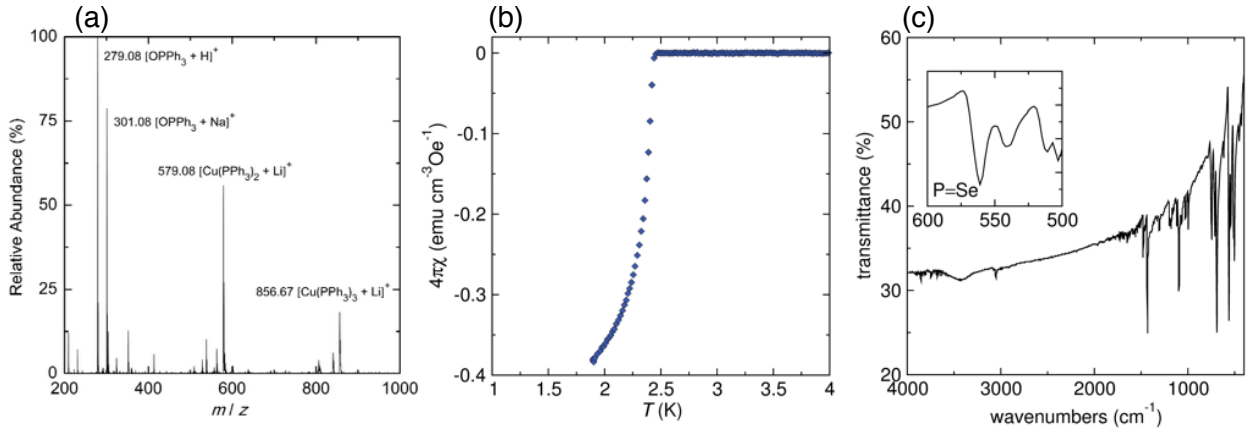

Figure 5.2: (a) Mass spectrum of $CuCl_2 + Na_2Se_2 + 0.1\,Ph_3P$ reacted at 130 °C for 96 hours with intermittent grinding every 24 hours, performed in CH_3OH with the four most intense peaks labelled. The triphenylphosphine oxide formation is a result of the conditions used to perform to experiment. (b) Measurement of magnetic susceptibility as a function of temperature indicates a transition to a superconducting state at T_c = 2.4 K in a sample of $CuSe_2$ produced from $CuCl_2 + Na_2Se_2 + 0.1\,Ph_3P$ reacted at 150 °C for 24 hours, then washed 5 times each with benzene and methanol. (c) IR spectrum of the products of $CuCl_2 + Na_2Se_2 + 0.97\,Ph_3P$. The inset shows the characteristic P=Se stretch at 560 cm^{-1} , which is not present in either the Ph_3P or Ph_3P=O spectra.

While phosphorous inclusion into (and possible stabilization of) the pyrite structure cannot be ruled out completely, it is unlikely under these reaction conditions. Previous reports of transition metal phosphide nanomaterial formation using trioctylphosphine as a phosphorous source required much higher temperatures ($T \geq 300$ °C) to break the C–P bonds,[153–155] and phosphine-chalcogenide adducts have previously been used at much higher temperatures as sulfur and selenium sources to form $CdSe_{(1-x)}S_x$, with no phosphorus inclusion.[145] ^{1}H NMR of the products washed in deuterated methanol shows no residual benzene or phenol from the C–P bond scission of Ph_3P. Additionally, the eventual conversion to the thermodynamically stable marcasite polymorph at longer reaction times suggests that the pyrite is a kinetic product and is not stabilized by phosphorous substitution. X-ray photoelectron spectroscopy indicates the presence of Ph_3PSe[149] on the surface of the material after multiple washes with benzene and methanol (Figure 5.3), but no copper phosphide phases. Magnetization measurements show no change in the super-

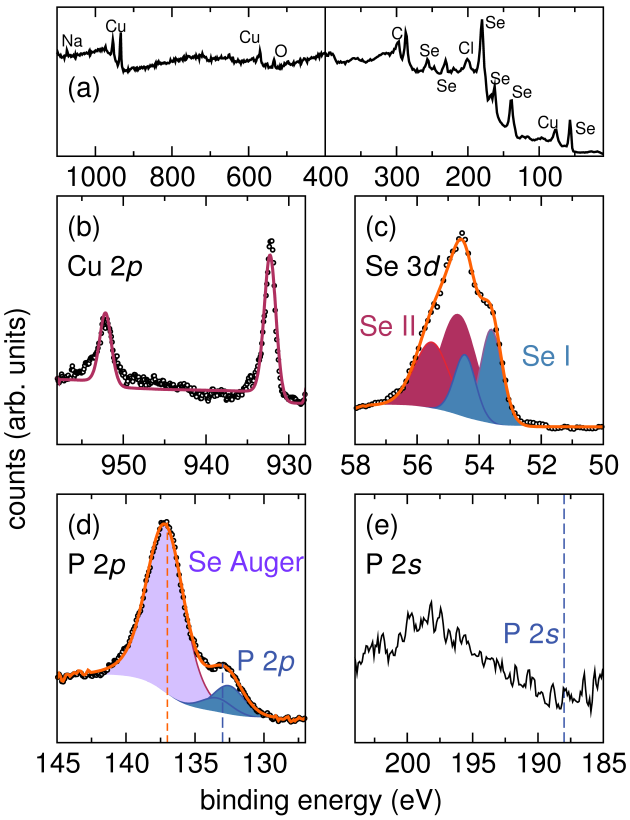

Figure 5.3: (a) Survey X-ray photoelectron spectrum with peaks labelled. Note the split x-axis at 400 eV. High resolution spectra of (b) the Cu 2*p*, (c) Se 3*d*, (d) P 2*p*, and (e) P 2*s* energies, with fits where applicable. The P 2*p* line (133 eV, large blue dashes) corresponds to Ph_3PSe,[149] and partially overlaps with a selenium Auger line (137 eV, small orange dashes).[150–152] Multiple peaks in the fits are due to spin-orbit splitting of Se and P environments in (c) and (d), respectively. No signal is apparent in the P 2*s* region (expected: 188 eV, large blue dashes)

conducting transition temperature T_c (Figure 5.2b); both support the conclusion that no phosphorus is unintentionally doped into the $CuSe_2$ product.

To study the effects of the Ph_3P on the metathesis reaction, reactions were executed for 24 hours without intermittent grinding. This allows the results to be attributed solely to the presence of Ph_3P and conclusions to be drawn regarding the nature of the organic additive and its participation in the metathesis reaction. At reaction temperatures below 150 °C without intermittent grinding, the conversion to products is not as pronounced, making it more difficult to glean the role of the Ph_3P in the reaction. At 150 °C, a significant conversion to products was observed in a relatively short period without intermittent

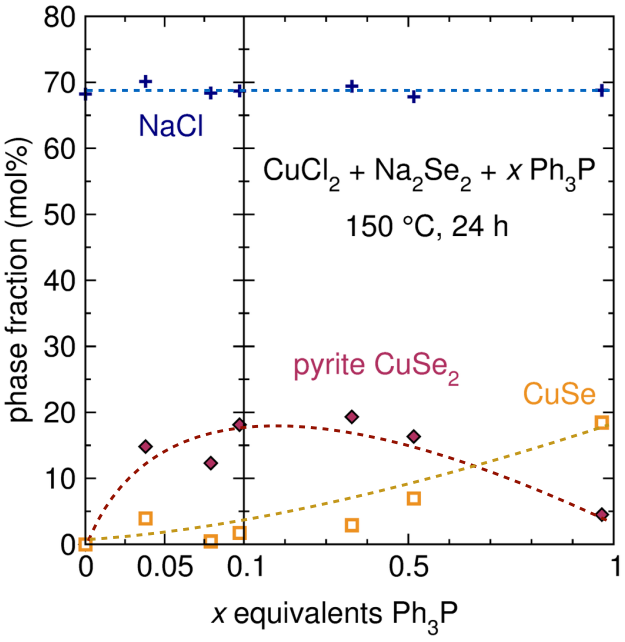

Figure 5.4: Molar phase fractions of NaCl, $CuSe_2$, and CuSe extracted from the Rietveld refinements of PXRD patterns of the products of $CuCl_2 + Na_2Se_2 + x$ Ph_3P after 24 hours at 150 °C. Adding more than $\approx$ 10% Ph_3P does not promote further pyrite formation, and at increased concentrations Ph_3P promotes CuSe formation rather than $CuSe_2$. NaCl content remains relatively constant, and quantitative at $\approx$ 67%. Dashed lines serve as a guide to the eye. Phase fractions of CuCl and selenium are omitted for clarity. Note the split x-axis at $x = 0.1$.

grinding, and no marcasite was detected after 24 hours, indicating that the reaction remains under kinetic control. Above 150 °C, the formation of marcasite $CuSe_2$ is observed. Thus, 150 °C was determined as an appropriate reaction temperature to study the effects of the organic additive.

A number of reactions were executed with varied amounts of added Ph_3P. The phase fractions of NaCl, CuSe, and pyrite $CuSe_2$ derived from Rietveld refinements of the PXRD data are shown in Figure 5.4. The amount of pyrite observed after 24 hours reaches a maximum with $\approx$ 0.1 molar equivalents Ph_3P added per mole of reactants. As the amount of Ph_3P is further increased, the phase fraction of pyrite $CuSe_2$ decreases while CuSe increases, suggesting that the Ph_3P is consuming a significant amount of the selenium in the reaction mixture to form Ph_3PSe. Yields of NaCl are approximately quantitative in all

reactions, but the formation of CuSe, Se, and CuCl intermediates prevents quantitative formation of $CuSe_2$ without longer reaction times. In the reaction without added Ph_3P, NaCl is observed because it forms upon preparation for the PXRD measurement, as we have previously shown.[98] Marcasite $CuSe_2$ was not detected at any level of added Ph_3P.

The formation of CuSe instead of $CuSe_2$ at increased Ph_3P levels suggests selenium uptake by Ph_3P. While this may slightly alter the yield of $CuSe_2$ at all concentrations, the fact that such small fractions of added Ph_3P still promote the formation of pyrite $CuSe_2$ suggests that the Lewis base may act as a selenium shuttle, either continually binding and transferring Se from the Na_2Se_2 reactant, or allowing enough sodium ions to be dissociated to induce NaCl nucleation and growth, as well as bulk dissociation of Cu^{2+} cations. While the energy of a Cu–Se bond is weaker than that of a P–Se bond (70(9) kcal mol^{-1} *vs.* 87(2) kcal mol^{-1}),[156] the lattice enthalpy will be greater than formation of relatively few phosphorus selenium bonds, driving the reaction to form the crystalline $CuSe_2$ products ($\Delta H_{\text{lattice}} = -190$ kcal mol^{-1}).[98]

While our previous report indicated that annealing the air-exposed reaction mixture at 100 °C was sufficient to promote pyrite $CuSe_2$ formation, small additions of Ph_3P in lieu of air exposure yielded no $CuSe_2$ formation after reaction at 100 °C. We hypothesize that the slightly higher temperatures used in these reactions are necessary to induce further mixing and diffusion of the reactants when the amount of Ph_3P is limited, whereas the air-exposed reactants were most likely exposed to an excess of H_2O vapor and not limited by its availability as a partial solvent. The increased temperatures may also aid in explaining the observation of CuCl in the reaction mixture, which was not observed in the previous work. Increasing the reaction temperature above 100 °C may stabilize the CuCl, as we

have shown that a number of intermediates may form depending on reaction temperature and that it is feasible to observe redox activity in solid-state metathesis reactions.[63]

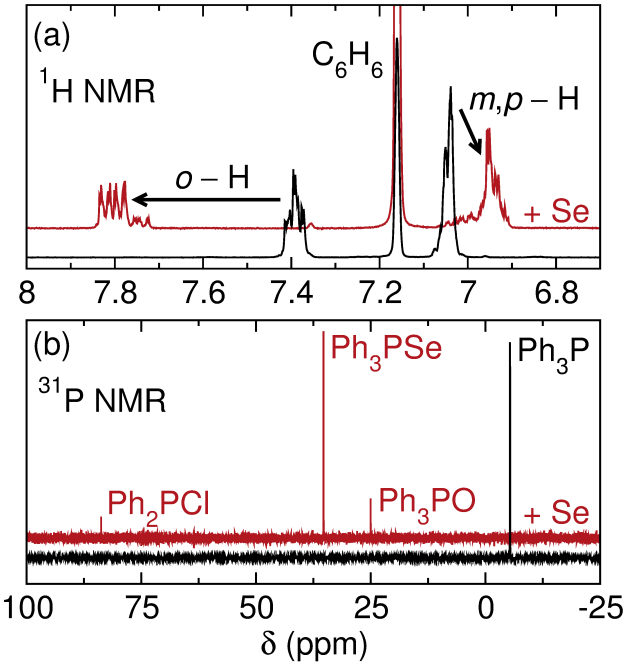

Figure 5.5: (a) The aromatic region of the ^{1}H NMR spectra shows the Ph_3P (black) and benzene-soluble products of the reaction $CuCl_2 + Na_2Se_2 + 0.97\,Ph_3P$ (red), with shifts of each resonance indicated. (b) The corresponding ^{31}P NMR spectra of the same solutions shows no Ph_3P remaining in the reaction mixture, indicating the presence of Ph_3PSe, Ph_3PO, and Ph_2PCl.

The formation of a selenium-Ph_3P adduct is supported by IR, ^{1}H NMR, and ^{31}P NMR spectroscopies. The IR spectrum shows a characteristic absorption at 560 cm^{-1}, corresponding to the P=Se stretch (Figure 5.2c).[157] The ^{1}H NMR spectra of Ph_3P and the metathesis reaction products with 0.97 equivalents of Ph_3P in deuterated benzene are shown in Figure 5.5b. The resonances in the neat Ph_3P centered around 7.39 ppm (corresponding to the *ortho* protons) shift to $\approx$ 7.8 ppm, while those centered around 7.05 ppm (corresponding to the *meta* and *para* protons) shift to 6.95 ppm. The introduction of the electronegative Se atom onto the phosphorous atom deshields the ortho protons by withdrawing electron density. Further, the meta and para protons are less affected due to the

overall distance of the change that was made in the molecule and show minimal changes overall. Integrations of each set of peaks correspond to a 2:3 ratio accordingly, and agree with reported literature values.[158] Chemical shifts in the ^{31}P NMR spectra (Figure 5.5c) indicate full consumption of the starting material (Ph_3P), and the presence of Ph_3PSe, as well as small signals attributed to Ph_3PO and Ph_2PCl.[159]

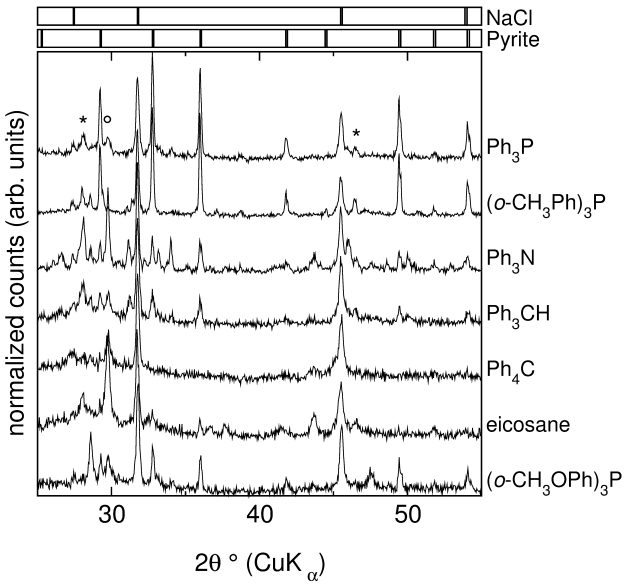

Figure 5.6: PXRD patterns of the products of $CuCl_2 + Na_2Se_2 + 0.1$ X where X is the organic molecule indicated at right. The expected reflections for NaCl and pyrite $CuSe_2$ are shown above. Strongest reflections present from CuCl ($*$) and Se ($\circ$) are marked.

To experimentally test the importance of Lewis basicity in mediating the metathesis, we performed the metathesis reaction with triphenylamine (Ph_3N), which is a non-basic analog of Ph_3P.[160,161] Both pyrite and marcasite were detected via PXRD after 24 hours, as well as much larger amounts of CuSe and elemental selenium (Figure 5.6). Since it is not likely that a Ph_3NSe adduct is forming with the nonbasic amine, we hypothesize that the Ph_3N is providing an alternative reaction pathway that does not involve complex intermediate formation, and therefore does not provide control over the polymorph of the $CuSe_2$ product.

Since Ph_3P and Ph_3N are both liquid at 150 °C (T_m = 80 and 127 °C, respectively), it is likely that diffusion of the reactants are increased due to this fact alone. Because Ph_3P is a Lewis base, it forms the Ph_3PSe adduct, which is not possible for the nonbasic Ph_3N. We suggest that the adduct formation simultaneously slows the propagation of the reaction and allows the pyrite polymorph of $CuSe_2$ to be formed before the marcasite polymorph. Reaction propagation of the Ph_3N-containing reaction is not slowed by any adduct formation, and polymorph selectivity is lost.

Triphenylmethane (Ph_3CH, T_m = 92 °C) and tetraphenylmethane (Ph_4C, T_m = 272 °C) are both nonbasic, and were each combined with the reaction mixture $CuCl_2 + Na_2Se_2$ to test the necessity of a melt (Figure 5.6). With Ph_3CH, both polymorphs of $CuSe_2$ were detected, in a similar fashion to the Ph_3N. In the case of Ph_4C, only NaCl and selenium were detected in the products, reminiscent of the reaction mixture with no additive. These control reactions indicate that the addition of a liquid to the reaction mixture is required to allow any reaction to proceed.

Eicosane ($C_{20}H_{42}$, T_m = 36 °C) was also introduced to test a completely nonpolar, unreactive molecule that will melt. After 24 hours at 150 °C with 0.1 molar equivalents of eicosane, very little $CuSe_2$ was detected; instead much more Se and CuSe were observed (Figure 5.6). This again indicates that the reaction is promoted by the presence of the liquid phase additive, but again polymorph selectivity is lost because the eicosane is unreactive with respect to the reaction mixture.

While these controls indicate that a melt may promote reaction in the solid matrix, they do not specifically attest to the influence of the Lewis-basic phosphine. Tris-*ortho*-methoxyphenylphosphine [(*o*-$CH_3OPh)_3P$, T_m = 200 °C] is a Lewis base but will be solid

under the reaction conditions. Therefore, (o-$CH_3OPh)_3P$ was mixed with $CuCl_2 + Na_2Se_2$ and reacted at 150 °C. After 24 hours, NaCl, CuCl, Se, and pyrite $CuSe_2$ were observed via PXRD (Figure 5.6). However, much less pyrite $CuSe_2$ was observed compared to a reaction at 150 °C with Ph_3P. As a positive control of a Lewis base that is liquid under the reaction conditions, tris-*ortho*-tolylphenylphosphine [(o-$CH_3Ph)_3P$, T_m = 123 °C] was added to the reaction mixture and reacted at 150 °C for 24 hours, yielding the pyrite polymorph of $CuSe_2$ (Figure 5.6). These results indicate that a melt works in concert with the presence of a Lewis base to provide polymorph selectivity of $CuSe_2$.

The organic adducts detected, $Cu(Ph_3P)_n^+$ and Ph_3PSe, may be reacting with one another to form CuSe or pyrite $CuSe_2$. Their reaction would replenish the Ph_3P after doing so and allow the solid-to-solid reaction to propagate. To test this alternative hypothesis, the reactions $(Ph_3P)_2CuCl_2 + 2\,Ph_3PSe$ and $(Ph_3P)_3CuCl + 2\,Ph_3PSe$ were both executed in the solid state at 150 °C and in toluene at reflux (T = 110 °C); no crystalline products were formed in either case. Additionally, reactions of the molecular intermediates seeded with pyrite $CuSe_2$ resulted in no further product formation. These controls indicate that the intermediates alone are not forming the products and that a solid interface or mixture must first be present for the products to form.

Taken together, these data suggest a distinct reaction mechanism compared to our previous report using air exposure to provide polymorph selectivity. We previously hypothesized that the pyrite polymorph was formed through a topochemical selenium insertion and slight structural rearrangement from CuSe to pyrite at low temperatures, then forming marcasite as the temperature increased. Here, Ph_3P serves as a selenium shuttle. The significantly slower kinetics and higher thermal activation barrier relative to the air-

exposed reaction suggest that the presence of multiple organic-inorganic moieties (Ph_3PSe, $Cu(Ph_3P)_n^+$) may be stabilizing the surface of pyrite $CuSe_2$ while reacting with the inorganic reactants and intermediates. As the concentration of Ph_3PSe and $Cu(Ph_3P)_n^+$ adducts decrease and the NaCl and $CuSe_2$ products form, stabilization of the pyrite surface is lost and rapid conversion to the thermodynamically-stable marcasite polymorph is observed. This embodies Ostwald's Step Rule, which states that as a product crystallizes it will form metastable intermediates before the thermodynamically stable product.[135,136] The hypothesized reaction pathway is summarized in Scheme 1. Initial reaction of $CuCl_2 + Na_2Se_2$ yields a range of intermediates after addition of Ph_3P and heating (**reaction 1**). Further heating induces formation of pyrite $CuSe_2$, formed by the organic intermediates **a** and **b** on a crystalline template (e.g., Se intercalation into CuSe, **reaction 2**). It is likely that reactions 1 and 2 occur repeatedly as x decreases and y increases. As the inorganic intermediates are consumed, conversion to the marcasite polymorph begins to occur (**reaction 3**).

The role of Ph_3P in this reaction is twofold: (a) the Ph_3P melts, and increases the diffusion and activity of the reactants, and (b) $Cu(Ph_3P)_n^+$ and Ph_3PSe adducts form, slowing the propagation of the reaction and allowing kinetic stabilization of the pyrite $CuSe_2$ product. If a molten, non-adduct forming molecule is added, the reaction progresses without polymorph selectivity.

The intermediate stability and thus potentially the reaction kinetics could potentially be tuned by altering the electron donating or withdrawing properties of the organic functionality on the phosphine center.[145,162] In general, the formation of these intermediate adducts seems integral to the controllable propagation of the reaction $CuCl_2 + Na_2Se_2$,

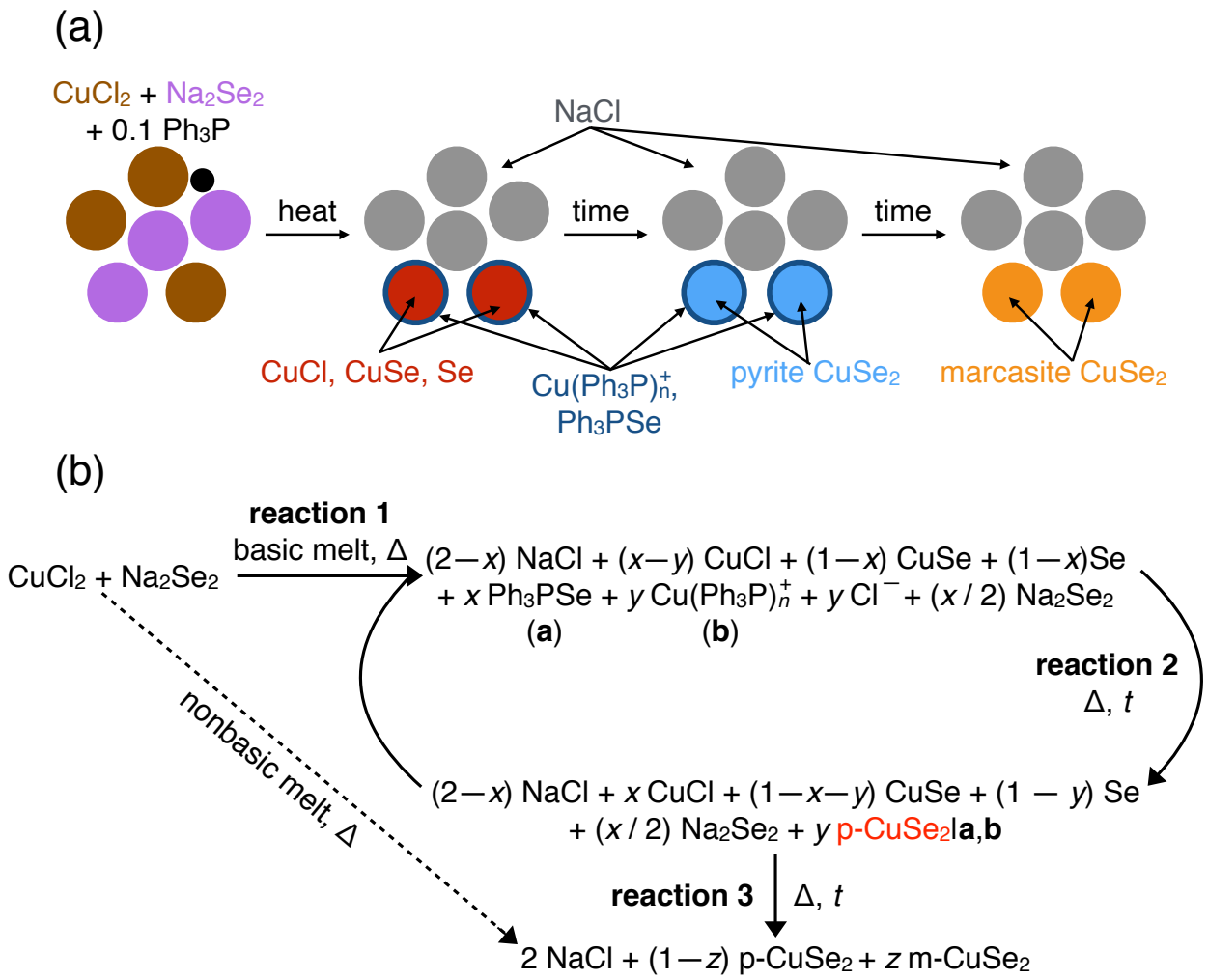

Figure 5.7: (a) A cartoon summarizing the polymorph-selective pathway of $CuSe_2$ formation, mediated by Ph_3PSe and $Cu(Ph_3P)_n^+$. (b) The hypothesized reaction pathway yielding polymorph selectivity of $CuSe_2$. Formation of **a** and **b** allow the stabilization of the pyrite polymorph before conversion to marcasite at longer reaction times. Without the addition of the Lewis base, no selectivity is observed and direct formation of marcasite occurs. (e.g., direct, dashed arrow)

and Lewis-base adducts provide a new pathway for solid-state chemistry to take place in a controlled manner.

5.4. Conclusion

In conclusion, we have demonstrated Lewis-base mediated solid-state chemistry at low temperatures for the reaction $CuCl_2 + Na_2Se_2$, which selectively forms the nominally high-

pressure, high-temperature pyrite polymorph of $CuSe_2$. Formation of multiple copper- and selenium-containing intermediates alters the reaction pathway and stabilizes the pyrite polymorph. Addition of other organic molecules that are either nonbasic or non-melting at the reaction temperatures tested do not allow for polymorph selectivity between pyrite and marcasite $CuSe_2$. The formation of the organic intermediates Ph_3PSe and $Cu(Ph_3P)_n^+$ are integral to the formation of one polymorph over the other, but are unable to react on their own to yield a crystalline product. Inclusion of small amounts of non-incorporating small molecules with the ability to form complex intermediates with the solid-state reactants into solid-state chemical reactions has the potential to yield a range of metastable products previously unobtainable through traditional solid-state synthetic means.

6. Outlook and Proposed Future Directions

6.1. Introduction

This body of work focused on the development of kinetic control of solid state metathesis reactions. To this end, we have presented the observation of kinetic intermediates,[63] pathway control,[95] and polymorph control[98,99] to produce transition metal dichalcogenides through solid state metathesis and under kinetic control.[1]

Moving forward, it will be important to understand the precise nature of the chemical interactions that allow these examples of kinetic control. This will in turn yield a greater understanding of how kinetic control can be exercised over a wider range of solid state chemical reactions.

6.2. Materials and Methods

Note on author contributions: The following work is currently in preparation for publication, and stems from the work of multiple scientists. Andrew J. Martinolich performed triphenylphosphine flux and solid state metathesis reactions, executed *in situ* synchrotron experiments, and optimized sample preparation for impedance spectroscopy. Joshua A. Kurzman executed *in situ* synchrotron experiments. Maxwell C. Schulze optimized and executed impedance spectroscopy measurements. Amy L. Prieto provided helpful discussion and supervised the impedance studies. James R. Neilson supervised the project.

FeS and FeSe in Ph_3P flux reactions: Elemental Fe powder was purified via heating to 980 °C in an evacuated ($<$ 10 mtorr) amorphous silica ampoule for several hours. Surface oxidation of the iron was driven off to form silicates on the glass surface and the resulting iron powder had a bright metallic luster. Selenium shot was purified by sealing in an amorphous silica ampoule, heating above the melting point, and slowly cooling through the transition temperature. The resulting ingot was sanded to remove any noticeable oxide layer. Sulfur was purified via vapor transport; after sealing under vacuum in a tube approx. 18 inches in length, the sulfur charge was placed in a three-zone tube furnace at 550 °C. The two other zones were set at 400 °C and the recrystallization setup was left for several hours. After cooling, all the sulfur was found at the cold end of the tube, with black, carbonaceous impurities left in the hot end.

The elemental reactants were ground homogeneously and mixed with a specified amount of Ph_3P. The entire mixture was transferred to a silica ampoule, heated at 10 °C to 325 °C, and allowed to dwell for 12–24 hours. The reactions were shaken occasionally once at the reaction temperature to further promote mixing and diffusion in the then-liquid media. The reactions were then either quenched in ice water, removed to ambient atmosphere, or controllably cooled at 10 °C per minute.

$NiCl_2 + A_2S_2$, A = Na, K: The reactants Na_2S_2, K_2S_2, Na_2Se_2, and K_2Se_2 were prepared from the elements in an argon-filled glove box. The alkali metal and chalcogen were physically separated, each in a separate alumina crucible, and placed in a 14 mm i.d. silica tube, evacuated to $<$10 mtorr and sealed. The reactions were then heated at 1 °C per minute to 400 °C and held for 24 hours. The products were subsequently collected in an argon-filled glove box, ground, pelleted, and resealed under vacuum, and annealed at

400 °C for 24 hours. The resultant yellow (for Na_2S_2 and K_2S_2) or red-brown (for Na_2Se_2 and K_2Se_2) powders were stored in a dry, argon filled glove box.

The reaction mixtures of $NiCl_2 + A_2S_2$, A = Na, K were combined in 1:1 stoichiometric ratios and ground homogeneously. They were then evacuated and sealed in extruded silica capillaries (o.d. = 0.7 mm). For air-exposed reactions, the reaction mixtures were ground homogeneously in an Ar-filled glove box, then removed to a fume hood in ambient atmosphere. The reaction mixtures all begin to darken in appearance within seconds and are completely black after ca. 60 seconds of grinding. Exact humidity levels were not controlled, but were generally $\leq$ 50% as monitored by an ambient humidity sensor. The reactant mixtures do not deliquesce. The reaction mixtures were then evacuated to $<$10 mtorr and sealed in extruded silica capillaries. *In situ* synchrotron X-ray diffraction data was collected using beamline 17-BM-B (λ = 0.75009 Å) at the Advanced Photon Source at Argonne National Laboratory. The samples were heated at 3 °C min^{-1} from room temperature to 400 °C using a resistive heater as previously described.[100] Diffraction data were continuously collected using a 2048$\times$2048 pixel Perkin-Elmer 2D plate detector in 30 second increments, each pattern consisting of three 10 s subframes, while the sample was continuously rotated by 5° along its long axis. The 2D diffraction patterns were then radially integrated using GSAS-II.[101] A LaB_6 standard (NIST 660b) was used to calibrate the sample-to-detector distance, which was nominally 300 mm.

Impedance spectroscopy was collected using a Gamry Reference 3000 potentiostat. Temperature was controlled using a Cincinnati Sub-Zero MicroClimate atmospheric chamber. High density ingots of Na_2S_2 and K_2S_2 were prepared for impedance spectroscopy by placing either "$Na_{50}S_{56}$" (that is, $Na_2S_2 + 0.24\,S$) or K_2S_2 powders in carbon-coated 4 mm

i.d. silica ampoules and sealed under vacuum. The tubes were placed upright in a box furnace and heated at 5 °C per minute to 550 °C and allowed to dwell for 6 hours. The reactions were then cooled at a rate of 15 °C per hour to either 145 °C (for Na_2S_2) or 260 °C (for K_2S_2). The products were collected in a dry, argon-filled glove box. The top of the Na_2S_2 ingot was cut off to remove any sulfur-rich material. The dense, yellow-brown ingots were sanded flat on either side and painted with conductive carbon paste, which was allowed to cure overnight. The ingots were then placed in Swagelok cells with stainless steel current collectors as the contacts.

Laboratory powder X-ray diffraction patterns were collected with a Bruker D8 Discover X-ray diffractometer using CuKα radiation and a Lynxeye XE-T position-sensitive detector. Differential scanning calorimetry data were collected on a TA Instruments DSC 2500 on homogeneously ground reaction mixtures (approx. 10 mg) hermetically sealed in aluminum cans. The temperature ramp was 3 °C min^{-1} to replicate the reaction collected *in situ*.

6.3. Using Molecules to Control Solid State Material Formation

Perhaps the most advanced application of kinetic control presented in this work is the use of a small amount of triphenylphosphine to the metathesis reaction $CuCl_2 + Na_2Se_2$ to selectively form pyrite $CuSe_2$ before the thermodynamically stable marcasite polymorph. It was determined that the Lewis basicity of the phosphine was necessary to form a triphenylphosphine selenide adduct which acted as an atom transfer agent.

We thus sought to extend the utility of triphenylphosphine as an atom transfer agent to different reactions, and motivated by the various uses of tertiary phosphines in the synthesis of transition metal chalcogenide nanomaterials,[154] instituted it as a flux for elemental solid state reactions. Triphenylphopshine melts at 80 °C and does not boil until 380 °C, affording a large stability window in which reactions may occur. It will also readily form adducts of sulfur and selenium, and is thus well suited to activate the solid reactants and promote reactivity.

Here, the phase-selective syntheses of tetragonal, superconducting FeSe as well as stoichiometric troilite-structured FeS, from the elements in a triphenylphosphine flux is presented. Both are the thermodynamically stable phases at low temperature, and are otherwise difficult to produce from the direct combination of the elements.

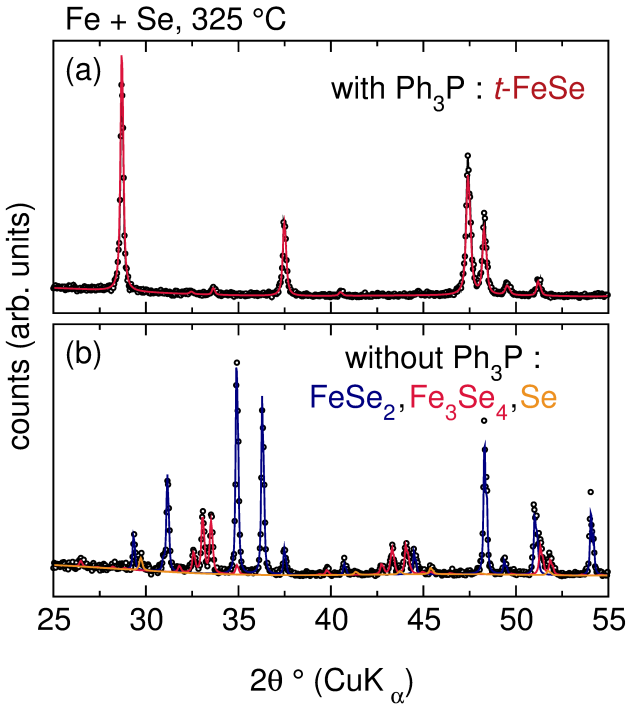

Figure 6.1: Phase-decomposed Rietveld refinements of the products of the reaction Fe + Se (a) with and (b) without the triphenylphosphine flux. It is clear that the flux promotes the phase selection of the superconducting β-FeSe phase, while the neat reaction yields a mixture of phases.

The synthesis of tetragonal FeSe via a triphenylphosphine flux was achieved by sealing approx. 100 mg of elemental Se with approx. 70.7 mg of Fe and approx. 333 mg of Ph_3P in a 10 mm i.d. silica tube under vacuum and heating to 325 °C at 10 °C per minute. After allowing the reaction mixture to dwell at temperature for 24 hours, the furnace was cooled at 10 °C per hour to room temperature. The resultant mixture yielded a black solid after repeated washes in benzene to remove the excess triphenylphosphine. A ferromagnetic impurity (likely small amounts of unreacted elemental iron) was magnetically separated from the FeSe.

Powder diffraction of the products of reaction Fe + Se at 325 °C in a flux of Ph_3P after wash with benzene is shown in Figure 6.1a. The data indicate the formation of a single phase, tetragonal FeSe. When executed in the absence of the triphenylphopshine flux under the same heating conditions, the elemental reaction yields $FeSe_2$, Fe_3Se_4, and elemental selenium (Figure 6.1b). It is likely that Fe metal was also left in the reaction mixture but not detected by PXRD because of its ductility and resistance against powdering.

When the reaction Fe + S was attempted in a phosphine flux, the stoichiometric troilite phase of FeS was produced (Figure 6.2). This phase is only stable below 150 °C, above which the material disproportionates to a range of iron-poor phases (Figure 6.3a). This phase is not easily accessible from traditional solid-state reactions, instead reqiuring the application of non-hydrolytic sol-gel methods[163] or can be found in nature.[164]

In an effort to understand the reason why these reactions were successful, a number of control reactions were explored. Firstly, the FeSe product of the flux reaction is sensitive to the cooling rate. Tetragonal FeSe alone is observed if the reaction is cooled at 10 °C per hour from the reaction temperature to room temperature. If the reaction is quenched or

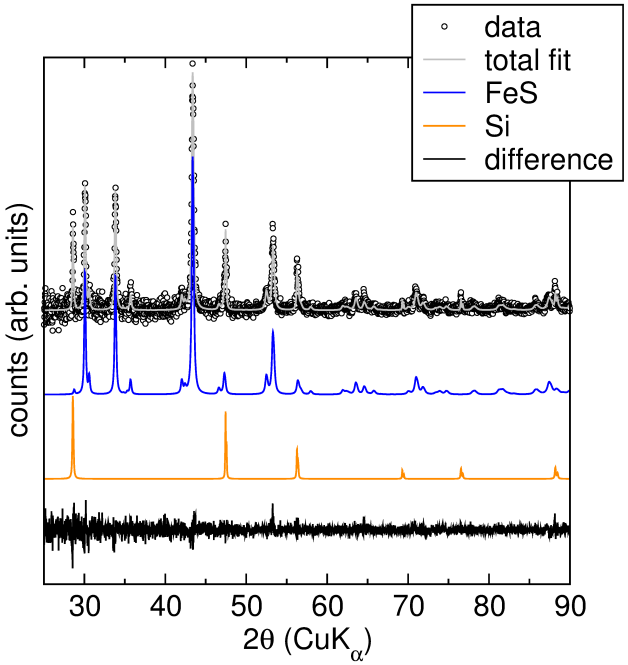

Figure 6.2: Rietveld refinement of the PXRD data of the products of the reaction Fe+S in a triphenylphosphine flux. The FeS troilite phase is the lone product. Elemental silicon was included as an internal standard for PXRD.

allowed to ambiently cool, both the tetragonal and hexagonal phases of FeSe are detected in the products. When quenched, there is significantly more of the hexagonal polymorph than the tetragonal. This result is somewhat surprising because the reaction remains below $T = 457$ °C, which is the temperature at which the hexagonal polymorph of FeSe becomes thermodynamically stable (Figure 6.3b).

Additionally, the tetragonal FeSe product phase seems to be uniquely *insensitive* to the input composition. Even if up to two equivalents of selenium are reacted with a single equivalent of iron, the only crystalline product found after washing with benzene is tetragonal FeSe. The product always appears to have the optimal *c*:*a* ratio for maximum T_c. This insensitivity is a striking feature of this synthetic method, especially considering the previous challenges surrounding the sensitivity of FeSe to stoichiometry derived from traditional solid state reactions.[125] The product seems generally insensitive to amount of Ph_3P

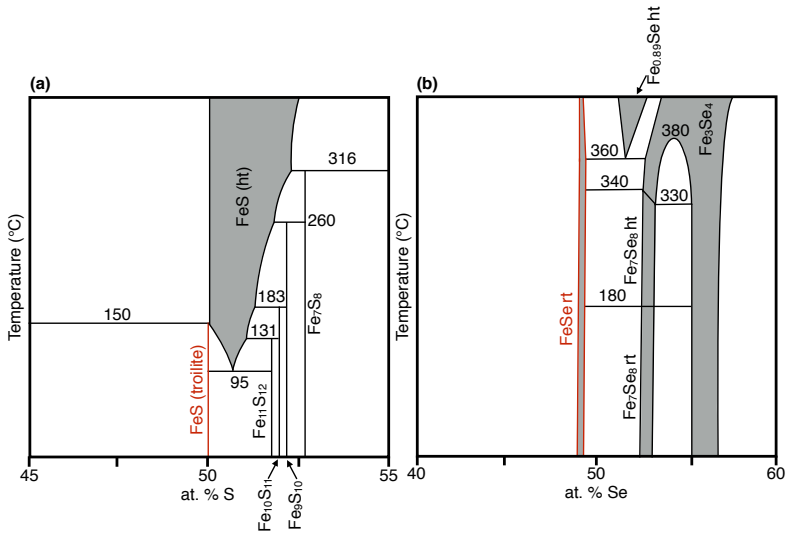

Figure 6.3: Partial phase diagrams of (a) Fe–S and (b) Fe-Se. The products of the reaction of iron with the respective chalcogenide in a triphenylphosphine flux yields stoichiometric FeS or FeSe in the structure stable at low temperatures, highlighted in red. Phase diagrams are adapted from Adapted from reference 10 and reference 165, respectively.

flux used as well, though less ferromagnetic impurity is observed as the ratio of Ph_3P to Se increases.

It should also be noted that in the reactions using the triphenylphosphine flux, no gaseous chalcogen was observed, either directly as gas in the tube while hot, or indirectly, by the deposition of a elemental chalcogen layer towards the cooler end of the tube. It is possible that the phosphine flux spatially sequesters the chalcogen reactant, which in turn makes it more available to corrode the iron. When no triphenylphosphine flux is used, there is clearly gas evolved in the tube as the chalcogen reactants volatilize, and a large amount of chalcogen can be observed separated from the metallic reactant once the reactions have cooled.

The reactivity of phosphines with chalcogenides has been well-studied; the Lewis-basic phosphine readily forms adducts with the chalcogenide (i.e., $R_3\mathrm{P} + Q \longrightarrow R_3\mathrm{P}Q$). This mechanism has been widely applied in the preparation of transition metal chalcogenide

nanoparticles, either to partially extract the chalcogen from nanoparticles,[144] or serve as chalcogenide transfer agents with tunable physical properties and reactivity.[145,162] We recently presented the utility of triphenylphosphine as an atom transfer agent to promote the polymorph-selective preparation of cubic $CuSe_2$, by adding the triphenylphosphine to the solid state metathesis reaction $CuCl_2 + Na_2Se_2$ in small amounts.[99]

In this case, it appears that these features are working in tandem to facilitate the reaction $Fe + Q$. The equilibrium $Se + Ph_3P \rightleftharpoons Ph_3PSe$ is influenced by the driving force to form FeSe, consuming the Ph_3PSe and replenishing the Ph_3P. However, there is relatively little driving force to produce $FeSe_2$ from FeSe (ΔH_f(FeSe)=37 kJ mol^{-1} atom^{-1}, ΔH_f($FeSe_2$)=41 kJ mol^{-1} atom^{-1}).[166] The thermodynamic favorability of the FeSe+Ph_3PSe vs. $FeSe_2 + Ph_3P$ is further supported by a report that utilizes trioctylphosphine to transform $FeSe_2$ and Fe_3Se_4 nanoparticles into tetragonal FeSe, which suggests a mechanism depending on selenium uptake by the phosphine.[144]

The open question remains: why are the low-temperature polymorphs of FeSe and FeS produced, even when the temperature at which the reactions are executed does not correspond to the range at which the products are thermodynamically stable? This is especially clear in the case of the quenched reaction that produces hexagonal FeSe. It is possible that the thermodynamic ground state is altered and allows the kinetic trapping of the various phases.[1] If indeed the thermodynamic ground state is being altered, it is possible that under the right conditions it will be possible to form metastable materials, such as the recently discovered tetragonal FeS, which is isostructural to tetragonal FeSe, and is a superconductor.[167,168]

In summary, we have presented a new method for the preparation of phase-pure, superconducting tetragonal FeSe, as well as the low temperature troilite phase of FeS. The syntheses depend on the use of triphenylphosphine as a flux, which likely functions as a chalcogen shuttle as well as solvent to promote corrosion of the iron and diffusion throughout the reaction simultaneously. The apparent insensitivity to input composition and phase dependence on cooling rate suggests that the triphenylphosphine flux promotes a thermodynamic equilibrium in which the tetragonal FeSe or troilite FeS is the thermodynamically stable phase, rather than any other polymorph or stoichiometry. This new synthetic method has the potential to form a range of desired functional materials, as small organic molecular fluxes can be tuned to react with a range of transition metal and main group elemental constituents.

6.4. Expanded Considerations for Precursor Selection

Returning to the reactivity of solid state metathesis reactions, a number of factors should also be explored to maximize the opportunities for kinetic control. While we previously have explored the variation of reaction pathway when the targeted functional material (i.e., the transition metal chalcogenide) is changed, the possibility to tune the reaction pathway by altering the spectator ions has not. Preliminary results in this light are promising, which will be outlined below.

Chapter three discusses the *in situ* PXRD data of the reaction $NiCl_2 + Na_2S_2$ between room temperature and 400 °C. The reaction first slowly forms NaCl as well as Na_2S_4 at ca. 100 °C before reaching a highly reactive period at ca. 230 °C. In this reactive zone, a num-

ber of intermediates are observed, including Na_2S_5, Ni_3S_2, and both known polymorphs of NiS. These intermediates are surprisingly quite crystalline in this reactive zone before NiS_2 formation, as indicated by relatively narrow FWHM of Bragg features. Once NiS_2 forms the intermediates disappear rapidly and no further reactivity is observed.

If instead K_2S_2 is used as a sulfur source for the reaction, the reaction pathway is clearly altered. KCl does not form until ca. 210 °C, and does so rapidly. No K-S intermediate phases are observed. Ni_3S_2 is not observed either, and NiS_2 forms shortly after KCl along with both polymorphs of NiS. The monosulfides are quickly consumed, and do not form as large crystalline domains as in the case of the reaction $Na_2S_2 + NiCl_2$. Interestingly, the ternary phase $K_2Ni_3S_4$ forms *after* NiS_2, and is observed to slowly grow in intensity until the end of the *in situ* experiment.

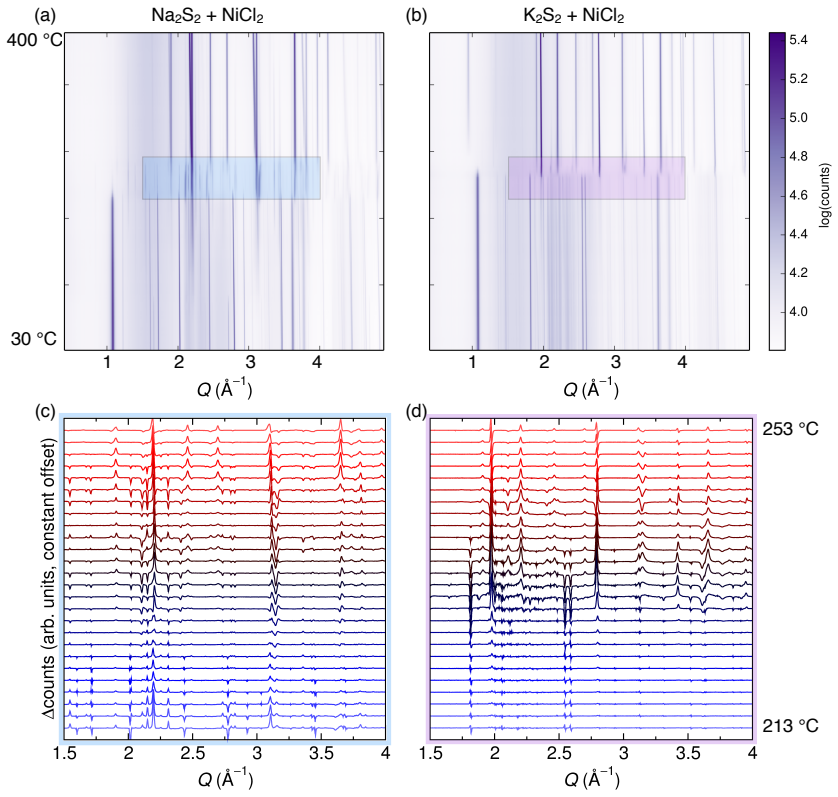

Figure 6.4: *In situ* powder X-ray diffraction of the reactions (a) $Na_2S_2 + NiCl_2$ and (b)$K_2S_2 + NiCl_2$. Difference powder X-ray diffraction of the highlighted regions of each are shown in (c) and (d), respectively.

Reactants, intermediates, and products are all present in the potassium-containing reaction simultaneously, indicating much faster reaction kinetics once the critical reaction temperature is reached, despite the delayed formation of KCl compared to NaCl. The delayed formation of KCl may be attributed to the slightly higher stability of K_2S_2 ($\Delta H_f = -447.5$ kJ mol^{-1}) compared to Na_2S_2 ($\Delta H_f = -398.0$ kJ mol^{-1}), as we have shown previously for the differing metal chloride salts, though the total enthalpies of both reactions are very comparable.

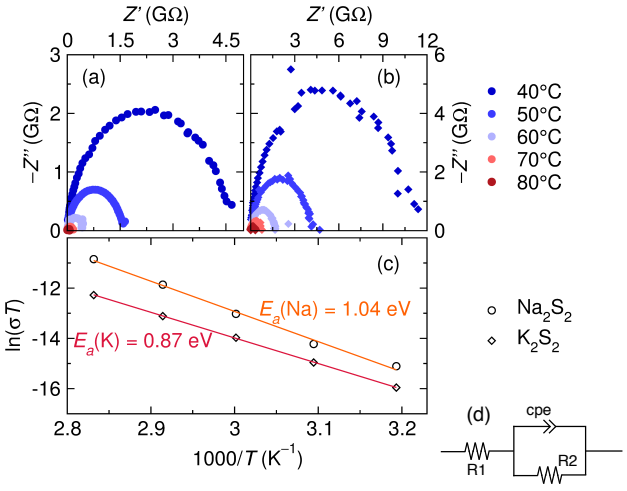

Figure 6.5: Nyquist plots of the complex impedance of (a) Na_2S_2 and (b) K_2S_2 between 40 °C and 80 °C. The Arrhenius relationship of inverse temperature and ionic conductivity is shown in (c), derived from fits to the data shown in (a) and (b). The equivalent circuit used to fit the data is shown in (d), where R1 corresponds to the contact resistance, R2 corresponds to the ionic resistance, and the constant phase element (cpe) accounts for the phase shift.

To further elucidate the origin of the varied reactivity between Na_2S_2 and K_2S_2, electrochemical impedance spectroscopy was used to study the ion mobility of each material (Figure 6.5). While the ionic resistivity is high for both materials (ca. 10s of GΩ at room temperature), it is approx. half as resistive in the sodium sulfide than the potassium sulfide. Measuring the impedance as a function of temperature allows the extraction of an Arrhenius relationship to determine activation energy for ionic conduction (Figure 6.5c).

The Na_2S_2 has an activation energy of 1.04 eV and the K_2S_2 has a slightly lower activation energy of 0.87 eV.

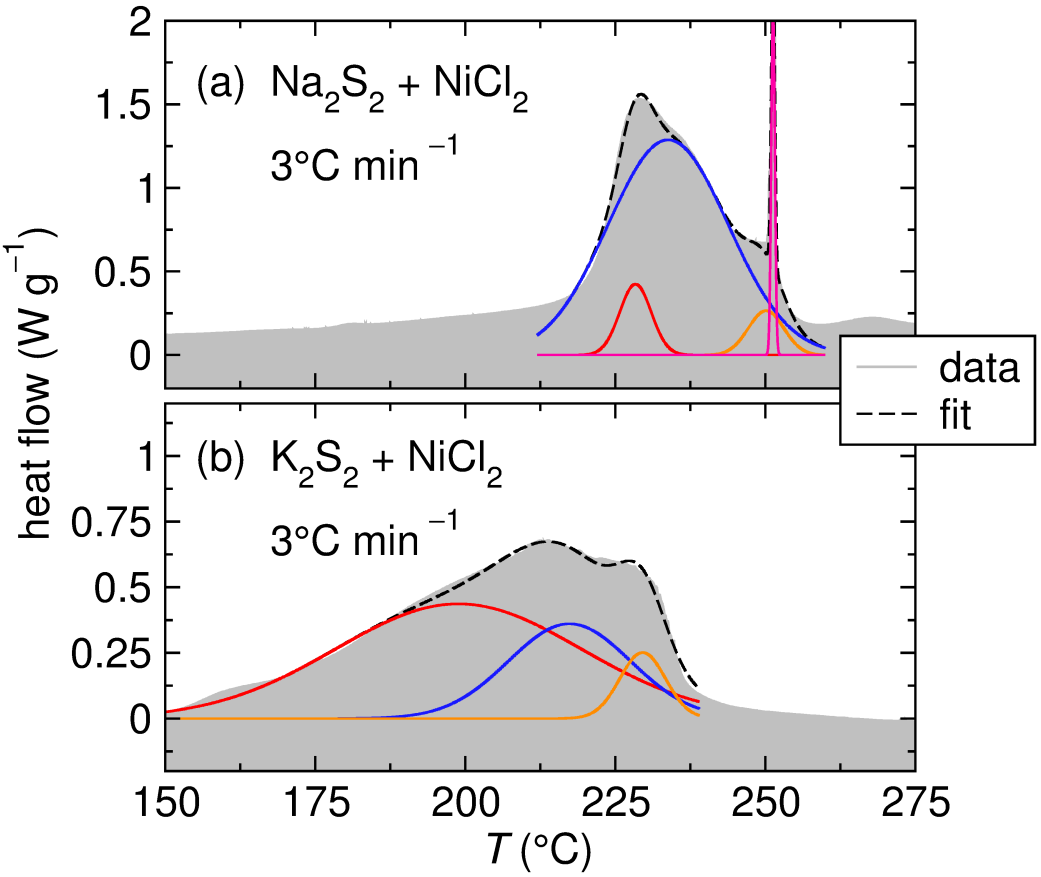

Figure 6.6: DSC curves collected at different scan rates (filled) with corresponding Gaussian fits (dashed lines). The Na-containing reaction (a) are well-described using four Gaussian functions, while the K-containing reaction (b) are fit using three.

Differential scanning calorimetry was used to understand the differences in reactivity between the sulfur sources, and extract kinetic information regarding the reaction pathways (Figure 6.6). In both cases, there are multiple broad exotherms present. Studying the reactions with DSC as a function of scan rate can be used to extract kinetic information in a variety of ways. In general, the exotherms shift more quickly as function of temperature in the Na-containing reaction than the K-containing reaction, again suggesting a higher activation energy for the sodium if an Arrhenius relationship is extracted.

Interestingly, while in the case of $Na_2S_2 + NiCl_2$ the exotherms align approximately with the reactive zone observed in PXRD, the onset temperature of the reaction $K_2S_2 + NiCl_2$ appears *much earlier* via DSC, while no major changes are observed in the PXRD. This suggests that there are microscopic differences occurring in the reactants before bulk reactivity, and that do not readily change the crystalline components of the reactants, or that there is some difference in the reactants (e.g., particles size) that was unaccounted for in these experiments.

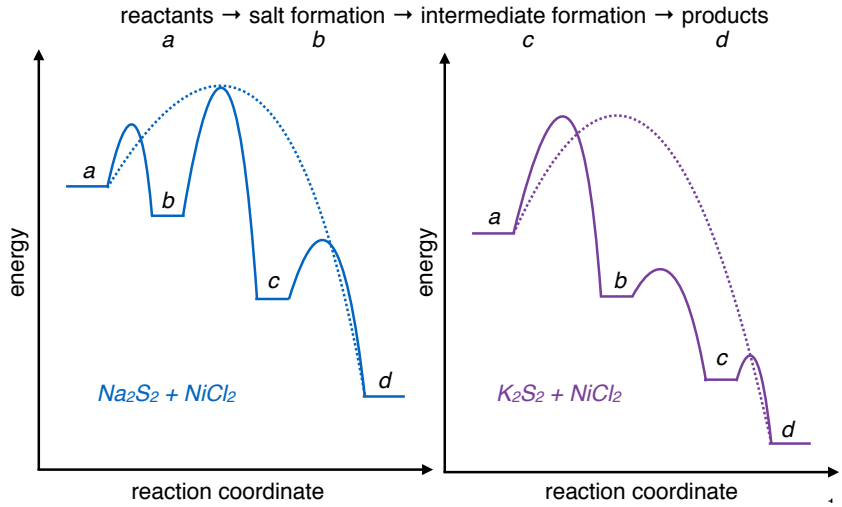

Figure 6.7: Proposed reaction pathways with distinct rate limiting steps of the two reactions.

From this ensemble of measurements, two different reaction pathways can be hypothesized depending on the use of either Na_2S_2 or K_2S_2, which are shown in Figure 6.7. In both cases, the first step is the formation of the alkali chloride salt. This step is followed by the formation of various other intermediates, including Na_2S_4 and Na_2S_5 in the Na-containing reaction, and various Ni-S phases in both reactions. This step is followed by NiS_2 formation and growth. In the Na-containing reaction, the salt formation occurs at relatively low temperature (ca. 100 °C), suggesting that there is only a small energetic barrier. The formation of KCl does not occur until approximately 200 °C, indicating a larger barrier for

this step comparatively. Alternatively, the intermediate formation proceeds much later in the case of the Na-containing reaction, whereas it occurs quickly after KCl formation. NiS_2 formation follows quickly in both cases. These data suggest that intermediate formation is the rate determining step in the Na-containing reaction, while salt formation is the rate determining step in the K-containing reaction. This is likely due to the much lower mobility of the potassium in the K_2S_2 precursor, evidenced by the electrochemical impedance spectroscopy.

To test the resulting hypotheses regarding the pathway control of these solid state reactions, we sought to prepare solid-solution mixtures of NiSSe. The end members (that is, NiS_2 and $NiSe_2$) are isostructural and have been shown to form solid solutions previously. The guiding principles for this proof-of-concept were that (a) sodium-containing precursors will have enhanced reactivity at low temperatures and promote mixing and (b) potassium-containing precursors will react more slowly, perhaps disallowing full chalcogen mixing and solid solution formation.

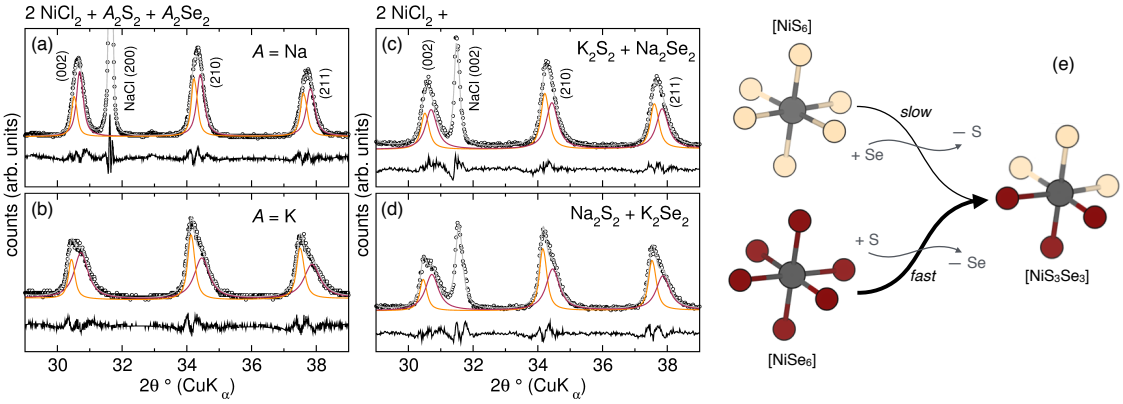

Figure 6.8: (a–d) PXRD patterns (circles) and corresponding Rietveld refinements (grey lines) of the products of the reactions $2\,NiCl_2 + A_2S_2 + A_2Se_2$ (A = Na, K). In all cases, there is clearly splitting of the NiSSe reflections, indicating the formation of incomplete solid-solution formation. The patterns in (a) and (d) are less phase separated than in (b) and (c). These observations are described by the scheme in (e), whereby it is easier to displace selenium than sulfur from the coordination sphere around a nickel center.

The reactions $2\,NiCl_2 + A_2S_2 + A_2Se_2$ (A = Na, K) were executed under air-free conditions at 400 °C for 24 hours. PXRD patterns of the products are shown in figure 6.8a and figure 6.8b. Both reactions achieve the formation of mixed S/Se phases, but the sodium-containing reaction yields two more similar NiSSe phases while the potassium-containing reaction forms two more distinct phases, as evidenced by the splitting of the NiSSe reflections. This is in good agreement with our reaction design principles that sodium-containing reactants can indeed provide the reactivity needed to increase mixing and promote solid-solution formation.

If instead both alkali ions are present in the reactions, via the reactions of either $2\,NiCl_2 + K_2S_2 + Na_2Se_2$ (figure 6.8c) or $2\,NiCl_2 + Na_2S_2 + K_2Se_2$ (figure 6.8d), the NiSSe product phase can again be altered. In the case of the sodium sulfide-potassium selenide case, two NiSSe phases are required to fit the data, whereas less NiSSe phase separation is observed in the potassium sulfide-sodium selenide case. This is due to the low-temperature reactivity of the sodium precursors. When Ni-S intermediates form, it is harder to then mix selenium from a less-reactive potassium source due to the increased strength of Ni-S bonds relative to Ni-Se bonds. Thus, phase separation occurs in the case of the reaction $2\,NiCl_2 + Na_2S_2 + K_2Se_2$. If instead the low temperature reactivity of the sodium precursor forms the relatively weaker Ni-Se bonds, the potassium sulfide reaction that occurs at higher temperature allows displacement of the Se and thus greater S/Se mixing in the homogenous NiSSe product. These concepts are illustrated in figure 6.8e.

These initial results indicate the profound impact that precursor selection may have on reaction pathway, even when substituting what would appear to be a spectator ion. Determining a broader understanding of what each component of a solid state reaction

can have on the overall reaction pathway will be instrumental in deriving design rules for new reaction pathways, and in turn new materials.

6.5. Advancing *in situ* Methods to Develop Kinetic Control

The previous example highlights the utility of the combination of a number of analytical assays to better understand the differences in reactivity; no single measurement provides the entire story. However, it is not without its shortcomings: the exotherm observed at low temperatures and over a broad temperature range (150 – 200 °C) via DSC in the reaction $K_2S_2 + NiCl_2$ does not correspond to any changes in the bulk crystalline structure of the reaction mixture, evidenced by PXRD. How can one determine the origin of this exotherm, and more generally, what methods can be used to account for microscopic changes in a solid state reaction mixture? However, the possibility that some extrinsic parameter such as particle size must also be considered. For example, if the K_2S_2 is made up of larger grains than the Na_2S_2, there is less bulk interface between the potassium sulfide and nickel chloride, and thus less available reactive material at a given temperature.

Pair distribution function analysis of *in situ* total scattering measurements may provide information on the local structural changes as a function of temperature. We have previously used this technique to analyze the nucleation and growth of a crystalline phase from an amorphous phase upon heating[95,98] but have yet to investigate complete crystalline-to-crystalline chemical transformations due to the added complication of the multiple crystalline components present. Analysis of the local structure may however provide a greater understanding of microscopic changes before bulk crystallographic changes occur. Addi-

tionally, the use of spectroscopic techniques, such as infrared or Raman spectroscopy, may prove valuable in understanding how the reactants begin to interact at the local, interfacial level.

6.6. Applying Kinetic Control Design Rules to Real Systems

Moving beyond the realm of fundamental solid state reactivity, application of similar studies to functional, dynamic, solid state chemical systems is the next step. Applying advanced *in situ* analytical methods to gain greater understanding of the origins of performance of specific materials and devices will be extremely informative towards the design of next-generation materials.

The key will be identifying appropriate dynamic systems in which understanding their kinetic mechanisms *in operando* will inform the principles upon which they operate. For example, the understanding of kinetic pathways of battery electrodes upon cycling provides a wealth of information regarding their performance. Even with relatively simple insertion electrodes, such as $LiFePO_4$, observation of a cycling rate-dependent mechanism, where at higher rates a single-phase, $Li_{1-x}FePO_4$-forming mechanism occurs rather than the classical, thermodynamically-driven two-phase mechanism aids in explanation of the high rate capability of the material.[51] This example highlights that even in simple compounds, *in situ* kinetic studies are worthwhile. As more battery technologies are being shifted to focus on conversion-based electrodes to maximize gravimetric capacity, the mechanism(s) controlling the transformation will become more complex (i.e., there will not be any structural similarities between a charged and discharged electrode). Studying these transfor-

mations, for example the lithiation of iron sulfide FeS_2, $4\,Li + FeS_2 \longrightarrow Fe + 2\,Li_2S$, with advanced analysis techniques and importantly under various kinetic conditions will provide the ability to design new battery materials and frameworks from which to maximize device performance, capacity, and efficiency.

Bibliography

[1] Martinolich, A. J.; Neilson, J. R. Toward Reaction-by-Design: Achieving Kinetic Control of Solid State Chemistry with Metathesis. *Chem. Mater.* **2017**, *29*, 479–489.

[2] Kanatzidis, M. G.; Poeppelmeier, K. R. Report from the third workshop on future directions of solid-state chemistry: The status of solid-state chemistry and its impact in the physical sciences. *Prog. Solid State Chem.* **2008**, *36*, 1 – 133.

[3] Soderholm, L.; Mitchell, J. Perspective: Toward "Synthesis by Design": Exploring Atomic Correlations During Inorganic Materials Synthesis. *APL Mater.* **2016**, *4*, 053212.

[4] DiSalvo, F. J. Solid-State Chemistry: A Rediscovered Chemical Frontier. *Science* **1990**, *247*, 649–655.

[5] Stein, A.; Keller, S. W.; Mallouk, T. E. Turning Down the Heat: Design and Mechanism in Solid-State Synthesis. *Science* **1993**, *259*, 1558–1564.

[6] Walsh, A. Inorganic Materials: The Quest for New Functionality. *Nat. Chem.* **2015**, *7*, 274–275.

[7] Franzen, H. In *Binary Alloy Phase Diagrams*, ii ed.; Massalski, T., Ed.; 1990; Vol. 3; pp 2593–2597.

[8] Chakrabarti, D.; Laughlin, D. The Cu-S (copper-sulfur) system. *Bull. Alloy Phase Diagr.* **1983**, *4*, 254–271.

[9] Sharma, K.; Chang, Y. The S-Zn (sulfur-zinc) system. *J. Phase Equilib.* **1996**, *17*, 261–266.

[10] Waldner, P.; Pelton, A. Thermodynamic modeling of the Fe-S system. *J. Phase Equilib. Diffus.* **2005**, *26*, 23–38.

[11] Kuznetsov, V.; Sokolova, M.; Palkina, K.; Popova, Z. The cobalt-sulfur system. *Inorg. Mater.* **1965**, *1*, 617–632.

[12] Waldner, P.; Pelton, A. D. Thermodynamic modeling of the Ni–S system. *Z. Metallkd.* **2004**, *95*, 672–681.

[13] Buckeridge, J.; Butler, K. T.; Catlow, C. R. A.; Logsdail, A. J.; Scanlon, D. O.; Shevlin, S. A.; Woodley, S. M.; Sokol, A. A.; Walsh, A. Polymorph Engineering of TiO_2: Demonstrating How Absolute Reference Potentials Are Determined by Local Coordination. *Chem. Mater.* **2015**, *27*, 3844–3851.

[14] Bither, T.; Prewitt, C.; Gillson, J.; Bierstedt, P.; Flippen, R.; Young, H. New transition metal dichalcogenides formed at high pressure. *Solid State Commun.* **1966**, *4*, 533 – 535.

[15] Bither, T. A.; Bouchard, R. J.; Cloud, W. H.; Donohue, P. C.; Siemons, W. J. Transition Metal Pyrite Dichalcogenides. High-Pressure Synthesis and Correlation of Properties. *Inorg. Chem.* **1968**, *7*, 2208–2220.

[16] Ranade, M. R.; Navrotsky, A.; Zhang, H. Z.; Banfield, J. F.; Elder, S. H.; Zaban, A.; Borse, P. H.; Kulkarni, S. K.; Doran, G. S.; Whitfield, H. J. Energetics of Nanocrystalline TiO_2. *Proc. Natl. Acad. Sci. USA* **2002**, *99*, 6476–6481.

[17] Murphy, D. W.; Cros, C.; DiSalvo, F. J.; Waszczak, J. V. Preparation and properties of Li_xVS_2 ($0 \leq x \leq 1$). *Inorg. Chem.* **1977**, *16*, 3027–3031.

[18] Massalski, T. B.; Okamoto, H.; Subramanian, P.; Kacprzak, L. Binary alloy phase diagrams. vol. 3. *ASM International, 1990,* **1990**, 1485.

[19] Neilson, J. R.; McQueen, T. M. Bonding, Ion Mobility, and Rate-Limiting Steps in Deintercalation Reactions with $ThCr_2Si_2$-type KNi_2Se_2. *J. Am. Chem. Soc.* **2012**, *134*, 7750–7757.

[20] Sanjaya Ranmohotti, K.; Josepha, E.; Choi, J.; Zhang, J.; Wiley, J. B. Topochemical Manipulation of Perovskites: Low-Temperature Reaction Strategies for Directing Structure and Properties. *Adv. Mater.* **2011**, *23*, 442–460.

[21] Schaak, R. E.; Mallouk, T. E. Perovskites by Design: A Toolbox of Solid-State Reactions. *Chem. Mater.* **2002**, *14*, 1455–1471.

[22] Zhou, X.; Eckberg, C.; Wilfong, B.; Liou, S.-C.; Vivanco, H. K.; Paglione, J.; Rodriguez, E. E. Superconductivity and Magnetism in Iron Sulfides Intercalated by Metal Hydroxides. *Chem. Sci.* **2017**, *8*, 3781–3788.

[23] Zhou, X.; Wilfong, B.; Vivanco, H.; Paglione, J.; Brown, C. M.; Rodriguez, E. E. Metastable Layered Cobalt Chalcogenides from Topochemical Deintercalation. *J. Am. Chem. Soc.* **2016**, *138*, 16432–16442.

[24] Rouxel, J. Anion–Cation Redox Competition and the Formation of New Compounds in Highly Covalent Systems. *Chem. Eur. J.* **1996**, *2*, 1053–1059.

[25] Sathiya, M.; Rousse, G.; Ramesha, K.; Laisa, C. P.; Vezin, H.; Sougrati, M. T.; Doublet, M.-L.; Foix, D.; Gonbeau, D.; Walker, W.; Prakash, A. S.; Ben Hassine, M.; Dupont, L.; Tarascon, J.-M. Reversible Anionic Redox Chemistry in High-Capacity Layered-Oxide Electrodes. *Nat. Mater.* **2013**, *12*, 827–835.

[26] Hayward, M.; Green, M.; Rosseinsky, M.; Sloan, J. Sodium Hydride as a Powerful Reducing Agent for Topotactic Oxide Deintercalation: Synthesis and Characterization of the Nickel (I) Oxide $LaNiO_2$. *J. Am. Chem. Soc.* **1999**, *121*, 8843–8854.

[27] Hayward, M.; Rosseinsky, M. Anion Vacancy Distribution and Magnetism in the New Reduced Layered Co (II)/Co (I) phase $LaSrCoO_{3.5-x}$. *Chem. Mater.* **2000**, *12*, 2182–2195.

[28] Hayward, M.; Cussen, E.; Claridge, J.; Bieringer, M.; Rosseinsky, M.; Kiely, C.; Blundell, S.; Marshall, I.; Pratt, F. The Hydride Anion in an Extended Transition Metal Oxide Array: $LaSrCoO_3H_{0.7}$. *Science* **2002**, *295*, 1882–1884.

[29] Kobayashi, Y. et al. An Oxyhydride of $BaTiO_3$ Exhibiting Hydride Exchange and Electronic Conductivity. *Nat. Mater.* **2012**, *11*, 507–511.

[30] Yajima, T.; Takeiri, F.; Aidzu, K.; Akamatsu, H.; Fujita, K.; Yoshimune, W.; Ohkura, M.; Lei, S.; Gopalan, V.; Tanaka, K.; Brown, C. M.; Green, M. A.; Yamamoto, T.; Kobayashi, Y.; Kageyama, H. A Labile Hydride Strategy for the Synthesis of Heavily Nitridized $BaTiO_3$. *Nat. Chem.* **2015**, *7*, 1017–1023.

[31] Masuda, N.; Kobayashi, Y.; Hernandez, O.; Bataille, T.; Paofai, S.; Suzuki, H.; Ritter, C.; Naoki, I.; Noda, Y.; Takegoshi, K.; Tassel, C.; Yamamoto, T.; Kageyama, H.

Hydride in $BaTiO_{2.5}H_{0.5}$: A Labile Ligand in Solid State Chemistry. *J. Am. Chem. Soc.* **2015**, *137*, 15315–15321.

[32] Mikita, R.; Aharen, T.; Yamamoto, T.; Takeiri, F.; Ya, T.; Yoshimune, W.; Fujita, K.; Yoshida, S.; Tanaka, K.; Batuk, D.; Abakumov, A. M.; Brown, C. M.; Kobayashi, Y.; Kageyama, H. Topochemical Nitridation with Anion Vacancy-Assisted N^{3-}/O^{2-} Exchange. *J. Am. Chem. Soc.* **2016**, *138*, 3211–3217.

[33] Zaikina, J. V.; Batuk, M.; Abakumov, A. M.; Navrotsky, A.; Kauzlarich, S. M. Facile Synthesis of $Ba_{1-x}K_xFe_2As_2$ Superconductors via Hydride Route. *J. Am. Chem. Soc.* **2014**, *136*, 16932–16939.

[34] Sunshine, S. A.; Kang, D.; Ibers, J. A. A New Low-Temperature Route to Metal Polychalcogenides: Solid-State Synthesis of Potassium Titanium Sulfide ($K_4Ti_3S_{14}$), a Novel One-Dimensional Compound. *J. Am. Chem. Soc.* **1987**, *109*, 6202–6204.

[35] Lu, Y.-J.; Ibers, J. A. Synthesis of the Quaternary One-Dimensional Triple-Chain Materials $K_3Cu_3M_2Q_8$ (M= Nb, Ta; Q= S, Se): The structure of $K_3Cu_3Nb_2S_8$. *J. Solid State Chem.* **1992**, *98*, 312–317.

[36] Mansuetto, M. F.; Keane, P. M.; Ibers, J. A. Synthesis and Structures of the New Group IV Chalcogenides $NaCuTiS_3$ and $NaCuZrQ_3$ (Q= S, Se, Te). *J. Solid State Chem.* **1993**, *105*, 580–587.

[37] Kanatzidis, M. G.; Park, Y. Polychalcogenide Synthesis in Molten Salts. Novel One-Dimensional Compounds in the Potassium-Copper-Sulfur System Containing Exclusively S_4^{2-} Ligands. *J. Am. Chem. Soc.* **1989**, *111*, 3767–3769.

[38] Kanatzidis, M. G. Molten Alkali-Metal Polychalcogenides as Reagents and Solvents for the Synthesis of New Chalcogenide Materials. *Chem. Mater.* **1990**, *2*, 353–363.

[39] Shoemaker, D. P.; Chung, D. Y.; Mitchell, J. F.; Bray, T. H.; Soderholm, L.; Chupas, P. J.; Kanatzidis, M. G. Understanding Fluxes as Media for Directed Synthesis: In Situ Local Structure of Molten Potassium Polysulfides. *J. Am. Chem. Soc.* **2012**, *134*, 9456–9463.

[40] Shoemaker, D. P.; Hu, Y.-J.; Chung, D. Y.; Halder, G. J.; Chupas, P. J.; Soderholm, L.; Mitchell, J. F.; Kanatzidis, M. G. In situ Studies of a Platform for Metastable Inorganic Crystal Growth and Materials Discovery. *Proc. Natl. Acad. Sci. USA* **2014**, *111*, 10922–10927.

[41] Novet, T.; Johnson, D. C. New synthetic approach to extended solids: selective synthesis of iron silicides via the amorphous state. *J. Am. Chem. Soc.* **1991**, *113*, 3398–3403.

[42] Fister, L.; Johnson, D. C. Controlling solid-state reaction mechanisms using diffusion length in ultrathin-film superlattice composites. *J. Am. Chem. Soc.* **1992**, *114*, 4639–4644.

[43] Johnson, D. C. Controlled synthesis of new compounds using modulated elemental reactants. *Curr. Opin. Solid State Mater. Sci.* **1998**, *3*, 159–167.

[44] Bauers, S. R.; Wood, S. R.; Jensen, K. M.; Blichfeld, A. B.; Iversen, B. B.; Billinge, S. J.; Johnson, D. C. Structural Evolution of Iron Antimonides from Amor-

phous Precursors to Crystalline Products Studied by Total Scattering Techniques. *J. Am. Chem. Soc.* **2015**, *137*, 9652–9658.

[45] Westover, R. D.; Ditto, J.; Falmbigl, M.; Hay, Z. L.; Johnson, D. C. Synthesis and Characterization of Quaternary Monolayer Thick $MoSe_2$/SnSe/$NbSe_2$/SnSe Heterojunction Superlattices. *Chem. Mater.* **2015**, *27*, 6411–6417.

[46] Merrill, D. R.; Sutherland, D. R.; Ditto, J.; Bauers, S. R.; Falmbigl, M.; Medlin, D. L.; Johnson, D. C. Kinetically Controlled Site-Specific Substitutions in Higher-Order Heterostructures. *Chem. Mater.* **2015**, *27*, 4066–4072.

[47] Williams, J. R.; Johnson, M. B.; Johnson, D. C. Suppression of binary nucleation in amorphous La-Fe-Sb mixtures. *J. Am. Chem. Soc.* **2003**, *125*, 3589–3592.

[48] Anderson, M. D.; Thompson, J. O.; Johnson, D. C. Avoiding binary compounds as reaction intermediates in solid state reactions. *Chem. Mater.* **2013**, *25*, 3996–4002.

[49] Hornbostel, M. D.; Hyer, E. J.; Thiel, J.; Johnson, D. C. Rational synthesis of metastable skutterudite compounds using multilayer precursors. *J. Am. Chem. Soc.* **1997**, *119*, 2665–2668.

[50] Burrard-Lucas, M.; Free, D. G.; Sedlmaier, S. J.; Wright, J. D.; Cassidy, S. J.; Hara, Y.; Corkett, A. J.; Lancaster, T.; Baker, P. J.; Blundell, S. J.; Clarke, S. J. Enhancement of the Superconducting Transition Temperature of FeSe by Intercalation of a Molecular Spacer Layer. *Nat. Mater.* **2013**, *12*, 15–19.

[51] Liu, H.; Strobridge, F. C.; Borkiewicz, O. J.; Wiaderek, K. M.; Chapman, K. W.; Chupas, P. J.; Grey, C. P. Capturing metastable structures during high-rate cycling of $LiFePO_4$ nanoparticle electrodes. *Science* **2014**, *344*.

[52] Strobridge, F. C.; Liu, H.; Leskes, M.; Borkiewicz, O. J.; Wiaderek, K. M.; Chupas, P. J.; Chapman, K. W.; Grey, C. P. Unraveling the Complex Delithiation Mechanisms of Olivine-Type Cathode Materials, $LiFe_xCo_{1-x}PO_4$. *Chem. Mater.* **2016**, *28*, 3676–3690.

[53] Wiaderek, K. M.; Borkiewicz, O. J.; Castillo-Martínez, E.; Robert, R.; Pereira, N.; Amatucci, G. G.; Grey, C. P.; Chupas, P. J.; Chapman, K. W. Comprehensive Insights into the Structural and Chemical Changes in Mixed-Anion FeOF Electrodes by Using Operando PDF and NMR Spectroscopy. *J. Am. Chem. Soc.* **2013**, *135*, 4070–4078.

[54] Hua, X.; Robert, R.; Du, L.-S.; Wiaderek, K. M.; Leskes, M.; Chapman, K. W.; Chupas, P. J.; Grey, C. P. Comprehensive study of the CuF_2 conversion reaction mechanism in a lithium ion battery. *J. Phys. Chem. C.* **2014**, *118*, 15169–15184.

[55] Bonneau, P. R.; Jarvis, R. F.; Kaner, R. B. Rapid Solid-State Synthesis of Materials from Molybdenum Disulphide to Refractories. *Nature* **1991**, *349*, 510–512.

[56] Wiley, J.; Kaner, R. Rapid solid-state precursor synthesis of materials. *Science* **1992**, *255*, 1093–1097.

[57] Parkin, I. P. Solid state metathesis reaction for metal borides, silicides, pnictides and chalcogenides: ionic or elemental pathways. *Chem. Soc. Rev.* **1996**, *25*, 199–207.

[58] Nartowski, A. M.; Parkin, I. P.; Craven, A. J.; MacKenzie, M. Rapid, Solid-State Metathesis Routes to Metal Carbides. *Adv. Mater.* **1998**, *10*, 805–808.

[59] Cumberland, R. W.; Weinberger, M. B.; Gilman, J. J.; Clark, S. M.; Tolbert, S. H.; Kaner, R. B. Osmium Diboride, An Ultra-Incompressible, Hard Material. *J. Am. Chem. Soc.* **2005**, *127*, 7264–7265.

[60] Chung, H.-Y.; Weinberger, M. B.; Levine, J. B.; Kavner, A.; Yang, J.-M.; Tolbert, S. H.; Kaner, R. B. Synthesis of ultra-incompressible superhard rhenium diboride at ambient pressure. *Science* **2007**, *316*, 436–439.

[61] Rao, L.; Gillan, E. G.; Kaner, R. B. Rapid synthesis of transition-metal borides by solid-state metathesis. *J. Mater. Res.* **1995**, *10*, 353–361.

[62] Gillan, E. G.; Kaner, R. B. Synthesis of refractory ceramics via rapid metathesis reactions between solid-state precursors. *Chem. Mater.* **1996**, *8*, 333–343.

[63] Martinolich, A. J.; Neilson, J. R. Pyrite Formation via Kinetic Intermediates through Low-Temperature Solid-State Metathesis. *J. Am. Chem. Soc.* **2014**, *136*, 15654–15659.

[64] Committee for an Assessment of and Outlook for New Materials Synthesis and Crystal Growth; National Research Council (US), *Frontiers in Crystalline Matter: From Discovery to Technology*; The National Academies Press, 2009.

[65] Shaw, G. A.; Morrison, D. E.; Parkin, I. P. Solid state synthesis of binary metal chalcogenides. *J. Chem. Soc., Dalton Trans.* **2001**, 1872–1875.

[66] Mann, A. K. P.; Skrabalak, S. E. Synthesis of Single-Crystalline Nanoplates by Spray Pyrolysis: A Metathesis Route to Bi_2WO_6. *Chem. Mater.* **2011**, *23*, 1017–1022.

[67] Motl, N. E.; Mann, A. K. P.; Skrabalak, S. E. Aerosol-assisted synthesis and assembly of nanoscale building blocks. *J. Mater. Chem. A* **2013**, *1*, 5193–5202.

[68] Yu, L.; Lany, S.; Kykyneshi, R.; Jieratum, V.; Ravichandran, R.; Pelatt, B.; Altschul, E.; Platt, H. A. S.; Wager, J. F.; Keszler, D. A.; Zunger, A. Iron Chalcogenide Photovoltaic Absorbers. *Adv. Energy Mater.* **2011**, *1*, 748–753.

[69] Seefeld, S.; Limpinsel, M.; Liu, Y.; Farhi, N.; Weber, A.; Zhang, Y.; Berry, N.; Kwon, Y. J.; Perkins, C. L.; Hemminger, J. C.; Wu, R.; Law, M. Iron Pyrite Thin Films Synthesized from an Fe(acac)3 Ink. *J. Am. Chem. Soc.* **2013**, *135*, 4412–4424.

[70] Bither, T.; Donohue, P.; Cloud, W.; Bierstedt, P.; Young, H. Mixed-cation transition metal pyrite dichalcogenides—High pressure synthesis and properties. *J. Solid State Chem.* **1970**, *1*, 526 – 533.

[71] Corliss, L. M.; Elliott, N.; Hastings, J. M. Antiferromagnetic Structures of MnS_2, $MnSe_2$, and $MnTe_2$. *J. Appl. Phys.* **1958**, *29*, 391–392.

[72] Ennaoui, A.; Tributsch, H. Iron Sulphide Solar Cells. *Solar Cells* **1984**, *13*, 197–200.

[73] Cheng, S. F.; Woods, G. T.; Bussmann, K.; Mazin, I.; Soulen, J., R.J.; Carpenter, E.; Das, B.; Lubitz, P. Growth and magnetic properties of single crystal $Fe_{1-x}Co_xS_2$ ($x = 0.35 - 1$). *J. Appl. Phys.* **2003**, *93*, 6847–6849.

[74] Gautier, F.; Krill, G.; Lapierre, M.; Panissod, P.; Robert, C.; Czjzek, G.; Fink, J.; Schmidt, H. Existence of an antiferromagnetic metallic phase (AFM) in the $NiS_{2-x}Se_x$ system with pyrite structure. *Phys. Lett. A* **1975**, *53*, 31 – 33.

[75] Goodenough, J. B. Conceptual phase diagram and its application to the spontaneous magnetism of several pyrites. *J. Solid State Chem.* **1971**, *3*, 26 – 38.

[76] Bonneau, P. R.; Shibao, R. K.; Kaner, R. B. Low-Temperature Precursor Synthesis of Crystalline Nickel Disulfide. *Inorg. Chem.* **1990**, *29*, 2511–2514.

[77] Bonneau, P. R.; Jarvis, R. F.; Kaner, R. B. Solid-state metathesis as a quick route to transition-metal mixed dichalcogenides. *Inorg. Chem.* **1992**, *31*, 2127–2132.

[78] Wang, J.; Toby, B. H.; Lee, P. L.; Ribaud, L.; Antao, S. M.; Kurtz, C.; Ramanathan, M.; Von Dreele, R. B.; Beno, M. A. A dedicated powder diffraction beamline at the Advanced Photon Source: Commissioning and early operational results. *Rev. Sci. Instrum.* **2008**, *79*, 085105.

[79] Toby, B. H. *EXPGUI*, a graphical user interface for *GSAS*. *J. Appl. Crystallogr.* **2001**, *34*, 210–213.

[80] Larson, A.; Von Dreele, R. General Structure Analysis System (GSAS). Los Alamos National Lab, 2004.

[81] Taylor, P.; Shoesmith, D. W. The nature of green alkaline iron sulfide solutions and the preparation of sodium iron(III) sulfide, $NaFeS_2$. *Can. J. Chem.* **1978**, *56*, 2797–2802.

[82] Taft, C. A. Mössbauer studies of $NaFeS_2$: magnetic hyperfine fields and covalency in MFeS$_2$ compounds (M = Na, K, Rb, Cs). *J. Phys. (Paris)* **1977**, *38*, 1161–1162.

[83] Abrahams, S. C. The crystal and molecular structure of orthorhombic sulfur. *Acta Cryst.* **1955**, *8*, 661–671.

[84] Lee, B.-J.; Sundman, B.; Kim, S. I.; Chin, K.-G. Thermodynamic Calculations on the Stability of Cu_2S in Low Carbon Steels. *ISIJ International* **2007**, *47*, 163–171.

[85] Sangster, J.; Pelton, A. The Na-S (Sodium-Sulfur) system. *J. Phase Equilib.* **1997**, *18*, 89–96.

[86] Patnaik, P. *Handbook of Inorganic Chemicals*; McGraw-Hill handbooks; McGraw-Hill, 2003.

[87] Lassin, A.; Piantone, P.; Crouzet, C.; Bodénan, F.; Blanc, P. Estimated thermodynamic properties of $NaFeS_2$ and erdite ($NaFeS_2$:2H_2O). *Appl. Geochem.* **2014**, *45*, 14–24.

[88] Jain, A.; Ong, S. P.; Hautier, G.; Chen, W.; Richards, W. D.; Dacek, S.; Cholia, S.; Gunter, D.; Skinner, D.; Ceder, G.; Persson, K. A. The Materials Project: A materials genome approach to accelerating materials innovation. *APL Materials* **2013**, *1*, 011002.

[89] Caron, J. M.; Neilson, J. R.; Miller, D. C.; Llobet, A.; McQueen, T. M. Iron displacements and magnetoelastic coupling in the antiferromagnetic spin-ladder compound $BaFe_2Se_3$. *Phys. Rev. B* **2011**, *84*, 180409.

[90] Caron, J. M.; Neilson, J. R.; Miller, D. C.; Arpino, K.; Llobet, A.; McQueen, T. M. Orbital-selective magnetism in the spin-ladder iron selenides $Ba_{1-x}K_xFe_2Se_3$. *Phys. Rev. B* **2012**, *85*, 180405.

[91] Neilson, J. R.; Llobet, A.; Stier, A. V.; Wu, L.; Wen, J.; Tao, J.; Zhu, Y.; Tesanovic, Z. B.; Armitage, N. P.; McQueen, T. M. Mixed-valence-driven heavy-fermion behavior and superconductivity in KNi_2Se_2. *Phys. Rev. B* **2012**, *86*, 054512.

[92] Neilson, J. R.; McQueen, T. M.; Llobet, A.; Wen, J.; Suchomel, M. R. Charge density wave fluctuations, heave electrons, and superconductivity in KNi_2S_2. *Phys. Rev. B* **2013**, *87*, 045124.

[93] Boller, H.; Blaha, H. Zur Kenntnis des Natriumthioferrates(III). *Monatsh. Chem.* **1983**, *114*, 145–154.

[94] Neilson, J.; Kurzman, J.; Seshadri, R.; Morse, D. Cobalt Coordination and Clustering in α-Co(OH)2 Revealed by Synchrotron X-ray Total Scattering. *Chem. Eur. J.* **2010**, *16*, 9998–10006.

[95] Martinolich, A. J.; Kurzman, J. A.; Neilson, J. R. Circumventing Diffusion in Kinetically-Controlled Solid-State Metathesis Reactions. *J. Am. Chem. Soc.* **2016**, *138*, 11031–11037.

[96] Buck, M. R.; Bondi, J. F.; Schaak, R. E. A Total-Synthesis Framework for the Construction of High-Order Colloidal Hybrid Nanoparticles. *Nat. Chem.* **2012**, *4*, 37–44.

[97] Gopalakrishnan, J. Chimie Douce Approaches to the Synthesis of Metastable Oxide Materials. *Chem. Mater.* **1995**, *7*, 1265–1275.

[98] Martinolich, A. J.; Kurzman, J. A.; Neilson, J. R. Polymorph Selectivity of Superconducting $CuSe_2$ Through Kinetic Control of Solid-State Metathesis. *J. Am. Chem. Soc.* **2015**, *137*, 3827–3833.

[99] Martinolich, A. J.; Higgins, R. F.; Shores, M. P.; Neilson, J. R. Lewis Base Mediated Polymorph Selectivity of Pyrite $CuSe_2$ Through Atom Transfer In Solid State Metathesis. *Chem. Mater.* **2016**, *28*, 1854–1860.

[100] Chupas, P. J.; Chapman, K. W.; Kurtz, C.; Hanson, J. C.; Lee, P. L.; Grey, C. P. A versatile sample-environment cell for non-ambient X-ray scattering experiments. *J. Appl. Crystallogr.* **2008**, *41*, 822–824.

[101] Toby, B. H.; Von Dreele, R. B. *GSAS-II*: the genesis of a modern open-source all purpose crystallography software package. *J. Appl. Crystallogr.* **2013**, *46*, 544–549.

[102] Hammersley, A. P.; Svensson, S. O.; Hanfland, M.; Fitch, A. N.; Hausermann, D. Two-dimensional detector software: From real detector to idealised image or two-theta scan. *High Pressure Res.* **1996**, *14*, 235–248.

[103] Juhás, P.; Davis, T.; Farrow, C. L.; Billinge, S. J. L. *PDFgetX3*: a rapid and highly automatable program for processing powder diffraction data into total scattering pair distribution functions. *J. Appl. Crystallogr.* **2013**, *46*, 560–566.

[104] Farrow, C. L.; Juhas, P.; Liu, J. W.; Bryndin, D.; Božin, E. S.; Bloch, J.; Proffen, T.; Billinge, S. J. L. PDFfit2 and PDFgui: computer programs for studying nanostructure in crystals. *J. Phys.-Condens. Mat.* **2007**, *19*, 335219.

[105] Lide, D. R. *CRC Handbook of Chemistry and Physics, 87th Edition*, 87th ed.; CRC Press, 2005.

[106] Gösele, U.; Tu, K. "Critical Thickness" of Amorphous Phase Formation in Binary Diffusion Couples. *J. Appl. Phys.* **1989**, *66*, 2619–2626.

[107] Walser, R.; Bené, R. First phase nucleation in silicon–transition-metal planar interfaces. *Appl. Phys. Lett.* **1976**, *28*, 624–625.

[108] Gösele, U.; Tu, K. Growth Kinetics of Planar Binary Diffusion Couples:"Thin-Film Case" Versus "Bulk Cases". *J. Appl. Phys.* **1982**, *53*, 3252–3260.

[109] Bené, R. A Kinetic Model for Solid-State Silicide Nucleation. *J. Appl. Phys.* **1987**, *61*, 1826–1833.

[110] Qi, Y.; Matsuishi, S.; Guo, J.; Mizoguchi, H.; Hosono, H. Superconductivity in Defective Pyrite-Type Iridium Chalcogenides Ir_xCh_2 (Ch = Se and Te). *Phys. Rev. Lett.* **2012**, *109*, 217002.

[111] Tossell, J.; Vaughan, D.; Burdett, J. Pyrite, marcasite, and arsenopyrite type minerals: Crystal chemical and structural principles. *Phys. Chem. Miner.* **1981**, *7*, 177–184.

[112] Hull, G. W.; Hulliger, F. $CuSe_2$, a Marcasite Type Superconductor. *Nature* **1968**, *220*, 257–258.

[113] Schollhorn, R. From Electronic/Ionic Conductors to Superconductors: Control of Materials Properties. *Angew. Chem. Int. Ed.* **1988**, *27*, 1392–1400.

[114] Schleich, D. Chimie douce: Low temperature techniques for synthesizing useful compounds. *Solid State Ionics* **1994**, *70/71*, 407–411.

[115] Rouxel, J.; Tournoux, M. Chimie douce with solid precursors, past and present. *Solid State Ionics* **1996**, *84*, 141–149.

[116] Gopalakrishnan, J.; Bhuvanesh, N. S. P.; Rangan, K. K. Towards rational synthesis of inorganic solids. *Curr. Opin. Solid State Mater. Sci.* **1996**, *1*, 285–294.

[117] Kanatzidis, M. G.; Park, Y. Molten salt synthesis of low-dimensional ternary chalcogenides. Novel structure types in the K/Hg/Q system (Q = S, Se). *Chem. Mater.* **1990**, *2*, 99–101.

[118] Murnaghan, F. D. The Compressibility of Media under Extreme Pressures. *Proc. Natl. Acad. Sci. USA* **1944**, *30*, 244–247.

[119] Cohen, K.; Rivet, J.; Dugué, J. Description of the Cu-As-Se ternary system. *J. Alloy Compd.* **1995**, *224*, 316 – 329.

[120] Kresse, G.; Joubert, D. From ultrasoft pseudopotentials to the projector augmented-wave method. *Phys. Rev. B* **1999**, *59*, 1758.

[121] Kresse, G.; Furthmüller, J. Efficient iterative schemes for ab initio total-energy calculations using a plane-wave basis set. *Phys. Rev. B* **1996**, *54*, 11169.

[122] Perdew, J. P.; Ruzsinszky, A.; Csonka, G. I.; Vydrov, O. A.; Scuseria, G. E.; Constantin, L. A.; Zhou, X.; Burke, K. Restoring the density-gradient expansion for exchange in solids and surfaces. *Phys. Rev. Lett.* **2008**, *100*, 136406.

[123] Mao, Z. Q.; Mori, Y.; Maeno, Y. Suppression of superconductivity in $\mathrm{Sr_2RuO_4}$ caused by defects. *Phys. Rev. B* **1999**, *60*, 610–614.

[124] Serquis, A.; Zhu, Y. T.; Peterson, E. J.; Coulter, J. Y.; Peterson, D. E.; Mueller, F. M. Effect of lattice strain and defects on the superconductivity of MgB_2. *Appl. Phys. Lett.* **2001**, *79*, 4399–4401.

[125] McQueen, T. M.; Huang, Q.; Ksenofontov, V.; Felser, C.; Xu, Q.; Zandbergen, H.; Hor, Y. S.; Allred, J.; Williams, A. J.; Qu, D.; Checkelsky, J.; Ong, N. P.; Cava, R. J. Extreme sensitivity of superconductivity to stoichiometry in $Fe_{1+\delta}Se$. *Phys. Rev. B* **2009**, *79*, 014522.

[126] Friščić, T.; Halasz, I.; Beldon, P. J.; Belenguer, A. M.; Adams, F.; Kimber, S. A. J.; Honkimäki, V.; Dinnebier, R. E. Real-time and in situ monitoring of mechanochemical milling reactions. *Nat. Chem.* **2013**, *5*, 66–73.

[127] Belenguer, A. M.; Lampronti, G. I.; Wales, D. J.; Sanders, J. K. M. Direct Observation of Intermediates in a Thermodynamically Controlled Solid-State Dynamic Covalent Reaction. *J. Am. Chem. Soc.* **2014**, *136*, 16156–16166.

[128] Zhang, H.; Gilbert, B.; Huang, F.; Banfield, J. F. Water-driven structure transformation in nanoparticles at room temperature. *Nature* **2003**, *424*, 1025–1029.

[129] Ohtani, T.; Motoki, M.; Koh, K.; Ohshima, K. Synthesis of binary copper chalcogenides by mechanical alloying. *Mater. Res. Bull.* **1995**, *30*, 1495 – 1504.

[130] Berry, L. G. The Crystal Structure of Covellite, CuS, and Klockmannite, CuSe. *Am. Mineral.* **1954**, *39*, 504–509.

[131] Heyding, R. D.; Murray, R. M. The crystal structures of $Cu_{1.8}Se$, Cu_3Se_2, α- and γ-CuSe, $CuSe_2$, and $CuSe_2$-II. *Can. J. Chem.* **1976**, *54*, 841–848.

[132] Momma, K.; Izumi, F. *VESTA 3* for three-dimensional visualization of crystal, volumetric and morphology data. *J. Appl. Crystallogr.* **2011**, *44*, 1272–1276.

[133] Kumar, P.; Nagarajan, R.; Sarangi, R. Quantitative X-ray absorption and emission spectroscopies: electronic structure elucidation of Cu2S and CuS. *J. Mater. Chem. C* **2013**, *1*, 2448–2454.

[134] Conejeros, S.; Moreira, I. d. P. R.; Alemany, P.; Canadell, E. Nature of Holes, Oxidation States, and Hypervalency in Covellite (CuS). *Inorg. Chem.* **2014**, *53*, 12402–12406.

[135] Ostwald, W. Studien über die Bildung und Umwandlung fester Körper. *Z. Phys. Chem.* **1897**, *22*, 289–330.

[136] Navrotsky, A. Energetic clues to pathways to biomineralization: Precursors, clusters, and nanoparticles. *Proc. Natl. Acad. Sci. USA* **2004**, *101*, 12096–12101.

[137] Ogawa, S. Magnetic properties of 3d transition-metal dichalcogenides with the pyrite structure. *J. Appl. Phys.* **1979**, *50*, 2308–2311.

[138] Abel, E.; Jenkins, C. Interaction of thiosilanes and disilthianes with some transitional and post-transitional metal halides. *J. Organometal. Chem.* **1968**, *14*, 285 – 289.

[139] Abel, E.; Brady, D. 210. The preparation and properties of some alkylthio-compounds of tin. *J. Chem. Soc.* **1965**, 1192–1197.

[140] Schleich, D.; Martin, M. Synthesis of novel molybdenum chalcogenides. *J. Solid State Chem.* **1986**, *64*, 359 – 364.

[141] Martin, M. J.; Qiang, G. H.; Schleich, D. M. New low-temperature synthesis of transition-metal sulfides. *Inorg. Chem.* **1988**, *27*, 2804–2808.

[142] Bartlett, P. D.; Meguerian, G. Reactions of Elemental Sulfur. I. The Uncatalyzed Reaction of Sulfur with Triarylphosphines1. *J. Am. Chem. Soc.* **1956**, *78*, 3710–3715.

[143] Abel, E. W.; Armitage, D. A.; Bush, R. P. 1069. The formation of phosphorus-sulphur compounds from phosphorus halides and alkylthiosilanes and silthianes. *J. Chem. Soc.* **1964**, 5584–5587.

[144] Sines, I. T.; Schaak, R. E. Phase-Selective Chemical Extraction of Selenium and Sulfur from Nanoscale Metal Chalcogenides: A General Strategy for Synthesis, Purification, and Phase Targeting. *J. Am. Chem. Soc.* **2011**, *133*, 1294–1297.

[145] Ruberu, T. P. A.; Albright, H. R.; Callis, B.; Ward, B.; Cisneros, J.; Fan, H.-J.; Vela, J. Molecular Control of the Nanoscale: Effect of Phosphine–Chalcogenide Reactivity on CdS–CdSe Nanocrystal Composition and Morphology. *ACS Nano* **2012**, *6*, 5348–5359.

[146] Ng, M. C. C.; Harper, J. B.; Stampfl, A. P. J.; Kearley, G. J.; Rols, S.; Stride, J. A. Central-Atom Size Effects on the Methyl Torsions of Group XIV Tetratolyls. *Chem. Eur. J.* **2012**, *18*, 13018–13024.

[147] Ramakrishna, D.; Bhat, B. R. A catalytic process for the selective oxidation of alcohols by copper (II) complexes. *Inorg. Chem. Commun.* **2011**, *14*, 690–693.

[148] Kociok-Köhn, G.; Molloy, K. C.; Sudlow, A. L. Molecular routes to Cu_2ZnSnS_4: A comparison of approaches to bulk and thin-film materials. *Can. J. Chem.* **2014**, *92*, 514–524.

[149] Morgan, W. E.; Stec, W. J.; Albridge, R. G.; Van Wazer, J. R. π-Bond feedback interpreted from the binding energy of the "2p" electrons of phosphorus. *Inorg. Chem.* **1971**, *10*, 926–930.

[150] Weightman, P.; Roberts, E.; Johnson, C. $L_{2,3}MM$ Auger processes in selenium. *J. Phys. C: Solid State Phys.* **1975**, *8*, 550.

[151] Bahl, M.; Watson, R.; Irgolic, K. LMM Auger spectra of selenium and some of its compounds. *J. Chem. Phys.* **1980**, *72*, 4069–4077.

[152] Crist, B. V. Handbook of monochromatic XPS spectra, The elements of native Oxides. *Handbook of Monochromatic XPS Spectra, The Elements of Native Oxides, by B. Vincent Crist, pp. 548. ISBN 0-471-49265-5. Wiley-VCH, October 2000.* **2000**, *1*.

[153] Park, J.; Koo, B.; Yoon, K. Y.; Hwang, Y.; Kang, M.; Park, J.-G.; Hyeon, T. Generalized synthesis of metal phosphide nanorods via thermal decomposition of continuously delivered metal-phosphine complexes using a syringe pump. *J. Am. Chem. Soc.* **2005**, *127*, 8433–8440.

[154] Henkes, A. E.; Schaak, R. E. Trioctylphosphine: a general phosphorus source for the low-temperature conversion of metals into metal phosphides. *Chem. Mater.* **2007**, *19*, 4234–4242.

[155] Brock, S. L.; Senevirathne, K. Recent developments in synthetic approaches to transition metal phosphide nanoparticles for magnetic and catalytic applications. *J. Solid State Chem.* **2008**, *181*, 1552–1559.

[156] Dean, J. A., Ed. *Lange's Handbook of Chemistry*, 15th ed.; McGraw Hill Inc., New York, NY, 1999.

[157] Zingaro, R. A. Phosphine Sulfides and Selenides: The Phosphorus-Sulfur and Phosphorus-Selenium Stretching Frequencies. *Inorg. Chem.* **1963**, *2*, 192–196.

[158] Gáti, A. T. G. M. D. M. S. D. H., T.; Simon Adducts of $Rh_2[MTPA]_4$ With Some Phosphine Chalcogenides: Nature of Binding and Ligand Exchange. *Magn. Reson. Chem.* **2004**, *42*, 600–604.

[159] Grossmann, G.; Potrzebowski, M. J.; Fleischer, U.; Krüger, K.; Malkina, O. L.; Ciesielski, W. Anisotropy of chemical shift and J coupling for P-31 and Se-77 in trimethyl and triphenyl phosphine selenides. *Solid State Nucl. Mag.* **1998**, *13*, 71 – 85.

[160] Arnett, E. M.; Quirk, R. P.; Burke, J. J. Weak bases in strong acids. III. Heats of ionization of amines in fluorosulfuric and sulfuric acids. New general basicity scale. *J. Am. Chem. Soc.* **1970**, *92*, 1260–1266.

[161] Hoefnagel, A. J.; Hoefnagel, M. A.; Wepster, B. M. Substituent effects. 8. Basic strength of azatriptycene, triphenylamine, and some related amines. *J. Org. Chem.* **1981**, *46*, 4209–4211.

[162] Alvarado, S. R.; Shortt, I. A.; Fan, H.-J.; Vela, J. Assessing Phosphine–Chalcogen Bond Energetics from Calculations. *Organometallics* **2015**, *34*, 4023–4031.

[163] Pedoussaut, N. M.; Lind, C. Facile Synthesis of Troilite. *Inorg. Chem.* **2008**, *47*, 392–394.

[164] Evans, H. T. Lunar Troilite: Crystallography. *Science* **1970**, *167*, 621–623.

[165] Okamoto, H. The Fe-Se (Iron-Selenium) System. *J. Phase Equilib.* **1991**, *12*, 383–389.

[166] Svendsen, S. R. Decomposition Pressures and Standard Enthalpy of Formation of the Iron Selenides FeSe, Fe_7Se_8, Fe_3Se_4, and $FeSe_2$. *Acta Chem. Scand.* **1972**, *26*, 3757–3774.

[167] Lai, X.; Zhang, H.; Wang, Y.; Wang, X.; Zhang, X.; Lin, J.; Huang, F. Observation of Superconductivity in Tetragonal FeS. *J. Am. Chem. Soc.* **2015**, *137*, 10148–10151.

[168] Borg, C. K.; Zhou, X.; Eckberg, C.; Campbell, D. J.; Saha, S. R.; Paglione, J.; Rodriguez, E. E. Strong anisotropy in nearly ideal tetrahedral superconducting FeS single crystals. *Phys. Rev. B* **2016**, *93*, 094522.